

TECHNISCHE UNIVERSITÄT MÜNCHEN
Lehrstuhl für Computation in Engineering

Finite Cell Method for Transport Problems in Porous Media

Quanji Cai

Vollständiger Abdruck der von der Ingenieur fakultät Bau Geo Umwelt der Technischen Universität München zur Erlangung des akademischen Grades eines

Doktor-Ingenieurs

genehmigten Dissertation.

Vorsitzender: Univ.-Prof. Dr.-Ing. habil. M. Manhart

Prüfer der Dissertation:

1. Univ.-Prof. Dr.rer.nat. E. Rank
2. Univ.-Prof. Dr.-Ing. habil. A. Düster

Technische Universität Hamburg-Harburg

Die Dissertation wurde am 30.04.2013 bei der Technischen Universität München eingereicht und durch die Ingenieur fakultät Bau Geo Umwelt am 25.06.2013 angenommen.

Abstract

This thesis presents a generalization of the recently proposed Finite Cell Method (FCM) for problems in solid mechanics to the simulation of convection-diffusion transport problems in porous media. The FCM – a combination of a Fictitious Domain approach and high order Finite Elements - is an accurate computational technique for complex domains, which dispenses with the need for generating boundary-conforming meshes. The high order FEM will be shown to stabilize the oscillation at nodal solutions introduced in convection-dominated problems. One- and two-dimensional model problems are demonstrated where exponential convergence rates are observed. The validity of the approach is studied for convection- and diffusion-dominated flows, concluding this treatise with a three-dimensional single component, convection-diffusion example and a two-dimensional multicomponent, reactive transport problem based on a complex interior geometrical structure to emphasize the potential of this method.

Zusammenfassung

Die vorliegende Arbeit soll einen Beitrag zur Generalisierung der Finite Cell Methode (FCM) leisten, die für Probleme aus der Festkörpermechanik bereits sehr erfolgreich angewendet wurde und nun auf die Simulation von Transportprozessen erweitert wird. Dabei stellt die FCM – eine Kombination aus Fictitious Domain-Methode mit finiten Elementen hoher Ordnung – ein genaues numerisches Verfahren dar, das insbesondere bei komplexen Gebieten durch den Verzicht auf die Generierung von randkonformen Netzen seine Stärke ausspielen kann. Am Beispiel ein- und zweidimensionaler Probleme wird gezeigt, dass finite Elemente hoher Ordnung Oszillationen von Knotenlösungen in konvektionsdominierten Problemen stabilisieren und sich exponentielle Konvergenzraten erzielen lassen. Die Gültigkeit des Verfahrens wird dabei für konvektions- und diffusionsdominierte Strömungen untersucht. Anhand weiterer Beispiele wird das Potenzial der verwendeten Methode herausgestellt.

Acknowledgements

The work presented in this thesis has been accomplished during my time as a doctoral candidate at the Chair for Computation in Engineering at Technische Universität München.

This work has been funded by the Munich Centre of Advanced Computing (MAC) and the International Graduate School of Science and Engineering (IGSSE) at Technische Universität München. This support is gratefully acknowledged.

I would like to give special thanks to Prof. Dr.rer.nat. Ernst Rank for giving me the opportunity to work on this topic. Without his continuous help, support and encouragement in my work, I would not be able to finish the thesis.

I am very grateful to Prof. Dr.-Ing. habil. Alexander Düster for giving me constructive comments on the thesis and agreeing to be the second examiner.

I acknowledge Prof. Antonio Huerta for his guidance and support during my visit at the Department of Applied Mathematics III at Universitat Politècnica de Catalunya in Spain.

I would like to express my gratitude to my current boss Prof. Dr.-Ing. Wolfram Volk for his guidance and inspiration on my work.

I gratefully thank all colleagues who have contributed to this work. Special thanks go to Dr.-Ing. Stefan Kollmannsberger for his ongoing effort and helpful advice on the subject. I would also like to thank Dr.rer.nat. Ralf-Peter Mundani for his kind support and encouragement.

Last but not least, I would like to especially thank my parents and my husband for their endless love and support.

Quanji Cai
Munich, April 2013

Contents

List of symbols	ix
1 Introduction	1
2 Numerical simulation in fluid mechanics	6
2.1 The basic equations of fluid mechanics	6
2.1.1 The conservation law for a scalar quantity	7
2.1.2 Convection-diffusion equation	8
2.2 Transport equations in groundwater flow	11
2.2.1 Darcy's law	12
2.2.2 Multicomponent reactive transport problems	13
2.3 Numerical methods in transport problems	15
2.3.1 Finite difference method	15
2.3.1.1 Basic theory	16
2.3.1.2 Application in mass transport problems	17
2.3.2 Finite element method	18
2.3.2.1 Basic principles	18
2.3.2.2 The Bubnov-Galerkin discretization	20
2.3.2.3 The Streamline Upwind Petrov-Galerkin (SUPG) discretization	22
2.3.2.4 Error estimation in different norms	24
3 High Order Finite Element Method (p-FEM)	27
3.1 Basic principles	27
3.2 High order shape functions	29
3.2.1 Lagrange shape function – nodal expansion	29
3.2.2 Hierarchic shape function – modal expansion	29
3.2.2.1 One-dimensional hierarchic shape function	30
3.2.2.2 Two-dimensional hierarchic shape function	31
3.2.2.3 Three-dimensional hierarchic shape function	31
3.3 Numerical examples in transport problems	36
3.3.1 Single-component transport problems	36
3.3.1.1 One-dimensional simple Dirichlet boundary problem	36
3.3.1.2 Two-dimensional steady rotating pulse problem	36
3.3.2 Multi-component reactive transport problems	38
3.3.2.1 Fixed point iteration for coupled reaction terms	40
3.3.2.2 Three-component transient reactive transport problem in 1D	41

4	Stability analysis of p-FEM in convection-dominated problems	46
4.1	Truncation error of the Bubnov-Galerkin discretization in the h -FEM	47
4.2	Truncation error of the Bubnov-Galerkin discretization in the p -FEM	50
4.3	Connection of the stability and the structure of the system matrix	53
4.3.1	Spectral properties of tridiagonal Toeplitz matrix	54
4.4	Stability analysis of nodal solutions in the p -FEM	54
4.5	Verification of truncation analysis in 1D convection-diffusion problem	60
5	Finite Cell Method in transport problems in porous media	65
5.1	Basic principles	65
5.2	Different integration schemes	67
5.2.1	Gaussian quadrature employing over-integration	67
5.2.2	Subcell integration schemes	68
5.2.2.1	Uniform subcell integration scheme	70
5.2.2.2	Adaptive integration scheme	72
5.3	FCM in single-component reactive transport problems in porous media	73
5.3.1	The performance of the FCM in 1D transport problems	73
5.3.2	The performance of the FCM in 2D transport problems	76
5.3.3	The performance of the FCM in 3D transport problems	80
5.4	FCM in multi-component reactive transport problems in porous media	91
6	Conclusion	95
	Bibliography	96

List of symbols

The symbols used in this work are listed in alphabetical order.

Latin letters

Symbol

a	magnitude of fluid velocity
a_i	unknowns of a finite element approximation
\vec{a}	fluid velocity
A	cross-sectional area of the sand filter
\mathcal{A}	system matrix
\mathbf{B}	strain-displacement matrix
\mathbf{B}_B	strain-displacement matrix with respect to bending deformation
$\mathbf{B}_S, \bar{\mathbf{B}}_S$	strain-displacement matrix with respect to shear deformation
c	dissolved concentration of a solute
c_j	dissolved concentration of the j th solute component
c^γ	finite element approximation of dissolved concentration of a solute
c_H^γ	component of finite element approximation associated with homogeneous Dirichlet boundary condition
c_D^γ	component of finite element approximation associated with prescribed Dirichlet boundary condition
\mathbf{C}	convection matrix
C^e	element convection matrix
C_{ij}^e	entries of element convection matrix
$\mathbf{c}_{i,j}^t$	concentration of the i^{th} component in the j^{th} fixed point iteration at time t
\mathbf{D}	diffusion matrix
D^e	element diffusion matrix
D_{ij}^e	entries of element diffusion matrix
e	error of the finite element solution

\vec{F}	volumetric flow rate, or flux
\vec{F}_C	convective flux
\vec{F}_D	effective diffusive flux
\vec{F}'_D	mechanical dispersion flux
f	body source/sink term per unit volume
\mathbf{f}	force vector
f^e	element force vector
f_i^e	entries of element force vector
$\mathbf{F}_{i,j}^t$	Force vector of the concentration $\mathbf{c}_{i,j}^t$
g	gravitational acceleration
h	mesh size of a finite element
h_1	upper length of the sand filter
h_2	lower length of the sand filter
$H^1(\Omega)$	the first Sobolev space
$I = (a, b)$	finite interval
k_1, k_2, k_3	reaction coefficients
K	hydraulic conductivity
K_d	constant adsorption coefficient
l	length of a finite element
L	length of the sand filter
$\{L_n(x)\}_{n=0}^{\infty}$	Legendre polynomials
n	number of Gaussian points
\vec{n}	outward-pointing unit normal vector
N_i	shape functions
p	polynomial degree of a finite element
p_1, p_2	pressure in fluid
Pe	<i>Péclet</i> number
P_t	porosity of porous media
\vec{q}	Darcy's velocity
Q	volumetric flow rate, or flux
Q_Ω	body source/sink term per unit volume
\vec{Q}_S	surface source/sink term per unit area
r	subcell coordinate of a finite element
r_i	relative point of a subcell in the cell coordinate
R_{ij}	c_j related reaction terms
R_r	coordinate of Gaussian point
R_s	saturation ratio
Re	Reynold's number

s	subcell coordinate of a finite element
s_{ij}	coefficients of reaction terms
s_j	relative point of a subcell in the cell coordinate
S	sorbed contaminant mass of rock
S_s	coordinate of Gaussian point
\vec{S}	a control face of a control volume
t	time
t	subcell coordinate of a finite element
t_k	relative point of a subcell in the cell coordinate
Δt	constant time step
T_t	coordinate of Gaussian point
U	a conserved scalar quantity
v	pore velocity
V_l	volume of liquid
V_s	volume of solid
V_p	volume of pore
V_t	volume of total phase
w	weight function
w^γ	finite element approximation of weight function
x	global coordinates of a finite element
Δx	constant grid spacing
y	global coordinates of a finite element
z	global coordinates of a finite element

Greek letters

Symbol	
α	penalization factor in embedding domain
α	a variable in triangular Toeplitz matrix
$\alpha_1, \alpha_2, \alpha_3$	coefficients for nodally exact solutions
α_p	a variable in triangular Toeplitz matrix in p -FEM
Γ	boundary of Ω
Γ_D	part of the boundary where Neumann conditions are specified
Γ_N	part of the boundary where Dirichlet conditions are specified
δ_{nm}	Kronecker delta
ϵ_0	tolerance for fixed point iteration
ζ	local coordinate of a finite element
ζ_t	Gaussian point of a subcell in cell coordinate
η	local coordinate of a finite element
η_s	Gaussian point of a subcell in cell coordinate
θ	volumetric water content
κ	permeability
$\{\lambda_j\}_{j=1}^N$	eigenvalues of triangle Toeplitz matrix
μ	fluid dynamic viscosity
ν	effective diffusivity
ν_x	effective diffusivity in x -direction
ν_y	effective diffusivity in y -direction
ν_{md}	mechanical dispersion coefficient
$\bar{\nu}$	required diffusivity for nodally exact solutions in linear FEM
$\bar{\nu}_p$	additional diffusivity introduced by p -FEM, with shape functions of polynomial degree p
$\Delta\nu_p$	required diffusivity for nodally exact solutions in p -FEM
ξ	local coordinate of a finite element
ξ_j	local coordinates of the nodes of a one-dimensional Lagrangian finite element basis
ξ_r	Gaussian point of a subcell in cell coordinate
ρ	fluid density
σ	reaction coefficient
Ω	A domain/control volume in \mathbb{R}^n
Ω_e	An embedding domain in \mathbb{R}^n

Calligraphic letters

Symbol

$\mathcal{B}(\cdot, \cdot)$	bilinear form
$\mathcal{B}_e(\cdot, \cdot)$	bilinear form in the embedding domain
$\mathcal{C}(\cdot, \cdot)$	convection related non-symmetric bilinear form
$\mathcal{D}(\cdot, \cdot)$	diffusion related symmetric bilinear form
$\mathcal{F}(\cdot)$	linear form
\mathcal{M}	mass-related symmetric bilinear form
\mathcal{S}	trial function space
\mathcal{S}^γ	discretized trial function space
$\mathcal{S}_{\mathcal{H}}^\gamma$	discretized test function space
\mathcal{V}	test function space
\mathcal{V}^γ	discretized test function space

Mathematical symbols

Symbol

\forall	for all
\cdot	scalar product
$(\cdot)'$	$\frac{d(\cdot)}{dx}$
$\frac{\partial(\cdot)}{\partial x}$	partial derivative of (\cdot) with respect to x
∇	gradient operator
$ \cdot $	absolute value
$\ \cdot\ _{E(\Omega)}$	energy norm
$\ \cdot\ _1$	Sobolev norm
$\ \cdot\ _{L_2(\Omega)}$	L_2 -norm

Chapter 1

Introduction

The thorough understanding of contaminant transport behavior in the flow of groundwater is a challenging prerequisite in the face of increasingly serious environmental problems. The underlying physics of the contaminant transport can be modeled and described using the groundwater flow equation and analyzed by solving the governing equation analytically or numerically. The transport behavior in groundwater flow can be modeled mathematically using the groundwater equation, which is based on the convection-diffusion equation. When there is a chemical reaction between different species, the equation also includes a coupled reaction term serving as a source term.

Since the analytical solution is only applicable for simple boundary value problems, the numerical solution is more feasible and preferable in most real-life problems. The Finite Element Method (FEM), one of the most popular numerical methods, has a powerful track record in solving complex domain problems with a high degree of accuracy. In this thesis, we will deal with two of the major challenges facing the finite element analysis for groundwater problems:

1. The geometry of the domain is complicated by impervious materials;
2. The dominance of the convection flux with respect to the diffusion flux may cause non-physical oscillations;

In hydrogeology, groundwater flow models are used to describe the water contained in the saturated zone (such as aquifers and aquitards etc.), which is located beneath the water table. An aquifer is a pervious geological formation that allows a great amount of water to move through it. An aquitard is a semi-pervious geological formation and has a relatively low permeability compared to an aquifer [4]. Figure 1.1 shows the schematic structure of the underground area, where pervious and impervious materials are distributed in a random manner.

Impervious materials enable a very slow rate of flow, or no flow at all, so the domain containing impervious material should be excluded from the physical domain, which makes the domain complex. The intrinsic permeability of different strata layers and materials are shown in Table 1.2 ([66], modified from [4]).

Since flow patterns in groundwater are highly influenced by the irregular distribution of materials through which the flow passes, it is a particularly demanding challenge to generate

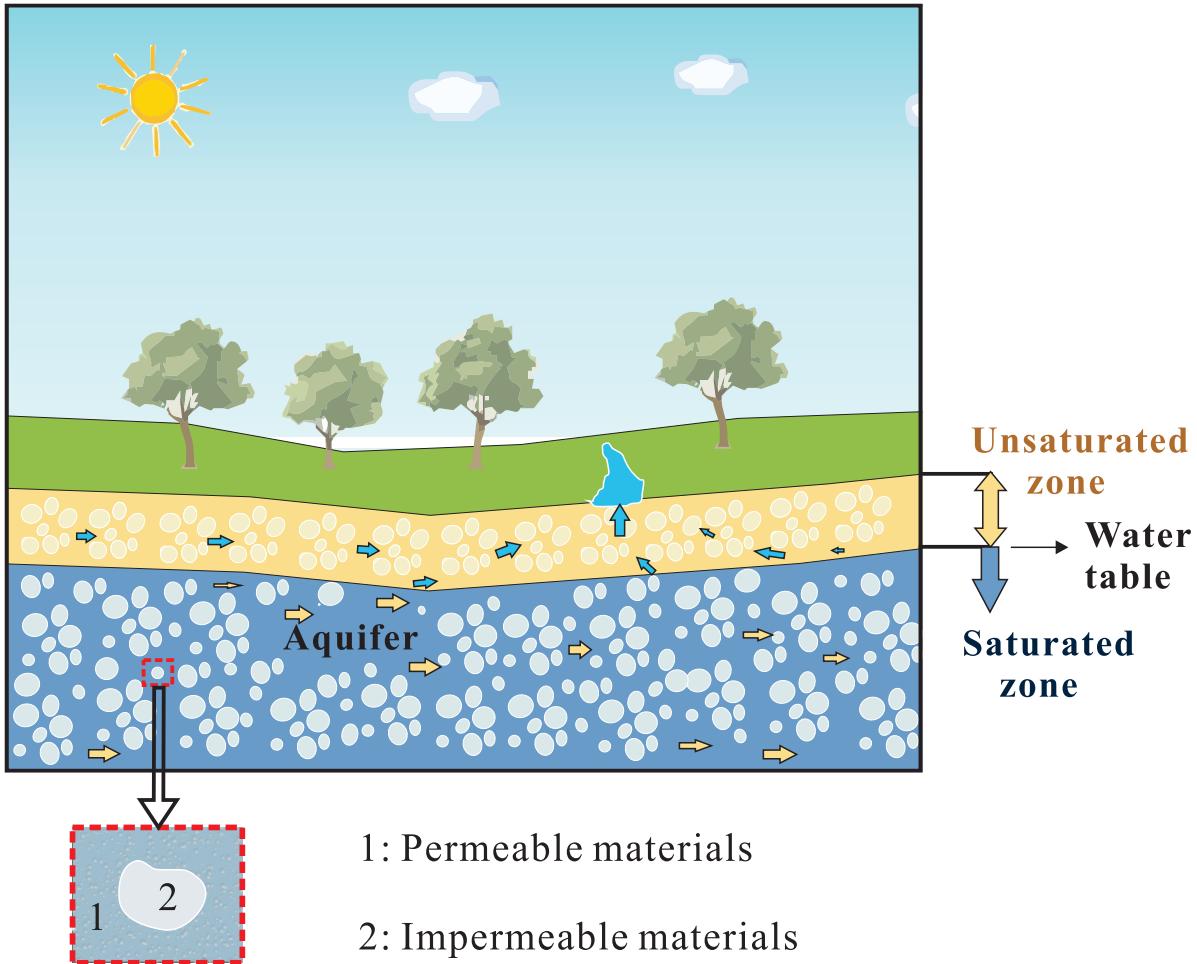


Figure 1.1: Permeable and impermeable materials in groundwater flow

boundary-conforming finite element meshes for the complex domain. During the past few decades, a lot of effort has therefore been invested in developing numerical simulation techniques for highly complex domains of computation, which dispense with the need to generate body-fitted meshes. The methods can be roughly classified as follows:

1. the extended finite element method (XFEM), with variation in the generalized finite element method (GFEM) or partition of unity method (PUM);
2. meshless or mesh-free methods;
3. embedding or fictitious domain methods, often also denoted as immersed boundary methods.

XFEM was first proposed in 1999 [46] to alleviate shortcomings in the finite element method for problems containing singularities. In this method, the standard finite element approximation space is enriched locally by functions enabling a precise approximation of discontinuities within elements [54]. In the field of fluid mechanics, XFEM has been applied to immiscible

Permeability	Pervious				Semi-Pervious				Impervious				
Unconsolidated Sand & Gravel	Well-Sorted Gravel		Well-Sorted Sand or Sand & Gravel		Very Fine Sand, Silt, Loess, Loam				Unweathered Clay				
Unconsolidated Clay & Organic					Peat		Layered Clay			Unweathered Clay			
Consolidated Rocks	Highly Fractured Rocks				Oil Reservoir Rocks			Fresh Sandstone		Fresh Limestone, Dolomite		Fresh Granite	
$\kappa(cm^2)$	10^{-3}	10^{-4}	10^{-5}	10^{-6}	10^{-7}	10^{-8}	10^{-9}	10^{-10}	10^{-11}	10^{-12}	10^{-13}	10^{-14}	10^{-15}
$\kappa(\text{millidarcy})$	10^8	10^7	10^6	10^5	10^4	10^3	10^2	10	1	10^{-1}	10^{-2}	10^{-3}	10^{-4}

Figure 1.2: Intrinsic permeability of different strata and subsoil materials in terms of groundwater flow [66]

two-phase flows, where jumps in the concentration appear across the interfaces between the phases. Chessa [11] applies the XFEM to two-phase fluids to solve the Navier-Stokes equation. The discontinuity in the velocity field is captured by enriching the process with basis functions whose gradient is discontinuous at the interface. Another approach is the intrinsic XFEM [21], enriching the shape functions locally without the introduction of additional global unknowns. All these methods are designed to dispense with the task of resolving geometric features using mesh generation and to extend the Ansatz spaces for the numerical approximation instead.

Meshless (sometimes called mesh-free) methods discretize the computational domain with a set of nodal points only, instead of classical elements [10]. One origin of these concepts is the smooth particle hydrodynamics method, which was first used for modeling astrophysical phenomena without exterior boundaries [42]. Extensive development has been carried out, leading to a number of variants, among which the element-free Galerkin method [5] and the radial point interpolation method [40] are the most relevant in the context of this paper. The element-free Galerkin method has been applied to advection-dispersion transport through saturated porous media [38]. The Galerkin weak form of the governing equation is formulated using mesh-free shape functions constructed by moving least square approximation. The radial point interpolation method employs the Galerkin weak form and radial basis shape functions which are constructed solely on the basis of a group of nodes. It has also been applied in the transportation of contaminants through saturated porous media [39].

The principle of fictitious or embedding domain methods was introduced by Hyman [35] as long ago as the 1950s and later by Saul'ev [55]. They have recently become the focus of

considerable attention again [47, 3, 13, 22]. The common idea of all these approaches is to extend the original physical domain to a larger but geometrically simpler region, which is then discretized in a structured mesh (very often by a Cartesian grid) independent of the original boundary. The methods differ in their approach to implicitly capture the physical domain of computation. Many fictitious domain methods with different features have been explored for fluid problems. Glowinski [23] presents a Lagrange multiplier-based approach to simulate fluid-particle motion. The core feature of this method is to introduce a Lagrange multiplier function to enforce constraints at the interface between fluid and particles. Ramiere [49] solves convection-diffusion problems using fictitious domain methods which are able to simulate free-boundaries undergoing transient deformations. The fat boundary method is proposed by Maury [45] to solve elliptic problems in domains with holes. The method aims at achieving the global resolution on a coarse Cartesian mesh and is capable of an accurate approximation of the solution in the neighborhood of the holes by local refinement. Vos [64] demonstrates the good performance of this method for fluid-structure interaction problems. In a partitioned, strong coupling fluid-structure framework, Wall [65] developed two fixed grid methods by combining them with a) XFEM and b) Arbitrary Lagrangian Eulerian (ALE) based methods coupled with the Chimera approach.

The Finite Cell Method (FCM), recently proposed in [48, 18] was first applied in solid mechanics. It employs the basic concept of fictitious domain approaches, but extends them to high order Ansatz spaces familiar from the p -version of the Finite Element Method [60]. Here, the physical domain is recovered by a trivial continuation of the Galerkin weak form to the fictitious domain and a refined integration of element matrices is performed. The method has been investigated for linear elasticity problems [18], geometrically nonlinear problems [57, 56] and thin-walled, shell-like structures [51]. Although the true boundary of the physical domain is disregarded, the FCM inherits the superior approximation properties of high order finite element methods. It even shows an exponential rate of convergence, provided there are no singularities in the exact solution. Moreover, due to the simple algorithmic structure, it is possible to achieve a highly efficient implementation of the method, even allowing interactive numerical simulation [69, 68]. In this thesis, the FCM is extended to problems of steady convection-diffusion mass transport problems in porous media.

Another topic discussed in this thesis is the high order FEM for convection-diffusion problems, which is also a fundamental basis of FCM. Standard Bubnov-Galerkin finite elements are known to deliver oscillating solutions for convection-dominated problems for meshes that are not fine enough. It has not yet been proven whether raising the polynomial degree of the shape functions will increase or decrease numerical oscillations. The research result described in this thesis will show that increasing the polynomial degree stabilizes the numerical oscillations in Bubnov-Galerkin type finite elements naturally, without the addition of any stabilization term.

Many stabilized finite element methods that can effectively eliminate numerical oscillations have been proposed in the wider body of literature. One of these methods is the streamline upwind Petrov-Galerkin method (SUPG) [7, 33]. It achieves stability by adding extra artificial diffusion, which needs to be modeled explicitly. Alternatively, the local projection stabilization (LPS) [6, 44, 37] may be used. The LPS method suppresses numerical oscillations without refining the mesh or enriching the finite element space. It is necessary to choose locally con-

structured stabilization parameters instead. Other methods, such as the orthogonal subgrid scale (OSS) [12], Galerkin least-squares (GLS) [25], residual-free bubble(RFB) [53], discontinuous Galerkin methods [26], and the variational multi-scale method (VMS) [29, 31, 32] provide a wealth of remedies for the curse of artificial oscillation in convection-dominated problems which are usually applied in lower order finite elements.

For convection-diffusion problems discretized by high order finite element methods (also referred to as p -FEM), Tobiska [62] developed a new stabilized approach combining p -FEM and the VMS approach. Roos *et al.* [52] stated that a better behavior of higher order polynomial degrees has been observed in numerical experiments than in their linear counterparts. [41] looks at the high order finite element method together with SUPG and shock-capturing stabilization. Nevertheless, to the author's knowledge, the p -FEM without any stabilization term has not been systematically analyzed so far for convection-diffusion problems. This thesis aims to analyze the stabilization capacity of pure p -FEM from the numerical and mathematical point of view.

The layout of the thesis is as follows:

Chapter 2 recalls the relevant basic equations in fluid mechanics. The governing transport equation in groundwater flow is then derived and extended for multi-component reactive transport problems. Basic principles of the Finite Difference Method and Finite Element Method are introduced as well as the corresponding discretization schemes.

Chapter 3 describes the High Order Finite Element Method (or p -FEM) and its application in transport problems. Numerical examples show that the p -FEM limits the artificial oscillations in convection-dominated problems for both single- and multi-component, rather than increasing them. As we will show, not only does the numerical scheme remain stable for an extended range of *Péclet* numbers, but the solution also converges exponentially to the exact solution when the polynomial degree is increased.

Chapter 4 explains the stabilization capability of the p -FEM mathematically by analyzing stiffness matrices and their eigenvalues. A straightforward p -FEM extension naturally decreases the truncation error introduced by the linear Bubnov-Galerkin discretization for convection-dominated problems. We also derive, which polynomial degree is sufficiently high to completely eliminate numerical oscillations at nodes.

Chapter 5 introduces the Finite Cell Method and its application in transport problems in porous media. As a combination of the p -FEM and fictitious domain method, FCM provides an attractive approach to solve the groundwater flow problems.

Chapter 2

Numerical simulation in fluid mechanics

2.1 The basic equations of fluid mechanics

In this section, we recall the basic equations of fluid mechanics in differential and integral forms, which will later serve as fundamental equations in the numerical discretization approach.

One of the most fundamental and representative statements of fluid mechanics in an incompressible fluid is the conservation law. The general conservation law states that no quantity in an isolated fluid system can be created or destroyed in the absence of sources or sinks [27]. According to the property of the conserved quantity, the conservation law can be classified under the scalar conservation law, and the vector conservation law. Moreover, the mass and energy conservation equation are derived from the scalar conservation law and the momentum conservation equation comes from the vector conservation law, see Figure 2.1. In this thesis, the main differential equation that we are dealing with is the convection-diffusion equation, which is derived from scalar conservation law.

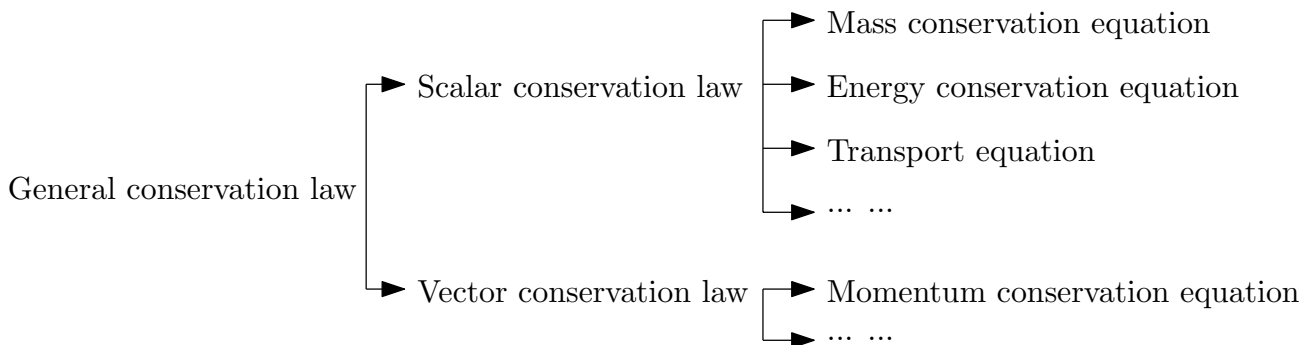


Figure 2.1: The classification of the general conservation law

2.1.1 The conservation law for a scalar quantity

Considering a control volume Ω in Figure 2.2, the conservation law balances the rate of change of a conserved scalar quantity U inside Ω , the rate of U crossing the control surface S and the contribution from any source (or sink) of U [27].

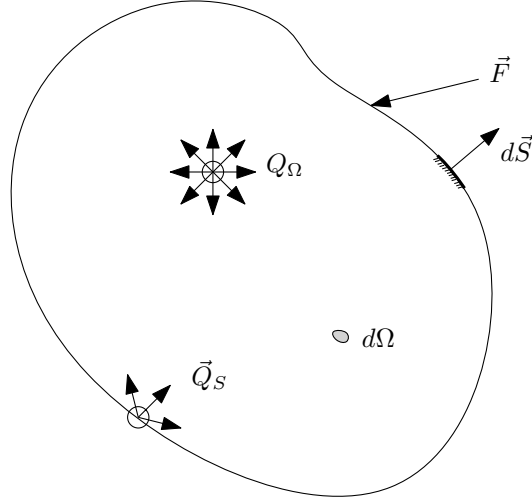


Figure 2.2: Illustration of the conservation law for a scalar quantity

The rate of change of U inside the control volume is the volume integral

$$\frac{d}{dt} \int_{\Omega} U d\Omega = \int_{\Omega} \frac{\partial U}{\partial t} d\Omega. \quad (2.1)$$

The amount of U crossing the unit of surface per unit of time is called flux, a directional quantity denoted by \vec{F} . The rate of U crossing the control surface is accordingly the surface integral

$$\oint_S \vec{F} \cdot d\vec{S}.$$

In the presence of the volume source (or sink) term $\int_{\Omega} Q_{\Omega} d\Omega$ and the surface source (or sink) term $\oint_S \vec{Q}_S \cdot d\vec{S}$, the general conservation equation reads

$$\int_{\Omega} \frac{\partial U}{\partial t} d\Omega + \oint_S \vec{F} \cdot d\vec{S} = \int_{\Omega} Q_{\Omega} d\Omega + \oint_S \vec{Q}_S \cdot d\vec{S}. \quad (2.2)$$

Applying the divergence theorem to transform the volume integral to the surface integral, Equation 2.2 becomes

$$\int_{\Omega} \frac{\partial U}{\partial t} d\Omega + \int_{\Omega} \nabla \cdot \vec{F} d\Omega = \int_{\Omega} Q_{\Omega} d\Omega + \int_{\Omega} \nabla \cdot \vec{Q}_S d\Omega. \quad (2.3)$$

When the fluxes are differentiable – at least C^1 continuous, Equation 2.3 is also valid in an infinitely small control volume, where we obtain the differential form of the conservation law

$$\frac{\partial U}{\partial t} + \nabla \cdot \vec{F} = Q_\Omega + \nabla \cdot \vec{Q}_S. \quad (2.4)$$

Equation 2.4 can be interpreted as the mass or energy conservation equation when the scalar quantity U is replaced by the fluid density ρ or the total energy density ρE , respectively. For another conserved quantity c , where c stands for the concentration of a certain quantity, Equation 2.4 becomes a general conservative form of the transport equation, which is also referred to as the convection-diffusion equation based on its physical property.

2.1.2 Convection-diffusion equation

Substituting the conserved quantity c in the place of U , Equation 2.4 becomes

$$\frac{\partial c}{\partial t} + \nabla \cdot \vec{F} = Q_\Omega + \nabla \cdot \vec{Q}_S \quad \text{in } \Omega. \quad (2.5)$$

The name of Convection-diffusion equation comes from the flux \vec{F} in Equation 2.5, which has mainly two components

1. Convective flux \vec{F}_C
2. Diffusive flux \vec{F}_D

The convective flux \vec{F}_C is the flux transported along with the fluid due to the bulk motion of the fluid. For example, the impurities or pollutants upstream can be transported along the river and found downstream after a certain time. The convective flux describes the physical phenomena with directional properties and is proportional to the velocity \vec{a} and the concentration c .

$$\vec{F}_C = \vec{a}c \quad (2.6)$$

The diffusive flux \vec{F}_D results from the random motion of molecules or the random eddies arising in turbulent flow. The former process is called molecular diffusion and the latter eddy or turbulent diffusion.

As is depicted in Figure 2.3(a), molecules in fluid move randomly at any moment. Let us suppose that there are two regions with a different concentration in fluid. Assuming an identical molecular propensity to move in any direction, the number of molecules moving from the region of higher concentration to that of a lower concentration is greater than the other way around. After a certain time, the quantity consequently moves from a higher concentration to a lower one. Molecular diffusion occurs independent from the bulk motion of the fluid. For instance, if we put a certain amount of salt in a cup of water, the salt spreads evenly through

the water after a while without being stirred. Molecular diffusion flux can be computed using Fick's first law, derived by Adolf Fick in the year 1855.

Fick's first law relates the diffusive flux to the gradient of the concentration and can be expressed as

$$\vec{F}_D = -\nu \nabla c, \quad (2.7)$$

where ν is the diffusion coefficient with units of m^2/s .

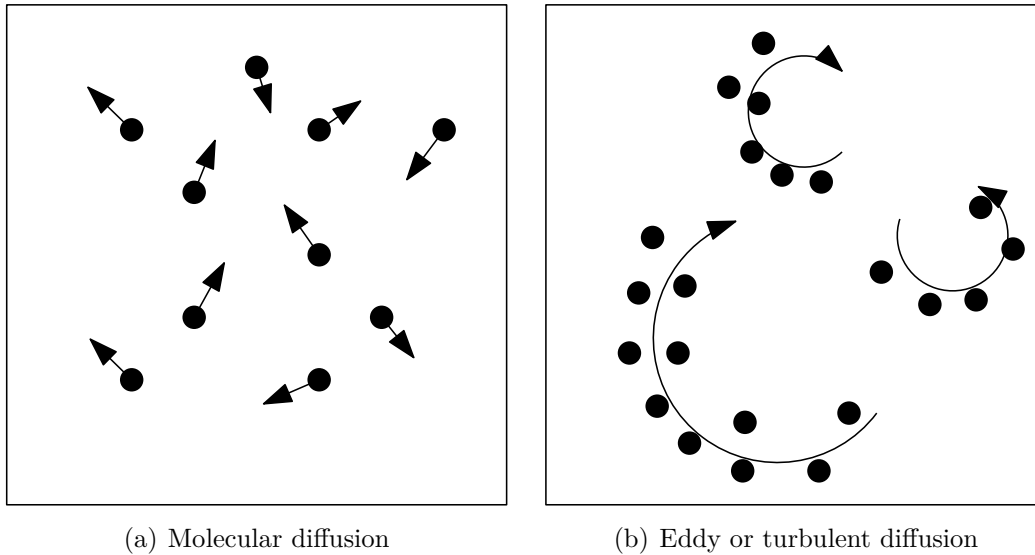


Figure 2.3: Diffusion process in transport problems

In eddy diffusion, the quantity becomes mixed due to the random motion of eddies, see Figure 2.3(b). Eddy diffusion exists in turbulent flow and occurs much more rapidly than molecular diffusion. Turbulent flow is characterized by the Reynolds Number Re defined in Equation 2.8 [58].

$$Re = \frac{\rho \bar{u} L}{\mu} \quad (2.8)$$

where ρ is the fluid density, \bar{u} is the mean velocity, L is the characteristic length and μ is the dynamic viscosity. Turbulent flow occurs when Re approaches the critical level, for example, $Re_{crit} = 4000$ in [28]. Although the eddy diffusion coefficient has a different value than the molecular one, the flux can be also computed using the same formula as Fick's first law.

Another diffusion-like process is called mechanical dispersion. The blending of the quantity is caused by variations either in the velocities in Figure 2.4(a) or in the flow pathways in Figure 2.4(b).

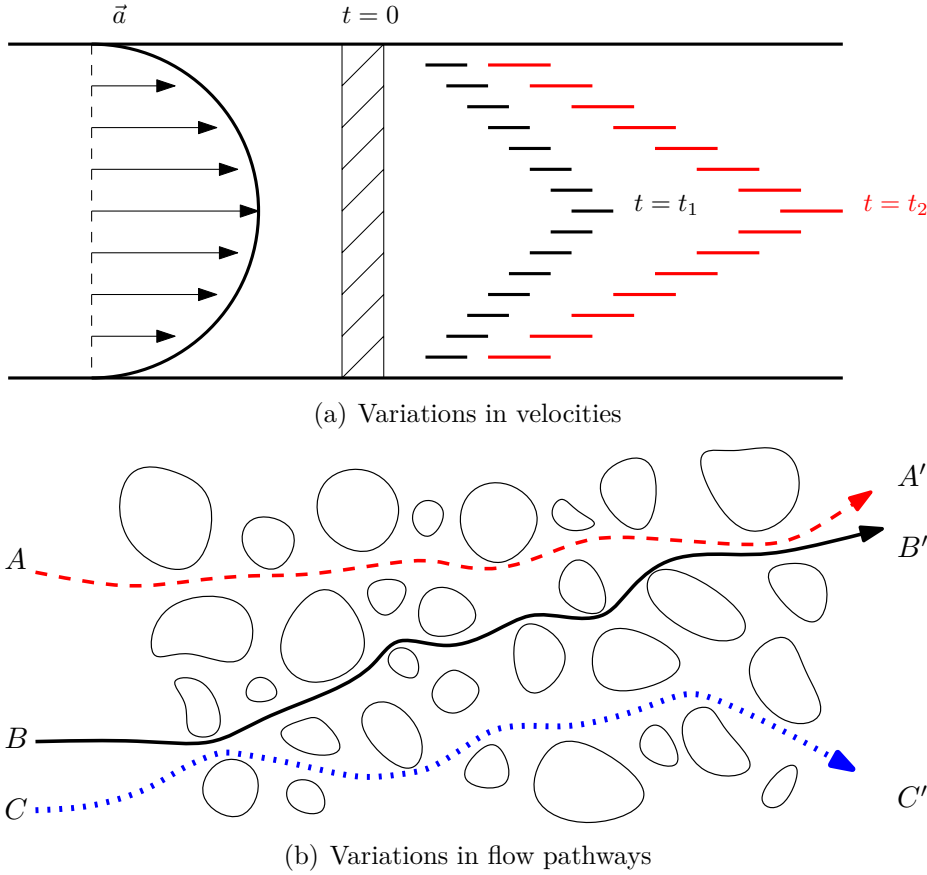


Figure 2.4: Mechanical dispersion process in transport problems

The velocity in fluid varies when the flow comes in contact with other stationary objects. For instance in a round pipe flow, the velocity in the cross-sectional area depends on the diameter of the pipe. The flow is fastest at the center of the pipe and slowest at the point of contact with the pipe. As shown in Figure 2.4(a), due to differences in the speed of flow, the solute is spread out in the longitudinal direction – i.e. in the direction of flow.

Variations in flow pathways happen in porous media, for example in groundwater flow, where the path of the flow changes due to the structure of the media. Figure 2.4(b) demonstrates that, due to heterogeneities in pore structures, the flow B and C are dispersed and the flow A and B converge after passing through a certain area in the porous layer.

Although the mechanical dispersion process is fundamentally different from the diffusion process, it can be mathematically modeled in a similar way to the diffusion process. Hence, the dispersion flux can be computed in Equation 2.9.

$$\vec{F}'_D = -\nu_{md}\nabla c \quad (2.9)$$

where ν_{md} is the mechanical dispersion coefficient.

In this thesis, the dispersion flux is not considered as a separate item but its value is already included in the general diffusive flux. Substituting the convection and diffusion flux term in Equation 2.5 with Equation 2.6 and Equation 2.7, a generalized convection-diffusion equation is accordingly obtained in Equation 2.10.

$$\frac{\partial c}{\partial t} + \nabla \cdot (\vec{a}c - \nu \nabla c) = Q_\Omega + \nabla \cdot \vec{Q}_S \quad \text{in } \Omega \quad (2.10)$$

To characterize the relative importance of the convection and diffusion flux, we introduce the *Péclet* number, which is named after the French physicist *Jean Claude Eugène Péclet*.

There are up to 10 different *Péclet* number definitions [34] for particular types of problems. In this thesis, we employ the one defined in Equation 2.11, which is called the local or mesh or grid *Péclet* number

$$Pe = \frac{ah}{2\nu}, \quad (2.11)$$

where a is the magnitude of the velocity, h is the mesh size and $h/2$ is accordingly the characteristic length of the mesh. It therefore expresses the ratio between the convection and diffusion flux in relation to the mesh size. Mesh *Péclet* number has a significant meaning in numerical analysis. Many discretization schemes become instable as soon as the mesh *Péclet* number exceeds a certain value.

2.2 Transport equations in groundwater flow

The transport equation in groundwater flow describes the solute transport processes by convection and diffusion flux through an aquifer. It is based on the conservation law of dissolved component concentrations and Darcy's law with the following assumptions [67]:

1. The aquifer material is incompressible
2. The water is incompressible
3. Any external loads on the aquifer are constant
4. The groundwater is flowing slowly (Reynolds number less than unity)
5. The hydraulic conductivity is an isotropic scalar

The groundwater flow equation of a single component concentration c reads:

$$\begin{aligned} \theta \frac{\partial c}{\partial t} + \nabla \cdot (\vec{a}c - \theta \nu \nabla c) &= f & \text{in } \Omega \\ c &= c_D & \text{on } \Gamma_D \\ \vec{n} \cdot \nu \nabla c &= c_N & \text{on } \Gamma_N \end{aligned} \quad (2.12)$$

where Γ_D is the Dirichlet boundary, Γ_N is the Neumann boundary, θ is volumetric water content, \vec{a} is the convection velocity and f is the source or sink term. The volumetric water content is the quantity of water contained in porous medium on a volumetric basis. Assuming that V_l , V_s , V_p and V_t are the volumes of the liquid, solid, pore and total phase in this porous medium, respectively, the volumetric water content θ can be computed using Equation 2.13

$$\theta = \frac{V_l}{V_s + V_p} = \frac{V_l}{V_t}. \quad (2.13)$$

On the other hand, the volumetric water content is the product of total porosity P_t and saturation ratio R_s

$$\theta = P_t \cdot R_s = \frac{V_p}{V_t} \cdot \frac{V_l}{V_p} = \frac{V_l}{V_t}. \quad (2.14)$$

which has the same result as Equation 2.13. Convection velocity \vec{a} in the groundwater flow is computed based on Darcy's law, which is elaborated in the following section.

2.2.1 Darcy's law

Darcy's law describes the relationship between the volumetric flow rate and the pressure drop over a given distance in a porous medium. It was experimentally obtained in 1856 by a French engineer named Henry Darcy [36]. He set up the equipment, which is depicted in Figure 2.5, and employed a sand filter as the porous medium.

The results of the experiment showed that the volumetric flow rate or flux $Q(m^3/s)$ is correlated with the length $L(m)$ and cross-sectional area $A(m^2)$ of the sand filter as well as the difference between upper and lower height $h_1 - h_2(m)$ in manometers. By introducing the hydraulic conductivity $K(m/s)$, the results can be formulated as

$$Q = \frac{KA(h_1 - h_2)}{L}. \quad (2.15)$$

Hydraulic conductivity K is directly proportional to the permeability $\kappa(m^2)$ of the porous medium, the weight of the fluid $\rho g(N/m^3)$ and inversely proportional to the fluid dynamic viscosity $\mu(N \cdot s/m^2)$. The mathematical formula accordingly reads:

$$K = \frac{\kappa \rho g}{\mu}. \quad (2.16)$$

where permeability κ is the property of porous medium and measures the fluid's ability to pass through the medium. Combining Equation 2.15 and 2.16, the general form of Darcy's law is obtained in one dimension

$$q = -\frac{\kappa p_1 - p_2}{\mu L}, \quad (2.17)$$

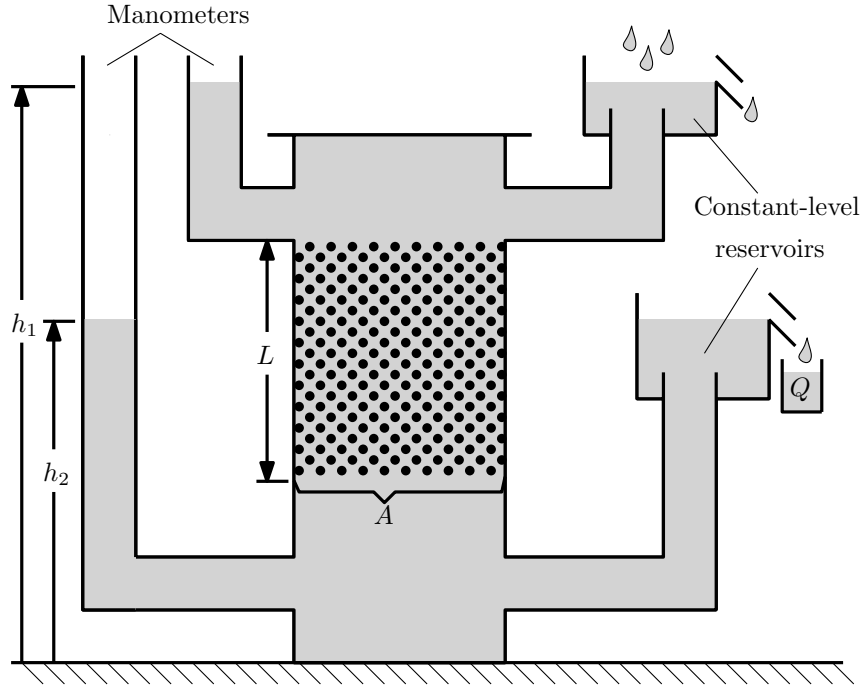


Figure 2.5: The equipment employed in Darcy's experiment

where $q(m/s)$ is the flux per unit area and the product of ρgh is replaced by the pressure p . The minus sign is introduced here to indicate that the fluid flows in the direction of decreasing pressure p . With the same unit as velocity, q is called Darcy velocity or Darcy flux. Darcy velocity q is not a real fluid velocity at any specific point, but it describes the average velocity over the cross-sectional area in porous medium. Since the flows cannot pass through the solid part of porous medium, Darcy velocity is related to the pore velocity v by the factor of porosity P_t .

$$v = \frac{q}{P_t} = \frac{q}{V_p/V_t} \quad (2.18)$$

With a wide range of parameters, it is experimentally proven that Darcy's law is valid for relatively low flow rates in viscous flow. The range value of the flow rates is limited by Reynold's number Re . In granular porous medium, the flow with a Re lower than 5 is considered as Darcian flow. In fracture media, the critical value of Re is 1000 and non-Darcian flow is defined with a q greater than approximately $6 \times 10^{-3}m/s$ [36]. In fact, most problems in groundwater flow have low a Re and accordingly fall into the category of Darcian flow. Therefore, Darcy velocity q can be considered as convection velocity in groundwater problems.

2.2.2 Multicomponent reactive transport problems

In groundwater flow, for example, in the process of groundwater contamination, more than one dissolved component is transported by convection and diffusion flux. These components are

simultaneously influenced by the chemical reaction or biological transformations with other components. Chemical and biological interactions appear as the source or sink term in the differential equation together with any external contribution. The governing equation in multicomponent reactive transport problems in Equation 2.19 is derived by incorporating reaction terms into general convection-diffusion equations.

$$\theta \frac{\partial c_j}{\partial t} + \nabla \cdot (\vec{a}c_j - \theta \nu \nabla c_j) = \sum_{i=1}^N R_{ij} \quad \text{in } \Omega \quad (2.19)$$

where $c_j [ML^{-3}]$, $j = 1, 2, 3$ is the j th dissolved component concentration and R_{ij} is the c_j related reaction term stemming from chemical or biological interaction. The reaction terms usually depend on dissolved concentrations themselves, which yields a coupled problem.

Let us consider a one-dimensional reactive transport problem in the domain Ω , where three components are coupled together in a first-order reaction network. These three components are Ammonium, Nitrite and Nitrate respectively and the schematic reaction network is illustrated in Figure 2.6.

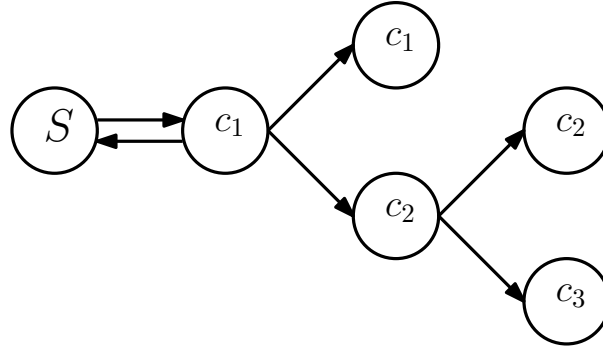


Figure 2.6: Reaction network between three components in the 1D transport problem (schematic)

The relation between sorbed contaminant mass of rock $S [ML^{-3}]$ and concentration of component c_1 can be modeled using the following equation:

$$\frac{\partial S}{\partial t} = K_d \frac{\partial c_1}{\partial t} \quad (2.20)$$

where K_d is the constant adsorption coefficient, which indicates the sorption process of component c_1 on the soil matrix. Accordingly, the governing equation reads

$$\begin{aligned} (1 + K_d) \frac{\partial c_1}{\partial t} &= \nu \frac{\partial^2 c_1}{\partial x^2} - a \frac{\partial c_1}{\partial x} - k_1 c_1 \\ \frac{\partial c_2}{\partial t} &= \nu \frac{\partial^2 c_2}{\partial x^2} - a \frac{\partial c_2}{\partial x} - k_2 c_2 + k_1 c_1 \\ \frac{\partial c_3}{\partial t} &= \nu \frac{\partial^2 c_3}{\partial x^2} - a \frac{\partial c_3}{\partial x} - k_3 c_3 + k_2 c_2. \end{aligned} \quad (2.21)$$

where $k_i[T^{-1}]$, $i = 1, 2, 3$ are reaction coefficients. By applying Dirichlet boundary conditions $c_1 = c_{D1}$, $c_2 = c_{D2}$ and $c_3 = c_{D3}$ for $x = 0$ and $t \geq 0$, the corresponding analytical solutions are derived by Lunn et al. [43], which reads

$$\begin{aligned}
c_1 &= c_{D1}P_1 \\
c_2 &= c_{D2}P_2 + \frac{k_1c_{D1}}{k_2 - k_1} \left\{ P_1 - P_2 + \exp\left(\frac{k_2 - k_1}{K_d}t\right) \left(P\left(\nu, \frac{\mu_2 - \mu^*}{\nu - \nu^*}\right) - P\left(\nu^*, \frac{\mu_2 - \mu^*}{\nu - \nu^*}\right) \right) \right\} \\
c_3 &= c_{D3}P_3 + \frac{k_2c_{D2}}{k_3 - k_2} (P_2 - P_3) + \frac{k_1k_2c_{D1}}{(k_3 - k_2)(k_3 - k_1)(k_2 - k_1)} \times \left\{ (k_2 - k_1)P_3 + (k_1 - k_3)P_2 \right. \\
&\quad \left. + (k_3 - k_2)P_1 \right\} + \frac{k_1k_2c_{D1}}{(k_3 - k_2)(k_2 - k_1)} \times \exp\left\{ \frac{k_2 - k_1}{K_d}t \right\} \left(P\left(\nu, \frac{\mu_2 - \mu^*}{\nu - \nu^*}\right) - P\left(\nu^*, \frac{\mu_2 - \mu^*}{\nu - \nu^*}\right) \right) \\
&\quad - \frac{k_1k_2c_{D1}}{(k_3 - k_2)(k_3 - k_1)} \times \exp\left\{ \frac{k_3 - k_1}{K_d}t \right\} \left(P\left(\nu, \frac{\mu_3 - \mu^*}{\nu - \nu^*}\right) - P\left(\nu^*, \frac{\mu_3 - \mu^*}{\nu - \nu^*}\right) \right),
\end{aligned} \tag{2.22}$$

where

$$\begin{aligned}
\nu^* &= \nu / (1 + K_d) \\
\mu_i &= a^2 / 4\nu + k_i, \quad i = 1, 2, 3 \\
\mu^* &= \mu_1 / (1 + K_d) \\
P(A, \lambda) &= \frac{1}{2} \left(\exp\left(\frac{vx}{2D} - x\sqrt{\lambda}\right) \operatorname{erfc}\left(\frac{x}{\sqrt{4At}} - \sqrt{A\lambda t}\right) + \exp\left(\frac{vx}{2D} + x\sqrt{\lambda}\right) \operatorname{erfc}\left(\frac{x}{\sqrt{4At}} + \sqrt{A\lambda t}\right) \right) \\
P_1 &= P\left(\nu^*, \frac{\mu^*}{\nu^*}\right) \\
P_j &= P\left(\nu, \frac{\mu_j}{\nu_j}\right), \quad j = 2, 3.
\end{aligned}$$

The concentration profiles for three components in Equation 2.22 will serve as reference solutions in numerical analysis. This example will be further investigated numerically as a one-dimensional benchmark problem in Chapter 3.

2.3 Numerical methods in transport problems

As shown in the previous sections, transport problems in fluid mechanics are frequently described mathematically by partial differential equations (PDE), from which it is often impossible to derive corresponding analytical solutions. Various numerical methods are accordingly employed in practice in order to obtain the solutions for real-life problems via numerical approximation. In this section, we introduce two different numerical methods along with their basic theories and applications in transport problems.

2.3.1 Finite difference method

The finite difference method (FDM) was first developed by A. Thom in 1920s under the title "the method of square" to solve nonlinear hydrodynamic equations [61]. FDM solves

differential equations by approximating derivatives numerically using finite differences in the algebraic form. These algebraic forms are derived by means of the Taylor series expansion, which connects a real-valued function to the sum of its derivatives of different orders at a certain point. Compared to the two other methods, FDM is the oldest one and comparatively easy to implement. However, the conservation property of FDM is limited by the size of the grid.

2.3.1.1 Basic theory

FDM discretizes a given function on a grid and its derivatives are approximated from the function values at each grid point. Taylor's theorem states [9]: Let a function $f(x) : \mathbb{R} \rightarrow \mathbb{R}$ be n times differentiable over the interval $I = (a, b)$. For $a < x_0, x_0 + h < b$, the function evaluated at $x = x_0 + h$ has a value

$$f(x_0 + h) = f(x_0) + \frac{f'(x_0)}{1!}h + \frac{f^{(2)}(x_0)}{2!}h^2 + \dots + \frac{f^{(n)}(x_0)}{n!}h^n + O(h^n), \quad (2.23)$$

where

- $f^{(n)} = \frac{d^n f}{dx^n}$
- $f^{(n)}(x_0)$ is the n th derivative of f with respect to x evaluated at $x = x_0$
- $O(h^n)$ is the remainder term, which means that all terms of order n or higher are ignored.

With the value $n = 2$, Equation 2.23 can be rearranged and the first derivative of f has the following expression

$$f'(x_0) = \frac{f(x_0 + h) - f(x_0)}{h} + O(h). \quad (2.24)$$

Based on Equation 2.24, the first order derivative at $x = x_0$ can be approximated by ignoring the remainder term.

$$f'(x_0) \approx \frac{f(x_0 + h) - f(x_0)}{h} \quad (2.25)$$

Equation 2.25 is called a first order forward-difference scheme with the step size h . As shown in Figure 2.7, the derivative of f at grid point P is approximated by the value at the forward grid point B. Similarly, a first order backward-difference scheme is derived in Equation 2.26, where the derivative at P is estimated on the basis of the value at A.

$$f'(x_0) = \frac{f(x_0) - f(x_0 - h)}{h} + O(h) \approx \frac{f(x_0) - f(x_0 - h)}{h} \quad (2.26)$$

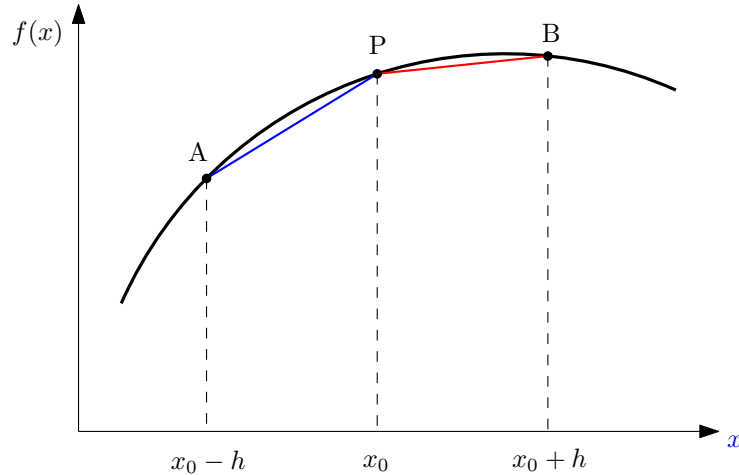


Figure 2.7: The derivatives of f at P can be approximated by forward or backward differences

By adding a forward and backward difference scheme, it is possible to obtain the second order difference scheme in Equation 2.27, which is called the central difference scheme.

$$f'(x_0) = \frac{f(x_0 + h) - f(x_0 - h)}{2h} + O(h^2) \approx \frac{f(x_0 + h) - f(x_0 - h)}{2h} \quad (2.27)$$

The accuracy of FDM is influenced by the order of truncation error in the approximation. Higher order finite difference approximations can be obtained by including more high order terms in Taylor's expansion, which improves the corresponding accuracy of the approximation. Taylor's expansion can be also extended to PDEs with multiple independent variables.

2.3.1.2 Application in mass transport problems

A simple transient linear convection equation in one dimension has the following PDE

$$\frac{\partial c}{\partial t} + a \frac{\partial c}{\partial x} = 0 \quad \text{in } \Omega \times (0, T). \quad (2.28)$$

Partial derivatives with respect to independent variable x and t in Equation 2.28 can be discretized respectively using different discretization schemes. The function is evaluated at the grid points (x_i, t^j) , where constant grid spacing Δx and Δt are applied. With the help of the grid shown in Figure 2.8, the coordinates of evaluation points can be computed in Equation 2.29, where i, j, n are non-negative integers.

$$\begin{aligned} x_{i+n} &= x_i + n \cdot \Delta x \\ t^{j+n} &= t^j + n \cdot \Delta t \end{aligned} \quad (2.29)$$

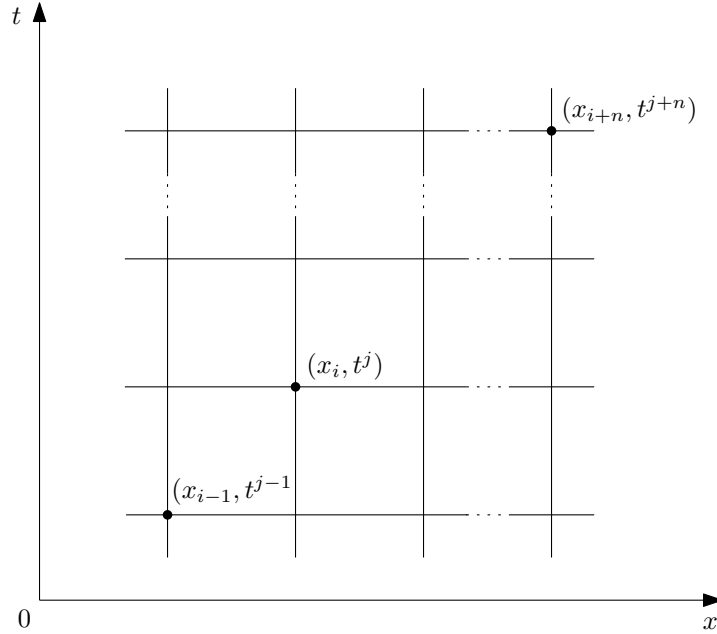


Figure 2.8: Spatial and time variables are approximated independently

Equation 2.28 becomes Equation 2.30 after discretizing the unknown function $c(x, t)$ using forward finite differences, where c_i^j is the abbreviated term for $c(x_i, t^j)$.

$$\frac{c_i^{j+1} - c_i^j}{\Delta t} + a \frac{c_{i+1}^j - c_i^j}{\Delta x} = 0 \quad (2.30)$$

2.3.2 Finite element method

The development of the finite element method (FEM) can be traced back to 1943, when R. Courant discretized a domain into triangles to achieve approximated solutions to Dirichlet problems in vibration systems [63]. The method has also been employed in the field of fluid mechanics since 1970s. FEM discretizes a complex geometry into simpler and disjoint components called finite elements, or elements for short, so that solutions on individual elements can be approximated by shape functions. Compared to the FDM, FEM can handle more complex geometries.

2.3.2.1 Basic principles

Based on Equation 2.10, steady convective-diffusive transport can be described by the following strong form of the boundary-value problem:

Given $f : \Omega \rightarrow \mathbb{R}$ and constant c_D and c_N , find $c : \Omega \rightarrow \mathbb{R}$, such that

$$\begin{cases} \vec{a} \cdot \nabla c - \nabla \cdot (\nu \nabla c) = f & \text{in } \Omega \\ c = c_D & \text{on } \Gamma_D \\ \vec{n} \cdot \nu \nabla c = c_N & \text{on } \Gamma_N, \end{cases} \quad (2.31)$$

where Γ_D is the Dirichlet boundary, Γ_N is the Neumann boundary and \vec{n} is the outward-pointing unit normal vector on the boundary $\Gamma = \partial\Omega$. As a starting point for the finite element method, the strong form of Equation 2.31 is transferred in an integral formulation, the so-called weak form of the PDE.

Consider $u, v : \Omega \rightarrow \mathbb{R}$, where the domain $\Omega \subset \mathbb{R}^n$. The Sobolev space $H^1(\Omega)$ is defined by the inner product in Equation 2.32 and the norm in Equation 2.33 [30].

$$(u, v)_1 = \int_{\Omega} uv + u_{,i}v_{,i}d\Omega, \quad 1 \leq i \leq n \quad (2.32)$$

$$\|u\|_1 = (u, u)_1^{1/2} \quad (2.33)$$

Let the unknown function c be a member of the trial function space $\mathcal{S} = \{c | c \in H^1(\Omega), c = c_D \text{ on } \Gamma_D\}$ and a weighting function w be a member of the test function space $\mathcal{V} = \{w | w \in H^1(\Omega), c = 0 \text{ on } \Gamma_D\}$. The equivalent weak formulation of the strong form in Equation 2.31 is obtained using the divergence theorem under the hypothesis of incompressible flow.

Given $f : \Omega \rightarrow \mathbb{R}$ and constant c_D and c_N , find $c \in \mathcal{S}$, such that for all $w \in \mathcal{V}$

$$\begin{aligned} \int_{\Omega} w(\vec{a} \cdot \nabla c)d\Omega + \int_{\Omega} \nabla w \cdot (\nu \nabla c)d\Omega &= \int_{\Omega} wf d\Omega + \int_{\Gamma_N} wc_N d\Gamma & \text{in } \Omega \\ c &= c_D & \text{on } \Gamma_D \\ \vec{n} \cdot \nu \nabla c &= c_N & \text{on } \Gamma_N. \end{aligned} \quad (2.34)$$

When the divergence theorem is employed, the Neumann boundary condition is automatically included in the weak form. It also implies that, when the homogeneous Neumann boundary condition is given, i.e. $c_N = 0$ in Equation 2.31, the only thing that has to be done is to delete the last term in the weak form.

To make following formulations more convenient, we introduce a compact form of Equation 2.34, which reads

$$\mathcal{C}(w, c) + \mathcal{D}(w, c) = \mathcal{F}(w), \quad (2.35)$$

where

$$\begin{aligned}\mathcal{C}(w, c) &= \int_{\Omega} w(\vec{a} \cdot \nabla c) d\Omega \\ \mathcal{D}(w, c) &= \int_{\Omega} \nabla w \cdot (\nu \nabla c) d\Omega \\ \mathcal{F}(w) &= \int_{\Omega} w f d\Omega + \int_{\Gamma_N} w c_N d\Gamma.\end{aligned}\tag{2.36}$$

Solutions of the weak and strong form are identical when the solutions have the required smoothness [30] of the strong solution. In FEM, the weak form is discretized in finite dimensional spaces $\mathcal{S}^\gamma \subset \mathcal{S}$ and $\mathcal{V}^\gamma \subset \mathcal{V}$ to obtain approximated solutions. Superscript γ can be a function of mesh size h , when these spaces are characterized by the finite element mesh size h , or a function of polynomial degree p , when these spaces are characterized by a polynomial degree of shape functions, or a function of h and p . The weak form is then converted into the following discrete model

Given $f : \Omega \rightarrow \mathbb{R}$, find $c^\gamma \in \mathcal{S}^\gamma$, such that for all $w^\gamma \in \mathcal{V}^\gamma$

$$\mathcal{C}(w^\gamma, c^\gamma) + \mathcal{D}(w^\gamma, c^\gamma) = \mathcal{F}(w^\gamma).\tag{2.37}$$

Here $\mathcal{C}(w^\gamma, c^\gamma)$ is a non-symmetric bilinear form defined on $\mathcal{V}^\gamma \times \mathcal{S}^\gamma$, $\mathcal{D}(w^\gamma, c^\gamma)$ is a symmetric bilinear form defined on $\mathcal{V}^\gamma \times \mathcal{S}^\gamma$ and $\mathcal{F}(w^\gamma)$ is a linear functional defined on \mathcal{V}^γ . The non-symmetric bilinear form \mathcal{C} is related to the convection flux and \mathcal{D} corresponds to the diffusion one.

In pure diffusion problems, the weak equation has an elliptic form and the Bubnov-Galerkin discretization method leads to the best approximated solution c^γ . However, when the convection flux dominates, solutions obtained by means of the Bubnov-Galerkin scheme have spurious oscillations. For this reason, several other stabilization methods have been developed to keep the solution stable. For example, the Streamline Upwind Petrov-Galerkin (SUPG) method can stabilize the solution by introducing an artificial diffusive term. These two different spatial discretization schemes are elaborated in the following sections.

2.3.2.2 The Bubnov-Galerkin discretization

The Bubnov-Galerkin method is one of the most popular spatial discretization schemes, which can convert the continuous problem in Equation 2.35 to the discretized one in Equation 2.37. By expressing test and trial functions using shape functions (or basis functions) of the same discretized, finite dimensional space, the original differential equation becomes an algebraic matrix system, which can then be solved numerically.

As for the continuous problem, a numerical solution can be obtained only if boundary conditions are prescribed. It has been shown in Equation 2.34 that the Neumann boundary condition is naturally included in the weak form, whereas the Dirichlet boundary condition is not.

To impose the Dirichlet boundary condition, the approximated function $c^\gamma \in \mathcal{S}^\gamma$ can be decomposed into two components: an unknown component $c_H^\gamma \in \mathcal{S}_H^\gamma$ and a known component $c_D^\gamma \in \mathcal{S}^\gamma$ which satisfies the prescribed Dirichlet boundary condition. Here space \mathcal{S}_H^γ is also a subset of \mathcal{V} . In other words

$$c^\gamma = c_H^\gamma + c_D^\gamma, \quad (2.38)$$

where

$$\begin{cases} c_H^\gamma = 0 & \text{on } \Gamma_D \\ c_D^\gamma = c_D & \text{on } \Gamma_D. \end{cases} \quad (2.39)$$

By substituting Equation 2.38 into Equation 2.37, we obtain Equation 2.40, which reads

$$\mathcal{C}(w^\gamma, c_H^\gamma) + \mathcal{D}(w^\gamma, c_H^\gamma) = \mathcal{F}(w^\gamma) - \mathcal{C}(w^\gamma, c_D^\gamma) - \mathcal{D}(w^\gamma, c_D^\gamma). \quad (2.40)$$

c_D^γ can be any function in \mathcal{S}^γ . Therefore, the corresponding part is moved to the right-hand side and the value of it is added to the system by enforcing the prescribed Dirichlet boundary condition using, for example, the Penalty method. The next step is to construct a finite dimensional space to approximate w^γ and c_H^γ , respectively.

In the Bubnov-Galerkin discretization, an arbitrary test function space \mathcal{V}^γ can be chosen in such a way that it is the same as \mathcal{S}_H^γ – another subset of the space \mathcal{V} . Let the finite dimensional space \mathcal{V}^γ and \mathcal{S}_H^γ be constructed by the same set of basis functions N_i , $i = 0, 1, 2, \dots, n$. Let us take a one-dimensional convection diffusion problem in $\Omega := (0, l)$ by way of an example. For the sake of simplicity, the Dirichlet boundary condition is applied to the first node: $c(x = 0) = c_D$. The trial function c^γ and the test function w^γ are defined in Equation 2.41.

$$\begin{aligned} c^\gamma &= c_H^\gamma + c_D^\gamma \\ &= \sum_{i=1}^n \hat{c}_i N_i(x) + c_D N_0(x) \in \mathcal{S}^\gamma \\ w^\gamma &= \sum_{j=1}^n \hat{w}_j N_j(x) \in \mathcal{V}^\gamma \end{aligned} \quad (2.41)$$

Here $N_0(x = 0) = 1$ and \hat{c}_i, \hat{w}_i are scalar weights. If the shape functions are piecewise linear, the possible trial and test function are depicted in Figure 2.9. The dashed lines indicate the weighted shape functions at each node that contributed to the trial or test functions.

The Bubnov-Galerkin discretization scheme is known to be optimal for elliptic and parabolic problems due to its orthogonality properties for symmetric bilinear forms. This means that the difference between the approximated solution c^γ under Galerkin discretization and the original solution c is orthogonal to the space \mathcal{V}^γ .

$$\begin{aligned} \mathcal{D}(w^\gamma, c - c^\gamma) &= \mathcal{D}(w^\gamma, c) - \mathcal{D}(w^\gamma, c^\gamma) \\ &= \mathcal{F}(w^\gamma) - \mathcal{F}(w^\gamma) = 0 \end{aligned} \quad (2.42)$$

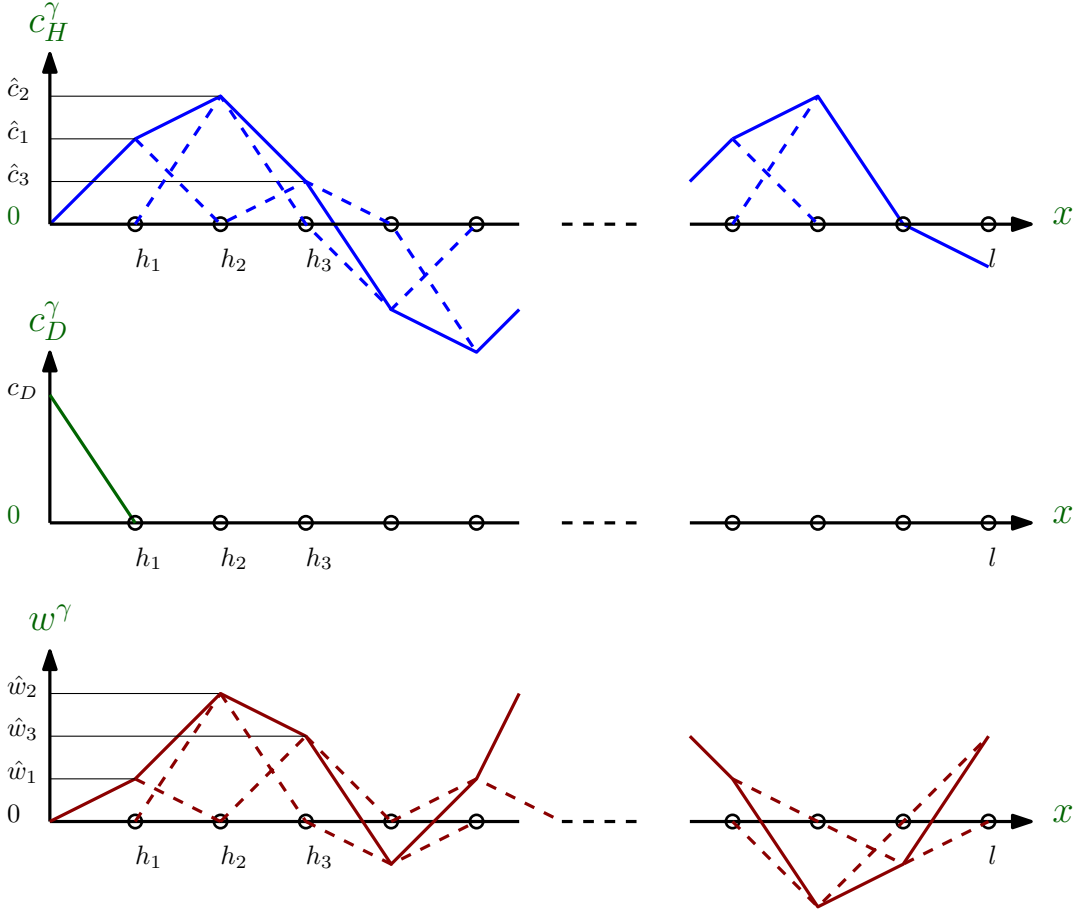


Figure 2.9: Possible trial and test functions using Bubnov-Galerkin discretization

2.3.2.3 The Streamline Upwind Petrov-Galerkin (SUPG) discretization

Due to the non-symmetric convection term, the differential equation does not hold an elliptic or a parabolic form any more. When the convection flux dominates, the Bubnov-Galerkin discretization leads to spurious oscillations in numerical solutions. Many stabilization methods have been developed based upon the standard Bubnov-Galerkin discretization to eliminate non-physical oscillations. An alternative approach to Bubnov-Galerkin schemes is the Petrov-Galerkin method, which assigns different discretization spaces for trial and test functions.

In order to compensate the negative diffusion created by the Bubnov-Galerkin method, we add a non-physical diffusion artificially in SUPG [15]. For example, in a one-dimensional convection-diffusion problem, the weak form of the differential equation

$$\begin{aligned}
 ac'(x) - \nu c''(x) &= 1 \quad \text{on } \Omega := (0, 1) \\
 c(x) &= 0 \quad \text{at } x = 0 \\
 c(x) &= 0 \quad \text{at } x = 1
 \end{aligned} \tag{2.43}$$

is

$$\int_0^1 (wac' + w'(\nu + \bar{\nu})c')dx = 0, \quad (2.44)$$

where

$$\bar{\nu} = \frac{ah}{2}(\coth Pe - 1/Pe). \quad (2.45)$$

The numerical solutions computed by applying the standard Bubnov-Galerkin scheme and the SUPG scheme with different mesh *Péclet* number are compared in Figure 2.10 and Figure 2.11. It can be observed that for both cases $Pe > 1$ and $Pe < 1$, the additional added diffusion of the Petrov-Galerkin scheme will lead the non-oscillatory solution, whereas the Bubnov-Galerkin scheme oscillates for $Pe > 1$. How to obtain this amount of diffusion will be derived in Chapter 4. However, defining the necessary artificial diffusivity for more complicated problems in multi-dimensions will make the numerical analysis more complicated, which is a disadvantage of this method.

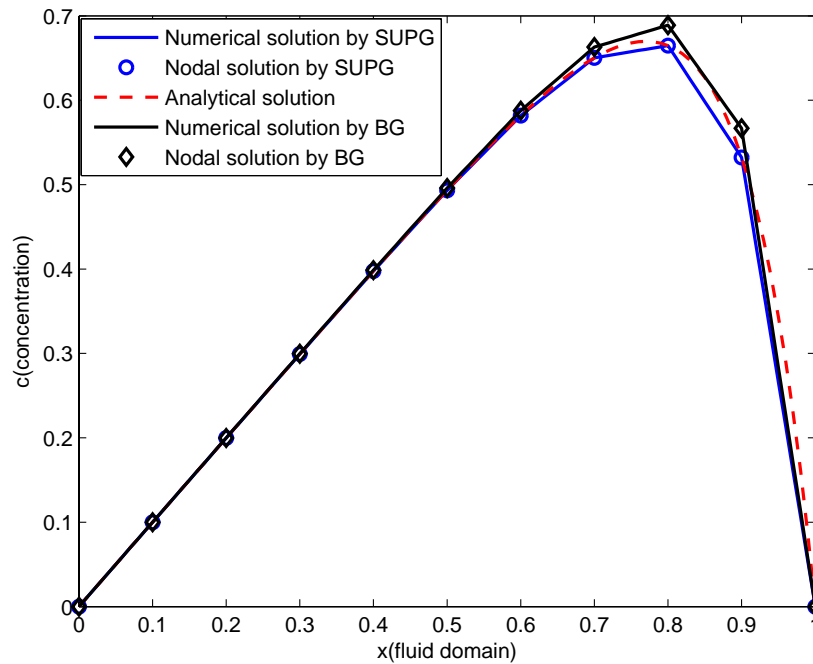


Figure 2.10: Numerical solutions obtained by the Bubnov-Galerkin and the SUPG scheme with $Pe=0.5$

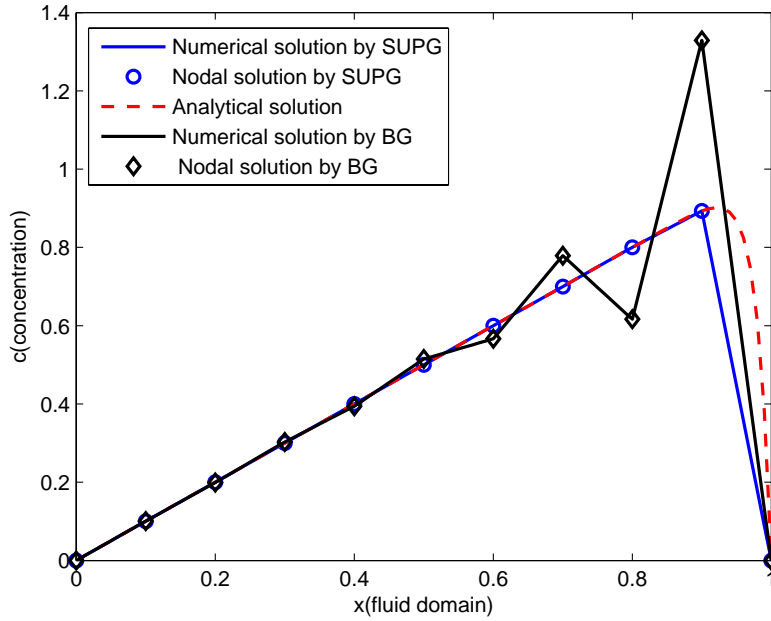


Figure 2.11: Numerical solutions obtained by the Bubnov-Galerkin and the SUPG scheme with $Pe=2.5$

2.3.2.4 Error estimation in different norms

An error estimation process is always necessary in numerical methods, where the quality of the approximated solution can be evaluated in different norms.

A norm is a mapping of a complex or real space A , $\|\cdot\| : A \rightarrow \mathbb{R}$. Let $x, y \in A$ and $\alpha \in \mathbb{R}$, then a norm $\|\cdot\|$ has the following properties [30].

1. Positive definiteness: $\|x\| \geq 0$, and $\|x\| = 0$ if and only if $x = 0$
2. Positive homogeneity: $\|\alpha x\| = |\alpha| \|x\|$
3. Triangle inequality: $\|x + y\| \leq \|x\| + \|y\|$

Consider a domain $\Omega \subset \mathbb{R}^n$, $n > 1$, and let $c, w : \Omega \rightarrow \mathbb{R}$. The s^{th} Sobolev space $H^s(\Omega)$ has the natural norm

$$\|c\|_s = \left(\int_{\Omega} (c^2 + c_{,i}^2 + c_{,ij}^2 + \dots + c_{,ij\dots k}^2) d\Omega \right)^{1/2}, \quad 1 \leq i, j, \dots, k \leq n \quad (2.46)$$

and a seminorm

$$|c|_s = \left(\int_{\Omega} (c_{,ij\dots k}^2) d\Omega \right)^{1/2}, \quad 1 \leq i, j, \dots, k \leq n. \quad (2.47)$$

The only property of a seminorm that is different from a norm is that a seminorm is positive-semidefinite. In this thesis, the relative error in the $L_2(\Omega)$ norm and energy $E(\Omega)$ norm are computed for evaluation of the numerical solutions. The $L_2(\Omega)$ norm is the 0th Sobolev natural norm, which reads

$$\|c\|_{L_2(\Omega)} = \|c\|_0 = \left(\int_{\Omega} (c_{,ij\dots k}^2) d\Omega \right)^{1/2}, \quad 1 \leq i, j, \dots, k \leq n. \quad (2.48)$$

An energy norm is a semidefinite form, defined as

$$\|c\|_{E(\Omega)} = |c|_1 = \left(\int_{\Omega} (c_{,i}^2) d\Omega \right)^{1/2}, \quad 1 \leq i \leq n. \quad (2.49)$$

An error e is the difference between the exact solution c_{ex} and its numerical solution c_{fe} whereas the relative error is e_r the ratio between error and the exact solution. The relative error in the L_2 norm and in the energy norm, respectively, read

$$\|e_r\|_{L_2(\Omega)} = \frac{\|e\|_{L_2(\Omega)}}{\|c_{ex}\|_{L_2(\Omega)}} = \frac{\|c_{ex} - c_{fe}\|_{L_2(\Omega)}}{\|c_{ex}\|_{L_2(\Omega)}}, \quad (2.50)$$

$$\|e_r\|_{E(\Omega)} = \frac{\|e\|_{E(\Omega)}}{\|c_{ex}\|_{E(\Omega)}} = \frac{\|c_{ex} - c_{fe}\|_{E(\Omega)}}{\|c_{ex}\|_{E(\Omega)}}. \quad (2.51)$$

Since it is not generally possible to obtain an exact solution c_{ex} even for model problems, the reference solution in this thesis is obtained by means of a high-resolution mesh with high polynomial degrees for corresponding shape functions. In addition, the relative error in the L_2 or energy norm is approximated by Equation 2.52 and Equation 2.53, computed using an in-house p -FEM code – AdhoC [17].

$$\begin{aligned} \|e_r\|_{L_2(\Omega)} &= \frac{\|c_{ex} - c_{fe}\|_{L_2(\Omega)}}{\|c_{ex}\|_{L_2(\Omega)}} \\ &\approx \frac{\|c_{ex}\|_{L_2(\Omega)} - \|c_{fe}\|_{L_2(\Omega)}}{\|c_{ex}\|_{L_2(\Omega)}} \end{aligned} \quad (2.52)$$

$$\begin{aligned}\|e_r\|_{E(\Omega)} &= \frac{\|c_{ex} - c_{fe}\|_{E(\Omega)}}{\|c_{ex}\|_{E(\Omega)}} \\ &\approx \frac{\|c_{ex}\|_{E(\Omega)} - \|c_{fe}\|_{E(\Omega)}}{\|c_{ex}\|_{E(\Omega)}}\end{aligned}\tag{2.53}$$

It is worth mentioning that Equation 2.53 is only exact in the case of an elliptic problem and the application of a Bubnov-Galerkin scheme, as the Galerkin orthogonality [14] only holds in this constellation. In all other cases, the expression can nevertheless be regarded as a good approximation to the error.

Chapter 3

High Order Finite Element Method (p -FEM)

Discretization in spatial and time domain is a necessary step in FEM to restrict the number of degrees of freedom (DOF) to a finite level. On the other hand, this process introduces an inevitable discretization error, which is one of the most important facts that influence the accuracy of numerical approximations. In order to perform a reliable computation, it is essential to control the discretization error. The obvious solution for decreasing the discretization error is to increase the number of DOF and, when it goes to infinity, the discretization error for a convergent scheme becomes zero. The number of DOF can be increased by simply refining the mesh locally or globally in the h -FEM. In this chapter, we introduce the high order finite element method, also called p -FEM, by way of another discretization strategy and apply it to fluid transport problems. The p -FEM keeps the finite element mesh fixed and increases the number of DOF by raising the polynomial degree of shape functions for elements.

3.1 Basic principles

The basic principles of the p -FEM can be explained using a one-dimensional steady convective-diffusive transport problem with a Dirichlet boundary condition, which reads

Given constant a , ν and f , find $c : \Omega \rightarrow \mathbb{R}$, such that

$$\begin{cases} a \frac{dc}{dx} - \nu \frac{d^2c}{dx^2} = f & \text{on } \Omega = \{x | 0 < x < 1\} \\ c = 0 & \text{at } x = 0 \\ c = 0 & \text{at } x = 1. \end{cases} \quad (3.1)$$

The straightforward application of the Bubnov-Galerkin discretization leads to the corresponding weak form of Equation 3.2

$$\int_0^1 (ac'w + c'\nu w') d\Omega = \int_0^1 f w d\Omega, \quad (3.2)$$

where w is an arbitrary test function and c' and w' are the compact forms of $\frac{dc}{dx}$ and $\frac{dw}{dx}$, respectively. The scalar function c and w are both discretized and approximated by the same shape functions $\{N_i\}_1^{p+1}$. By applying h -FEM, where finite elements are only approximated by linear shape functions, the discretized function c_H^γ at any point in the element $\Omega_j^e = [x_j, x_{j+1}]$ can be expressed as

$$c_H^\gamma(\xi) = N_1(\xi)c(x_j) + N_2(\xi)c(x_{j+1}), \quad (3.3)$$

where ξ denotes the normalized local coordinate, $-1 \leq \xi \leq 1$. The linear shape functions are expressed as

$$\begin{aligned} N_1(\xi) &= \frac{1}{2}(1 - \xi) \\ N_2(\xi) &= \frac{1}{2}(1 + \xi). \end{aligned} \quad (3.4)$$

In p -FEM, the trial and test function can be approximated using higher order polynomials in an elemental area Ω^e . When the set of polynomials is expanded up to the order p , the function c_H^γ is also enriched accordingly.

$$c_H^\gamma(\xi) = N_1(\xi)c(x_j) + N_2(\xi)c(x_{j+1}) + \sum_{i=2}^p N_{i+1}(\xi)a_{i+1} \quad (3.5)$$

Besides the linear functions, the finite element space now contains higher order ones as well, which offers the opportunity to approximate any curved function more efficiently. The linear shape function N_1 , N_2 and second order hierarchic shape function N_3 are schematically drawn in Figure 3.1.

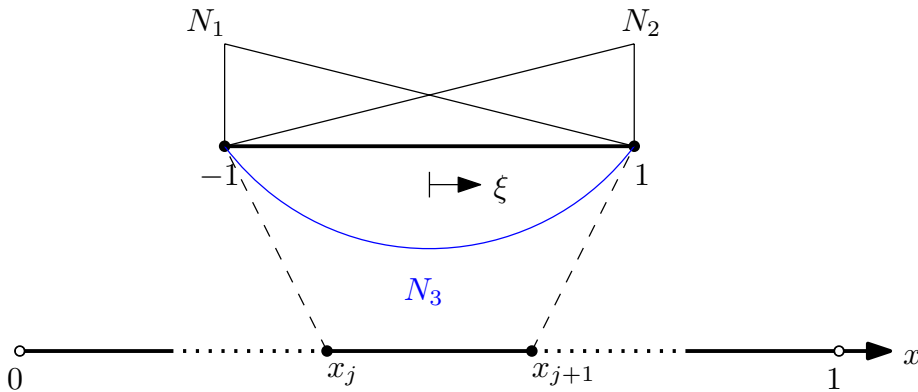


Figure 3.1: Discretization and approximation functions in 1D convection-diffusion problem

3.2 High order shape functions

There is more than one set of the shape functions that can construct the same high order finite element space. To make the computation efficient and convenient, however, it is necessary to take several factors into consideration before any set of the shape functions can be chosen. The shape functions should be easy to implement, for instance, in order to facilitate the process. The ideal case would be: the shape functions with the polynomial degree $p + 1$ contain those with p . In addition, the shape functions should be favorable for the efficient computation of stiffness matrices and load vectors. To satisfy this condition, orthogonal or near-orthogonal shape functions, which can yield diagonal or near-diagonal element stiffness matrices, are preferable.

Lagrange and hierarchic shape functions are two typical shape functions used in the standard finite element approaches, which will be discussed further in the following sections.

3.2.1 Lagrange shape function – nodal expansion

Lagrange shape functions are constructed on the basis of a nodal polynomial expansion. In one dimension, the set of Lagrange polynomials has the form

$$N_i^p(\xi) = \prod_{j=1, j \neq i}^{p+1} \frac{\xi - \xi_j}{\xi_i - \xi_j}, \quad (3.6)$$

where ξ_1, ξ_{p+1} are end nodes and $\{\xi_j\}_2^p$ are internal points of one element. As a notable property, the Lagrange shape function N_i^p has the value 1 at the point ξ_i and 0 at other points $\xi_j, j \neq i$. Consequently, the corresponding coefficient a_i in Equation 3.5 has a physical interpretation: the approximate solution at the point ξ_i . The internal points are called nodes and are usually chosen to be equidistant, i.e.

$$\xi_j = -1 + (j - 1) \frac{2}{p}, \quad j = 1, 2, \dots, p + 1. \quad (3.7)$$

The Lagrange shape functions for the polynomial degree $p = 1, \dots, 6$ are illustrated in Figure 3.2.

It is obvious that, when the polynomial degree is increased, the whole shape function set has to be completely reconstructed, which makes the implementation process inefficient. Another property of the Lagrange shape function is that the sum of all shape functions for a certain polynomial degree is always equal to 1.

3.2.2 Hierarchic shape function – modal expansion

Another choice of the shape function is the hierarchic shape function, which is based on the orthogonal Legendre polynomials.

3.2.2.1 One-dimensional hierarchic shape function

The Legendre polynomials are solutions to Legendre's differential equation, defined in the interval $x \in (-1, 1)$ using Rodrigues' formula

$$L_n(x) = \frac{1}{2^n n!} \frac{d^n}{dx^n} (x^2 - 1)^n, \quad n = 0, 1, 2, \dots \quad (3.8)$$

By definition, the orthogonal Legendre polynomial sequence $\{L_n(x)\}$ is defined in such a way that any two different polynomials in this sequence are orthogonal. In one dimension, the Legendre inner product is zero in the interval $(-1, 1)$

$$\langle L_n(x), L_m(x) \rangle = \int_{-1}^1 L_n(x) L_m(x) dx = \delta_{nm} \frac{2}{2n+1}, \quad (3.9)$$

where δ_{nm} is called Kronecker delta, which has the value

$$\delta_{nm} = \begin{cases} 1 & \text{if } n = m \\ 0 & \text{otherwise.} \end{cases} \quad (3.10)$$

One-dimensional hierarchic shape functions are derived from the integrated Legendre polynomials and defined in [59], for example,

$$\begin{aligned} N_1(\xi) &= \frac{1}{2}(1 - \xi) \\ N_2(\xi) &= \frac{1}{2}(1 + \xi) \\ N_i(\xi) &= \phi_{i-1}(\xi), \quad i = 3, 4, \dots, p+1, \end{aligned} \quad (3.11)$$

where

$$\phi_j(\xi) = \sqrt{\frac{2j-1}{2}} \int_{-1}^{\xi} L_{j-1}(x) dx, \quad j = 2, 3, \dots, p. \quad (3.12)$$

The linear shape functions called $N_1(\xi)$ and $N_2(\xi)$ are nodal modes and $\{N_i(\xi)\}_{i=3}^{p+1}$ are internal modes due to the fact that

$$N_i(-1) = N_i(1) = 0, \quad i = 3, 4, \dots, p+1. \quad (3.13)$$

The hierarchic shape functions for the polynomial degree $p = 1, \dots, 6$ are illustrated in Figure 3.3.

As opposed to the Lagrange shape functions, the enrichment of the hierarchic shape functions from p to $p+1$ maintains all the shape functions up to p and only requires the construction of one more shape function – the internal mode. The hierarchic shape functions are therefore constructed by the modal expansion.

3.2.2.2 Two-dimensional hierarchic shape function

Hierarchic shape functions for quadrilaterals are derived from the Ansatz functions introduced in [59]. The standard quadrilateral finite element is illustrated in Figure 3.4 [16].

The two-dimensional shape functions consist of three modes [16]:

1. **Nodal modes:** The nodal modes

$$N_{1,1}^{N_i}(\xi, \eta) = \frac{1}{4}(1 + \xi_i \xi)(1 + \eta_i \eta), \quad i = 1, \dots, 4 \quad (3.14)$$

are the standard bilinear shape functions, which are familiar from the isoparametric four-noded quadrilateral element. (ξ_i, η_i) denote the local coordinates of the i th node.

2. **Edge modes:** These modes are defined separately for each individual edge; they vanish at all other edges. The corresponding modes for edge E_1 read

$$N_{i,1}^{E_1}(\xi, \eta) = \frac{1}{2}(1 - \eta)\phi_i(\xi). \quad (3.15)$$

3. **Internal modes:** The internal modes

$$N_{i,j}^{\text{int}}(\xi, \eta) = \phi_i(\xi)\phi_j(\eta) \quad (3.16)$$

are purely local and vanish at the edges of the quadrilateral element.

The indices i, j of the shape functions denote the polynomial degrees in the local directions ξ, η .

3.2.2.3 Three-dimensional hierarchic shape function

Hierarchic shape functions in three dimensions are derived for the hexahedral elements illustrated in Figure 3.5 [16].

Analogous to two-dimensional formulations, three-dimensional shape functions can be classified into four groups [16]:

1. **Nodal modes:** The nodal modes

$$N_{1,1,1}^{N_i}(\xi, \eta, \zeta) = \frac{1}{8}(1 + \xi_i \xi)(1 + \eta_i \eta)(1 + \zeta_i \zeta), \quad i = 1, \dots, 8 \quad (3.17)$$

are the standard trilinear shape functions, well known from the isoparametric eight-noded brick element. (ξ_i, η_i, ζ_i) are the local coordinates of the i th node.

2. **Edge modes:** These modes are defined separately for each individual edge. If we consider edge E_1 , for example, the corresponding edge modes read

$$N_{i,1,1}^{E_1}(\xi, \eta, \zeta) = \frac{1}{4}(1 - \eta)(1 - \zeta)\phi_i(\xi). \quad (3.18)$$

3. **Face modes:** These modes are defined separately for each individual face. If we take a look at face F_1 , for instance, the corresponding face modes read:

$$N_{i,j,1}^{F_1}(\xi, \eta, \zeta) = \frac{1}{2}(1 - \zeta)\phi_i(\xi)\phi_j(\eta) \quad (3.19)$$

4. **Internal modes:** The internal modes

$$N_{i,j,k}^{\text{int}}(\xi, \eta, \zeta) = \phi_i(\xi)\phi_j(\eta)\phi_k(\zeta) \quad (3.20)$$

are purely local and vanish at the faces of the hexahedral element.

The indices i, j, k of the shape functions denote the polynomial degrees in the local directions ξ, η, ζ .

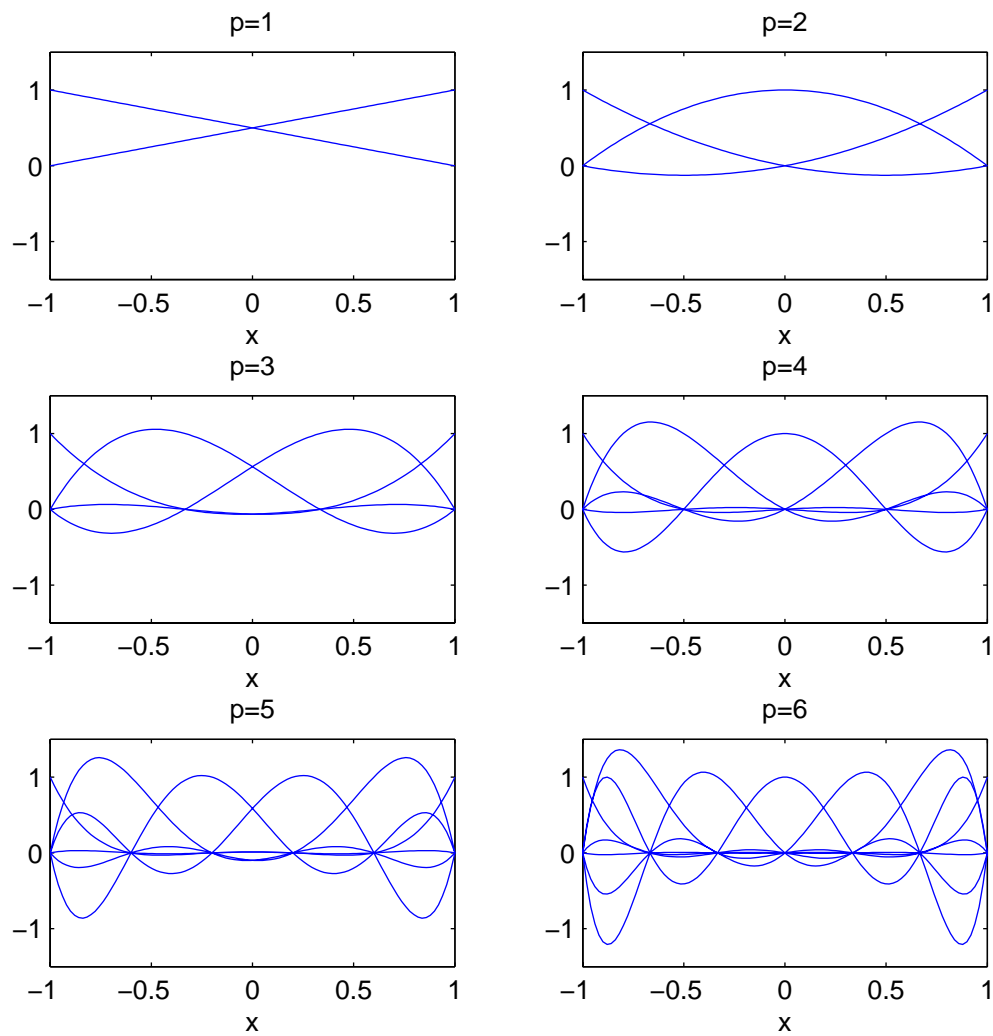


Figure 3.2: One-dimensional Lagrange shape functions, $p = 1, \dots, 6$

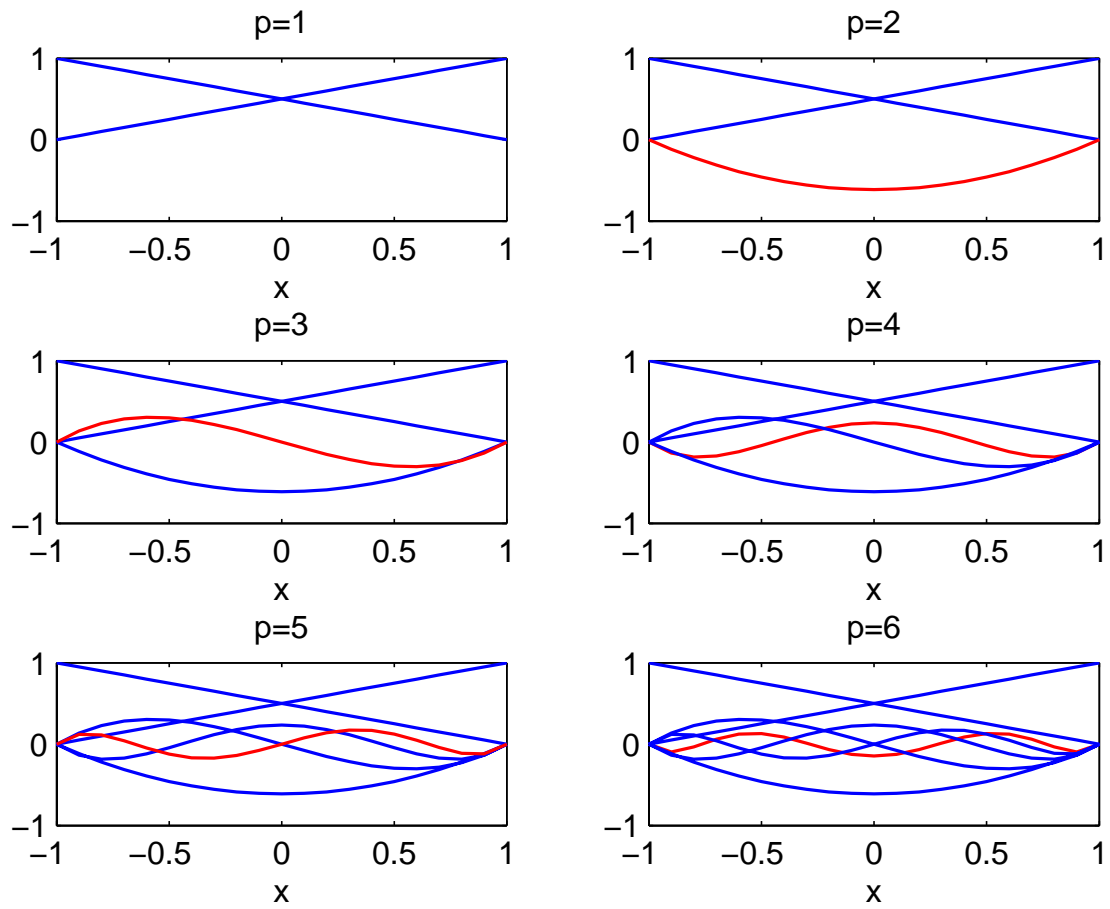


Figure 3.3: One-dimensional Hierarchic shape functions, $p = 1, \dots, 6$

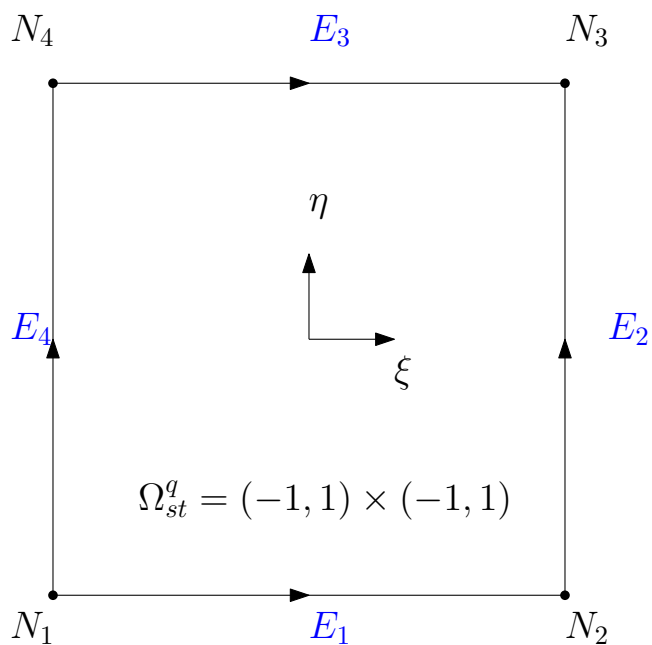


Figure 3.4: Nodes and edges in a standard quadrilateral element

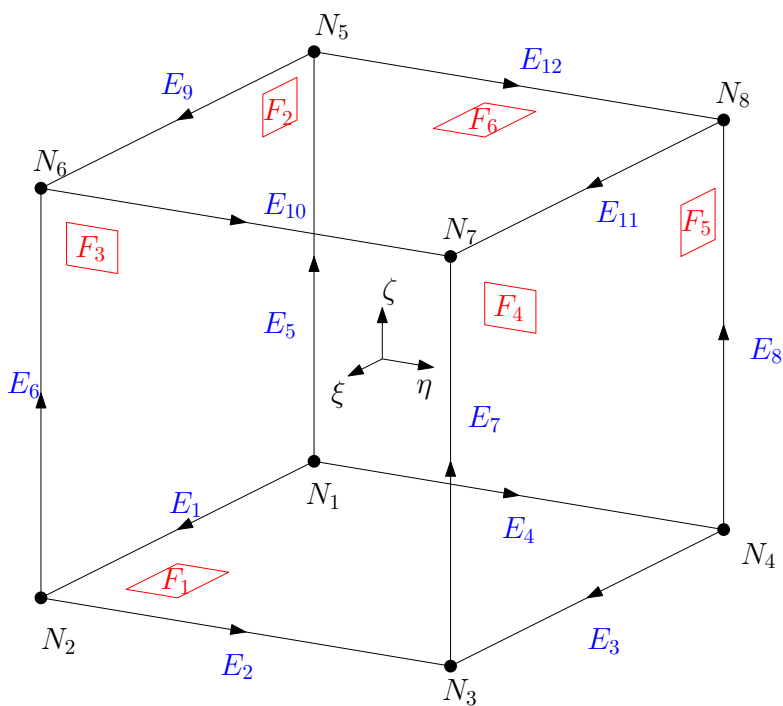


Figure 3.5: Nodes, edges and faces in a standard hexahedral element

3.3 Numerical examples in transport problems

3.3.1 Single-component transport problems

3.3.1.1 One-dimensional simple Dirichlet boundary problem

This section compares the numerical results of the one-dimensional convection-diffusion transport problem with the exact solution. The given differential equation 3.21

$$\begin{cases} a \frac{dc}{dx} - \nu \frac{d^2c}{dx^2} = 0 & \text{on } \Omega = \{x | 0 < x < 1\} \\ c = 0 & \text{at } x = 0 \\ c = 1 & \text{at } x = 1 \end{cases} \quad (3.21)$$

has the analytical solution

$$y = \frac{e^{ax/\nu} - 1}{e^{a/\nu} - 1}. \quad (3.22)$$

When the mesh is fixed, the ratio between velocity and diffusivity determines the *Péclet* number and characterizes the convergence of the numerical solution. When the *Péclet* number increases, the standard Bubnov-Galerkin method based on linear elements exhibits oscillations in the numerical solution. We choose the parameters $a = 2m/h$, $\nu = 0.02m^2/h$, and compute the corresponding numerical solutions with 10 elements of the same length $h = 0.1$. Figure 3.6 shows numerical solutions with different polynomial degrees. The dashed line denotes the exact solution, while the solid line represents the numerical solution.

As expected, when the *Péclet* number $Pe = \frac{ah}{2\nu} = 5$ is larger than 1, the numerical solution with linear Bubnov-Galerkin discretization introduces non-physical oscillations. The *p*-FEM can eliminate these oscillations by simply raising the polynomial degree p . Figure 3.6 shows that, with $p = 7$, the oscillation is drastically suppressed and the numerical solution is in good agreement with the analytical one.

3.3.1.2 Two-dimensional steady rotating pulse problem

Here, the stabilization of the Bubnov-Galerkin finite elements for high order shape functions is demonstrated by means of a two-dimensional diffusion-convection-reaction transport problem with a rotating velocity and a discontinuous source. The well-known partial differential equation reads

$$a \cdot \nabla c - \nabla \cdot (\nu \nabla c) + \sigma c = f, \quad (3.23)$$

where σ is the reaction coefficient. We apply the following boundary conditions $c(x = -1) = c(x = 1) = c(y = -1) = c(y = 1) = 0$ in the domain $\Omega = (-1, 1) \times (-1, 1)$. The velocity field is given as

$$a = \phi(\rho) \begin{pmatrix} -y \\ x \end{pmatrix}, \quad (3.24)$$

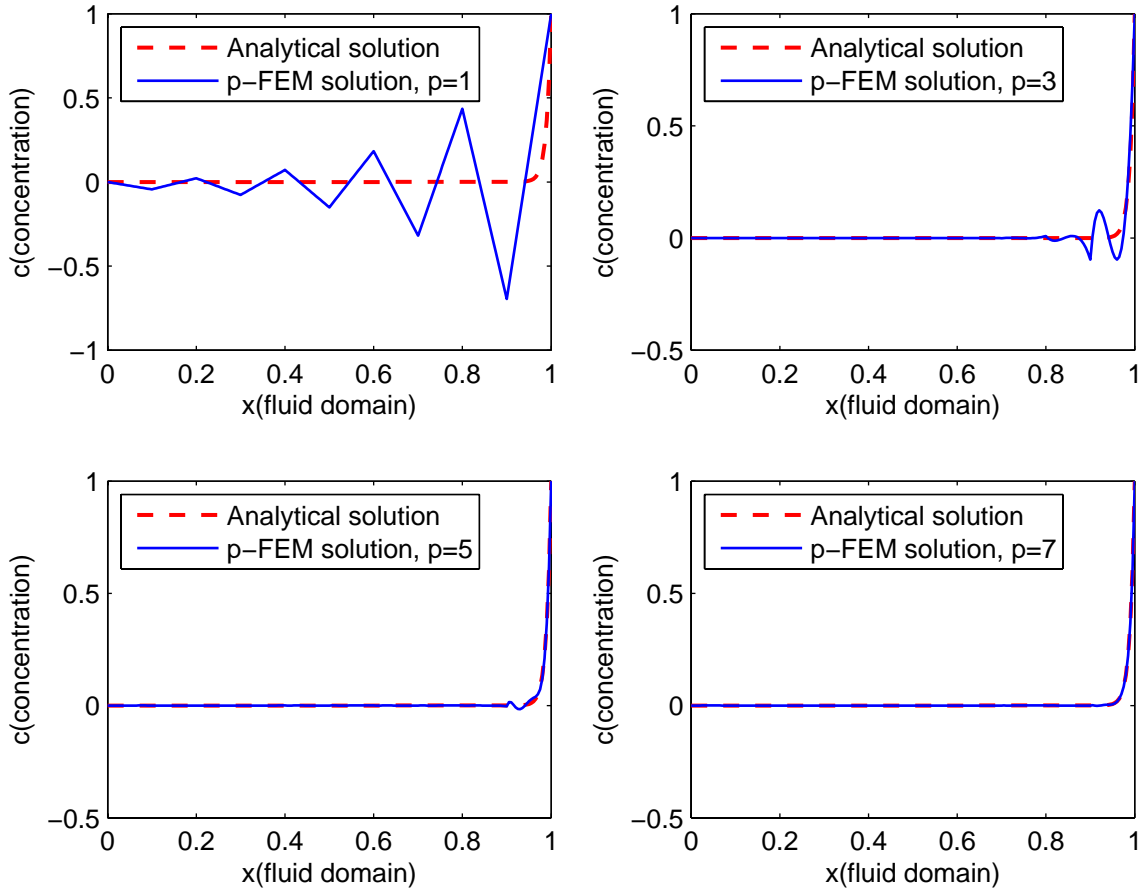


Figure 3.6: Numerical solution with different polynomial degrees, $Pe = 5$

where

$$\begin{cases} \phi(\rho) = \begin{cases} 1 - \rho^2 & \text{if } \rho \leq 1 \\ 0 & \text{else} \end{cases} \\ \rho = \sqrt{x^2 + y^2}. \end{cases} \quad (3.25)$$

For the following computations, the coefficients are defined as $\sigma = 2$, $\nu = 0.0001$ and the source term is

$$f = \begin{cases} 1 & \text{if } \rho \leq 1/2 \\ 0 & \text{otherwise.} \end{cases} \quad (3.26)$$

This example is also discussed in [15]. The result has an interior layer along the circle $\rho = 1/2$. In this instance, a uniform mesh with 10×10 elements is applied and the numerical solution

based on different polynomial degrees of shape functions can be seen in Figure 3.7.

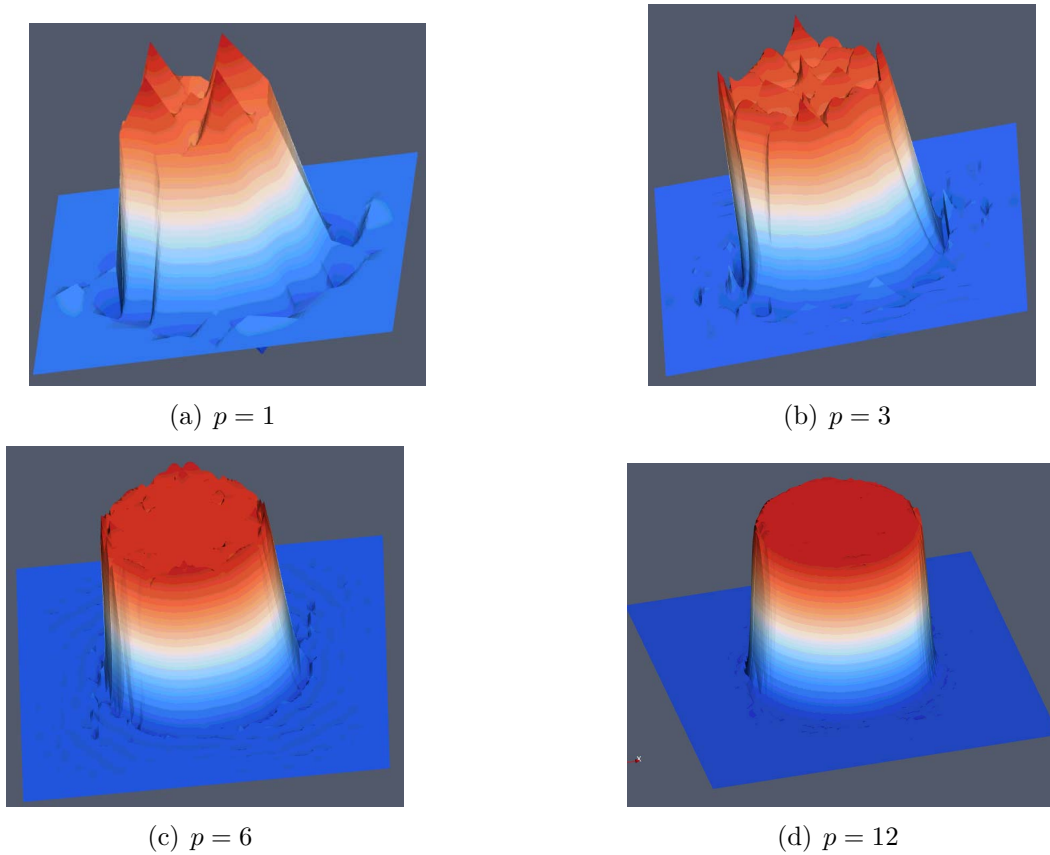


Figure 3.7: The numerical solutions with different polynomial degrees using 10×10 elements

The numerical result displays a strong oscillation along the boundary layer with the application of low order elements. This numerical oscillation can be dramatically reduced or even suppressed by increasing the polynomial degree, as shown in Figure 3.7. The p -FEM with the standard Bubnov-Galerkin method is therefore capable of resolving the solution with a boundary layer.

3.3.2 Multi-component reactive transport problems

As shown in Chapter 2, a one-dimensional multi-component reactive transport problem can be described by Equation 2.21, where the governing equations are coupled by first-order reaction terms. In a multi-dimensional problem, the generalized governing equation for an N -component reactive transport problem with constant velocity \vec{a} and diffusion coefficient ν is

$$R_i \frac{\partial c_i}{\partial t} + \vec{a} \cdot \nabla c_i - \nu \nabla^2 c_i = \sum_{j=1}^N s_{ij} c_j, \quad i = 1, 2, \dots, N, \quad (3.27)$$

where s_{ij} are the coefficients for the reaction terms. Let us assume that homogeneous Dirichlet conditions are applied to the boundary $\partial\Omega$. Applying the backward-difference scheme for time

discretization in Equation 3.28, the corresponding weak form for the i -th component c_i is obtained in Equation 3.29.

$$\frac{\partial c_i^{t+\Delta t}}{\partial t} = \frac{c_i^{t+\Delta t} - c_i^t}{\Delta t} \quad \text{at time } t + \Delta t \quad (3.28)$$

$$\begin{aligned} \frac{\mathcal{M}_i^{t+\Delta t}}{\Delta t} + \mathcal{C}_i^{t+\Delta t} - \mathcal{D}_i^{t+\Delta t} &= \mathcal{F}_i^{t+\Delta t} + \frac{\mathcal{M}_i^t}{\Delta t}, \quad i = 1, 2, \dots, N \quad \text{on } \Omega \\ \mathcal{M}_i^t &= \mathcal{M}(c_i^t) = \int_{\Omega} R_i w_i c_i^t d\Omega \quad \text{at time } t \\ \mathcal{C}_i^t &= \mathcal{C}(c_i^t) = \int_{\Omega} w_i (\vec{a} \cdot \nabla c_i^t) d\Omega \quad \text{at time } t \\ \mathcal{D}_i^t &= \mathcal{D}(c_i^t) = \int_{\Omega} \nabla w_i \cdot (\nu c_i^t) d\Omega \quad \text{at time } t \\ \mathcal{F}_i^t &= \mathcal{F}(c_i^t) = \int_{\Omega} w_i \left(\sum_{j=1}^N s_{ij} c_j^t \right) d\Omega \quad \text{at time } t \end{aligned} \quad (3.29)$$

Here Δt denotes the time step in the backward-difference scheme. They are discretized by applying the Bubnov-Galerkin method and then constructed by assembling the element contributions shown in Equation 3.30.

$$\begin{aligned} \mathbf{M}_i &= \mathbf{A}_{e=1}^{nel} \mathbf{M}_i^e, & M_{i,lk}^e &= \int_{\Omega^e} N_l \cdot (R_i N_k) d\Omega \\ \mathbf{C}_i &= \mathbf{A}_{e=1}^{nel} \mathbf{C}_i^e, & C_{i,lk}^e &= \int_{\Omega^e} N_l \vec{a} \cdot \nabla N_k d\Omega \\ \mathbf{D}_i &= \mathbf{A}_{e=1}^{nel} \mathbf{D}_i^e, & D_{i,lk}^e &= \int_{\Omega^e} \nabla N_l \nu \cdot \nabla N_k d\Omega \\ \mathbf{F}_i &= \mathbf{A}_{e=1}^{nel} \mathbf{F}_i^e, & F_{i,l}^e &= \int_{\Omega^e} N_l d\Omega \end{aligned} \quad (3.30)$$

After introducing shape functions to approximate the unknown function, the weak form at time $t + \Delta t$ reads

$$\left(\frac{\mathbf{M}_i}{\Delta t} + \mathbf{C}_i + \mathbf{D}_i \right) \mathbf{c}_i^{t+\Delta t} = \mathbf{F}_i \left(\sum_{j=1}^N s_{ij} \mathbf{c}_j^{t+\Delta t} \right) + \frac{\mathbf{M}_i}{\Delta t} \mathbf{c}_i^t, \quad i = 1, 2, \dots, N \quad \text{on } \Omega, \quad (3.31)$$

where \mathbf{c}_i^t is the solution vector of the component c_i at the time step t whereas \mathbf{M}_i , \mathbf{C}_i , \mathbf{D}_i and \mathbf{F}_i correspond to mass matrix, convection matrix, diffusion matrix and force vector of the component c_i , respectively.

3.3.2.1 Fixed point iteration for coupled reaction terms

We wish to mention that, in Equation 3.29, the coupled reaction term is treated as a source term which depends on the unknown function c_i . This coupling term can be solved by fixed point iteration. A fixed point for a scalar function is a number whose value remains unchanged when the function is applied [8]. The number p is a fixed point when $g(p) = p$ for a given function g . For a root-finding problem $f(x)=0$, we can find a function g , such that

$$f(x) = x - g(x). \quad (3.32)$$

It is easy to see that if p is a fixed point of the function g , then p is the solution to the equation $f(x) = 0$. In the fixed point iteration, we take a value x_0 to express an initial guess at the solution and the function $g(x)$ maps x_0 to the next point x_1 . The iterative scheme

$$x_{n+1} = g(x_n), \quad n = 0, 1, \dots, n_{max} \quad (3.33)$$

is repeated until the required precision is achieved. Applying the fixed point iteration, the solutions achieve convergence when the difference between the current solution and the previous one is smaller than the given tolerance ϵ_0 . As with scalar functions, it is possible to define fixed point iterations to vector valued functions. Applying the fixed point iteration instead of Equation 3.29 in the numerical analysis solves the following equation system

$$\left(\frac{\mathbf{M}_i}{\Delta t} + \mathbf{C}_i + \mathbf{D}_i\right)\mathbf{c}_i^{t+\Delta t} = \mathbf{F}_i\left(\sum_{j=1}^N s_{ij}\mathbf{c}_j^t\right) + \frac{\mathbf{M}_i}{\Delta t}\mathbf{c}_i^t, \quad i = 1, 2, \dots, N \quad \text{on } \Omega. \quad (3.34)$$

In other words, the value

$$\mathbf{c}_i^{t+\Delta t} = \left(\frac{\mathbf{M}_i}{\Delta t} + \mathbf{C}_i + \mathbf{D}_i\right)^{-1} \left(\mathbf{F}_i\left(\sum_{j=1}^N s_{ij}\mathbf{c}_j^t\right) + \frac{\mathbf{M}_i}{\Delta t}\mathbf{c}_i^t\right), \quad i = 1, 2, \dots, N \quad \text{on } \Omega \quad (3.35)$$

will be computed iteratively. The initial value in this iteration is set to be $\mathbf{c}_i^{t_0} = \mathbf{0}$ over the domain. Basically, the solution from the last iteration step is substituted in the reaction term of the current step to obtain an updated solution. This iteration process is repeated at each time step until the solutions converge, as shown in Equation 3.36, or the iteration comes to an end.

$$\epsilon = \frac{\left\|\mathbf{c}_{i,k}^t - \mathbf{c}_{i,k-1}^t\right\|_{L_2}}{\left\|\mathbf{c}_{i,k-1}^t\right\|_{L_2}} < \epsilon_0, \quad i = 1, 2, \dots, N \quad \text{at time } t \text{ and } k\text{-th fixed point iteration step} \quad (3.36)$$

Once the solution finally fulfills the condition in Equation 3.36, this solution is taken to be a final solution. The flow chart of the computational process is depicted in Figure 3.8. In this figure, $\mathbf{c}_{i,k}^t$ indicates the concentration of the component c_i computed in the k^{th} iteration step of the fixed point method at time t .

3.3.2.2 Three-component transient reactive transport problem in 1D

Here, the one-dimensional example introduced in Chapter 2 is further investigated using p -FEM. The governing equation is the same as Equation 2.21 and corresponding parameters and their values are listed in Table 3.1.

Domain length	L	5	L
Element size	Δx	1	L
Diffusion coefficient	ν	0.001	L^2T^{-1}
Velocity	a	0.01	LT^{-1}
Sorption coefficient	K_d	1.0	-
Reaction coefficient 1	k_1	0.05	T^{-1}
Reaction coefficient 2	k_2	0.03	T^{-1}
Reaction coefficient 3	k_3	0.02	T^{-1}

Table 3.1: Parameter values in the 1D three-components reactive transport problem

The mesh *Péclet* number has the value $Pe = 5$, which indicates the transport is convection flux dominated. Figure 3.9 illustrates the oscillatory solution obtained by linear FEM. Increasing the polynomial degree p to 3 effectively eliminates oscillation in Figure 3.10 and when $p = 5$, the numerical solution matches the analytical one perfectly, see Figure 3.11.

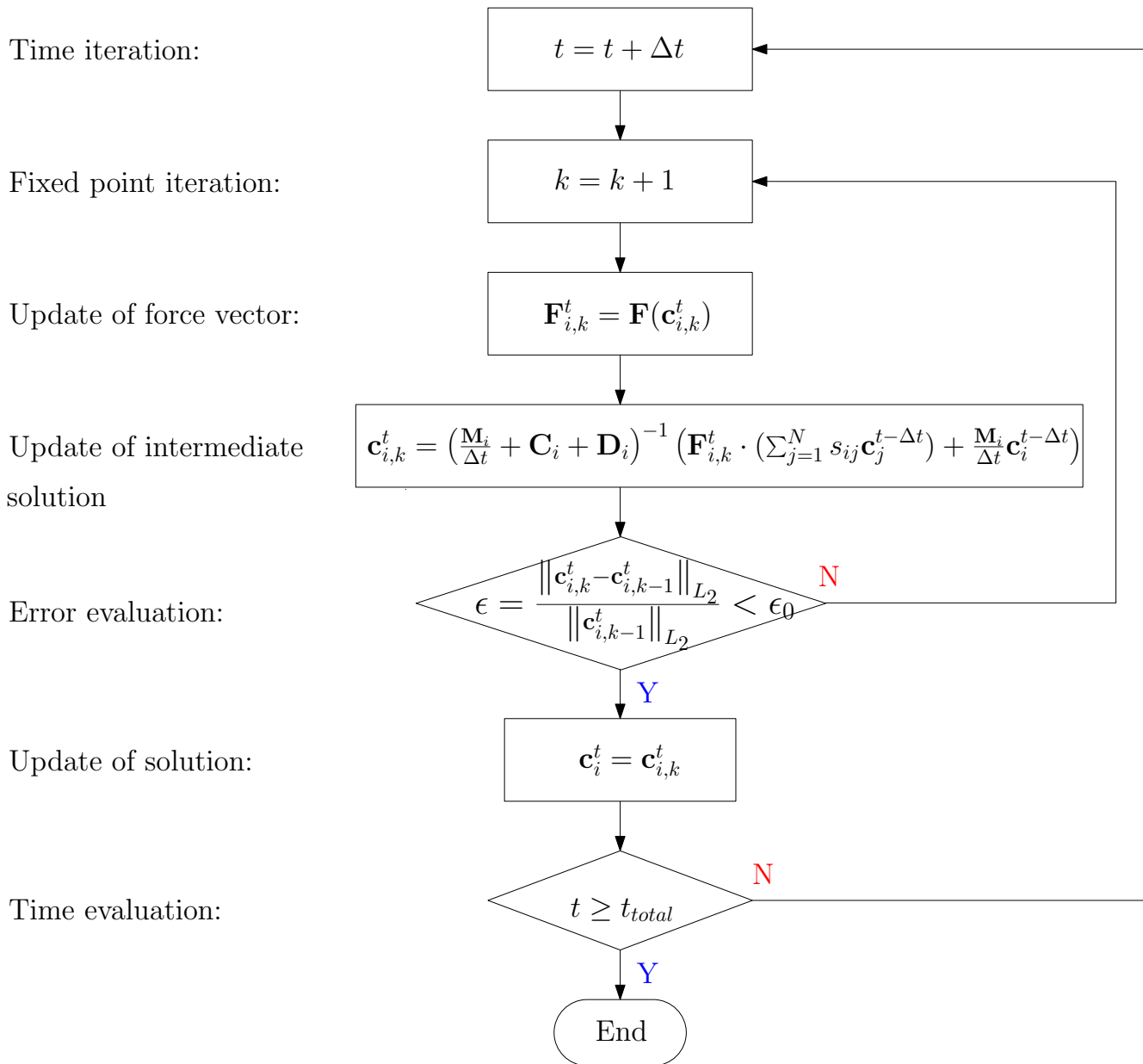
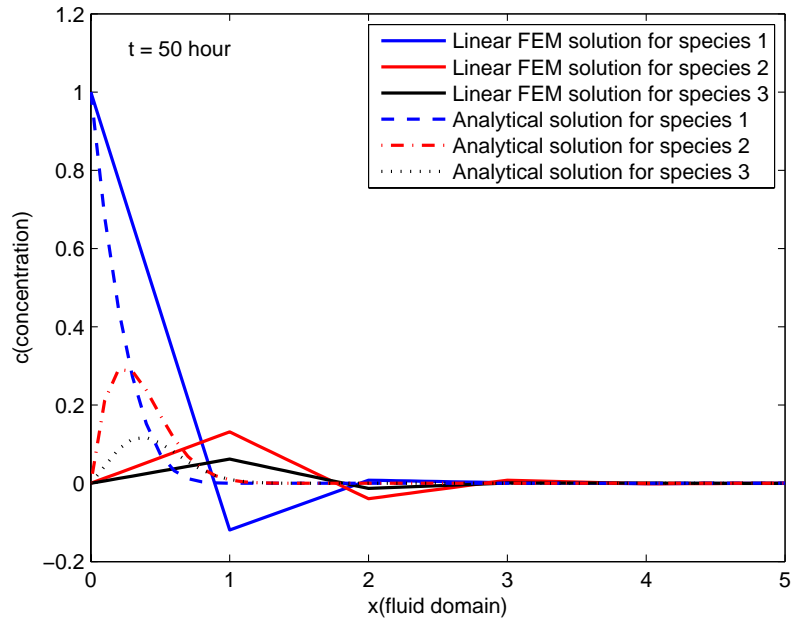
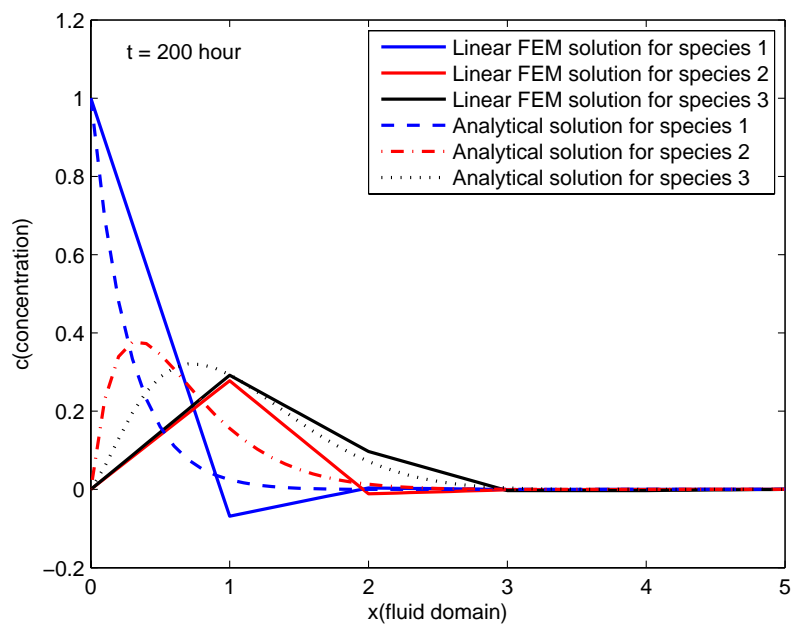


Figure 3.8: Flow chart of multi-component reactive transport problems in computational process

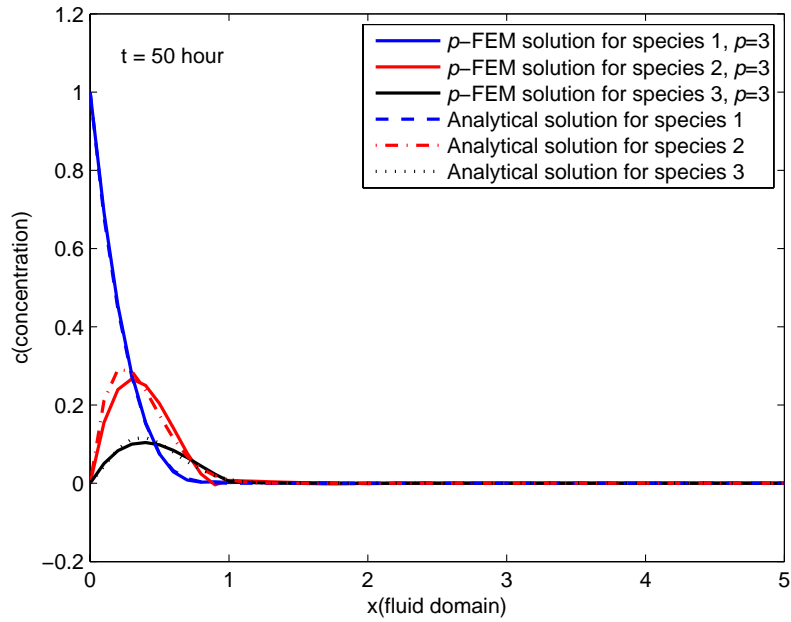


(a)

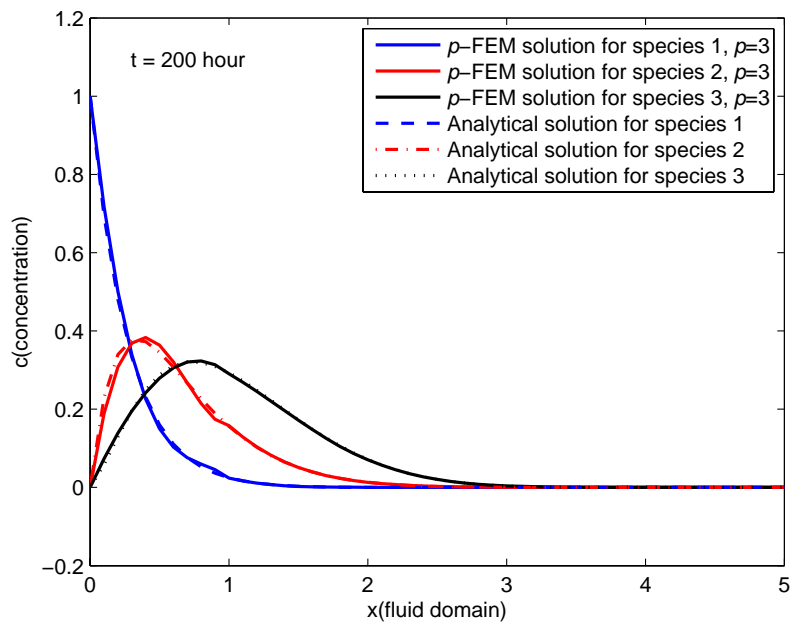


(b)

Figure 3.9: FEM solution for concentration profiles of three components, $Pe = 5$, $p = 1$

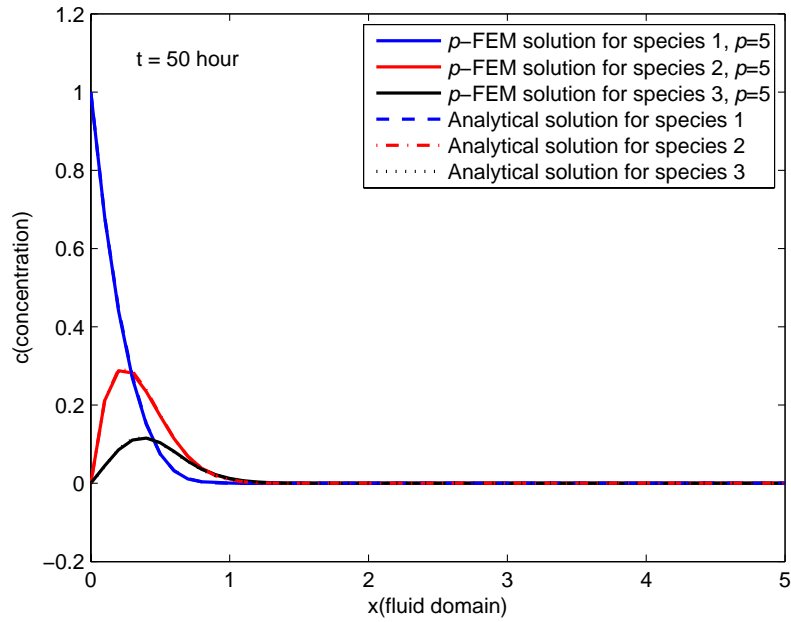


(a)

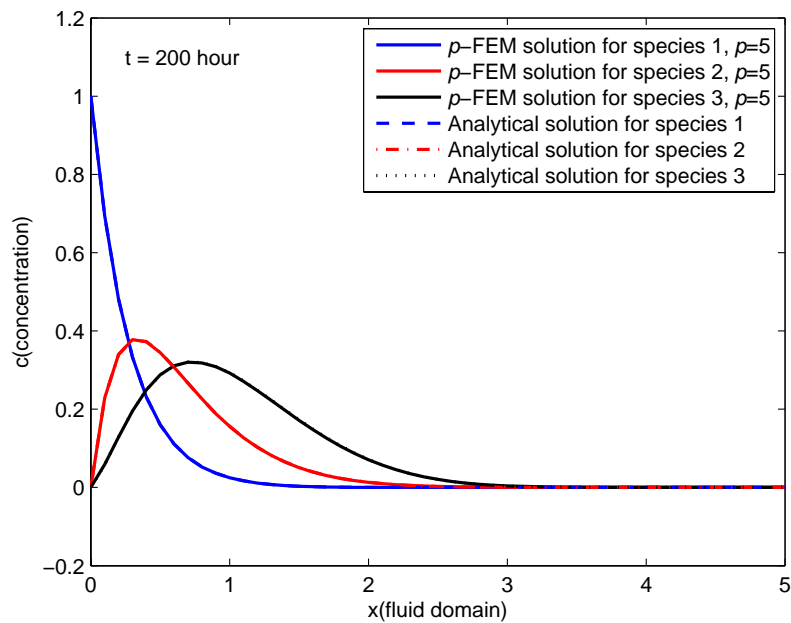


(b)

Figure 3.10: FEM solution for concentration profiles of three components, $Pe = 5$, $p = 3$



(a)



(b)

Figure 3.11: FEM solution for concentration profiles of three components, $Pe = 5$, $p = 5$

Chapter 4

Stability analysis of p -FEM in convection-dominated problems

This chapter is dedicated to the one-dimensional steady convection-diffusion transport problem set out below:

$$\begin{cases} a \frac{dc}{dx} - \nu \frac{d^2c}{dx^2} = f & \text{on } \Omega = \{x | 0 < x < 1\} \\ c = 0 & \text{at } x = 0 \\ c = 0 & \text{at } x = 1. \end{cases} \quad (4.1)$$

Here, the source term f has a constant value of 1 and the corresponding analytical solution reads

$$c(x) = \frac{1}{a} \cdot \left(x - \frac{1 - e^{\frac{ax}{\nu}}}{1 - e^{\frac{a}{\nu}}} \right). \quad (4.2)$$

We discuss the discretization on an equidistant mesh with the size h . It is a well-known fact that the numerical solution of Equation 4.1 is stable for the problem with piecewise linear elements if Pe is not greater than 1 [15]. The straightforward application of the Bubnov-Galerkin discretization leads to the corresponding weak form of Equation 4.1

Given $f : \Omega \rightarrow \mathbb{R}$, find $c \in \mathcal{S}$, such that for all $w \in \mathcal{V}$:

$$\begin{cases} \int_{\Omega} ac'w + c'\nu w'd\Omega = \int_{\Omega} f w d\Omega & \text{on } \Omega \\ c = c_D & \text{on } \Gamma_D \\ \vec{n} \cdot \nu \nabla c = c_N & \text{on } \Gamma_N. \end{cases} \quad (4.3)$$

The scalar function c and w are both discretized and approximated by the same shape functions N_i , which leads to Equation 4.4 featuring the convection matrix \mathbf{C} , diffusion matrix \mathbf{D} and

force vector \mathbf{f} .

$$(\mathbf{C} + \mathbf{D})\vec{c} = \mathbf{f} \quad (4.4)$$

When n denotes the number of equations of the system, \mathbf{C} and \mathbf{D} are $n \times n$ matrices, obtained by assembling element convection matrix C^e and element diffusion matrix D^e , respectively. In the one-dimensional example described in Equation 4.1, C^e , D^e and f^e correspond to:

$$\begin{aligned} C_{ij}^e &= \int_{\Omega^e} a N_i N_{j,x} dx \\ D_{ij}^e &= \int_{\Omega^e} \nu N_{i,x} N_{j,x} dx \\ f_i^e &= \int_{\Omega^e} f N_i dx. \end{aligned} \quad (4.5)$$

Whilst the Bubnov-Galerkin discretization is known to be optimal in the finite element analysis for elliptic problems, when the convection flux becomes more and more dominant, i.e. as Pe grows, the solution obtained by means of the Bubnov-Galerkin method is less and less accurate for a fixed polynomial degree. The next section explains the effect of Pe on the accuracy of the nodal solution.

4.1 Truncation error of the Bubnov-Galerkin discretization in the h -FEM

We consider the problem stated in Equation 4.1 with two adjacent elements $[x_{j-1}, x_j]$ and $[x_j, x_{j+1}]$ as depicted in Figure 4.1, where a node x_j is shared by two elements.

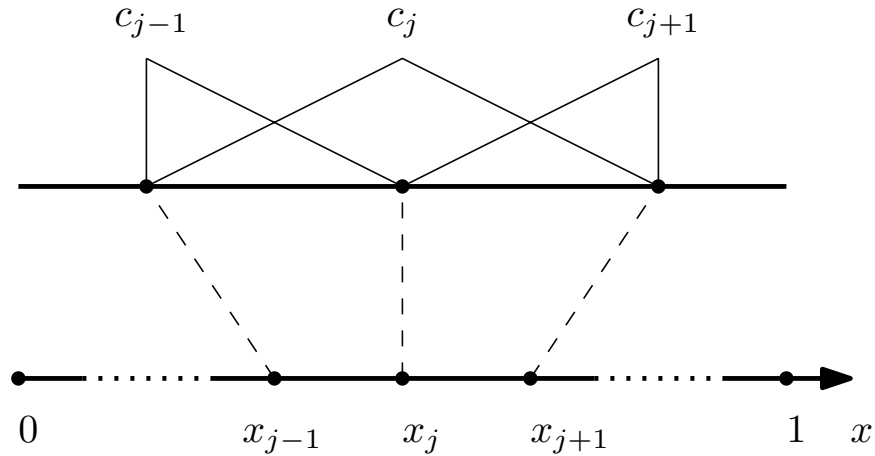


Figure 4.1: 1D example with $p=1$: three degrees of freedom in two elements

For the sake of simplicity, we apply the source term $f = 1$ and discretize the geometry using a uniform mesh with the element length h . The shape functions of a linear element are given

by [59].

$$N_1(\xi) = \frac{1 - \xi}{2} \quad (4.6)$$

$$N_2(\xi) = \frac{1 + \xi}{2} \quad (4.7)$$

where ξ is the normalized local coordinate. Setting $\Omega_j^e = [x_j, x_{j+1}] = [-1, 1]$ and applying the transformation between local and global coordinates, we obtain the following convective and diffusive matrices as well as the force vector [15] for each element, h being the length of the element.

$$C^e = a \int_{\Omega^e} \begin{pmatrix} N_1 \frac{\partial N_1}{\partial x} & N_1 \frac{\partial N_2}{\partial x} \\ N_2 \frac{\partial N_1}{\partial x} & N_2 \frac{\partial N_2}{\partial x} \end{pmatrix} dx = \frac{a}{2} \begin{pmatrix} -1 & +1 \\ -1 & +1 \end{pmatrix} \quad (4.8)$$

$$D^e = \nu \int_{\Omega^e} \begin{pmatrix} \frac{\partial N_1}{\partial x} \frac{\partial N_1}{\partial x} & \frac{\partial N_1}{\partial x} \frac{\partial N_2}{\partial x} \\ \frac{\partial N_2}{\partial x} \frac{\partial N_1}{\partial x} & \frac{\partial N_2}{\partial x} \frac{\partial N_2}{\partial x} \end{pmatrix} dx = \frac{\nu}{h} \begin{pmatrix} +1 & -1 \\ -1 & +1 \end{pmatrix} \quad (4.9)$$

$$f^e = \int_{\Omega^e} \begin{pmatrix} N_1 \\ N_2 \end{pmatrix} dx = \frac{h}{2} \begin{pmatrix} +1 \\ +1 \end{pmatrix} \quad (4.10)$$

Assembling the global system matrix, we obtain

$$\left\{ \begin{pmatrix} -\frac{a}{2} + \dots & \frac{a}{2} & \dots \\ -\frac{a}{2} & \frac{a}{2} - \frac{a}{2} & \frac{a}{2} \\ \dots & -\frac{a}{2} & \frac{a}{2} + \dots \end{pmatrix} + \begin{pmatrix} \frac{\nu}{h} + \dots & -\frac{\nu}{h} & \dots \\ -\frac{\nu}{h} & \frac{\nu}{h} + \frac{\nu}{h} & -\frac{\nu}{h} \\ \dots & -\frac{\nu}{h} & \frac{\nu}{h} + \dots \end{pmatrix} \right\} \begin{pmatrix} c_{j-1} \\ c_j \\ c_{j+1} \end{pmatrix} = \begin{pmatrix} \frac{h}{2} + \dots \\ \frac{h}{2} + \frac{h}{2} \\ \frac{h}{2} + \dots \end{pmatrix}. \quad (4.11)$$

The j th row of the matrix is related to the coupled degrees of freedom x_j and reads

$$a \left(\frac{c_{j+1} - c_{j-1}}{2h} \right) - \nu \left(\frac{c_{j+1} - 2c_j + c_{j-1}}{h^2} \right) = 1. \quad (4.12)$$

We now follow the analytical process introduced in [15], where the truncation error of a Bubnov-Galerkin discretization of Equation 4.1 is quantified in order to specify the additional

diffusion term used in Petrov-Galerkin methods. The exact solution of Equation 4.1 with $f = 1$ is

$$c(x) = \frac{1}{a} \cdot \left(x - \frac{1 - e^{\frac{ax}{\nu}}}{1 - e^{\frac{a}{\nu}}} \right). \quad (4.13)$$

Ideally, the value at each node should accordingly fulfill the exact solution

$$c_j = c(x_j) = \frac{1}{a} \cdot \left(x_j - \frac{1 - e^{\frac{ax_j}{\nu}}}{1 - e^{\frac{a}{\nu}}} \right). \quad (4.14)$$

In a uniform mesh with an element length of h , the coordinates of three consecutive nodes have the relationship

$$x_{j-1} + h = x_j = x_{j+1} - h. \quad (4.15)$$

Imposing the exact value on each node as in Equation 4.14 leads to the following system of equations

$$\begin{cases} c_{j-1} = \frac{1}{a} \left((x_j - h) - \frac{1 - e^{\frac{a(x_j-h)}{\nu}}}{1 - e^{\frac{a}{\nu}}} \right) \\ c_j = \frac{1}{a} \left(x_j - \frac{1 - e^{\frac{ax_j}{\nu}}}{1 - e^{\frac{a}{\nu}}} \right) \\ c_{j+1} = \frac{1}{a} \left((x_j + h) - \frac{1 - e^{\frac{a(x_j+h)}{\nu}}}{1 - e^{\frac{a}{\nu}}} \right). \end{cases} \quad (4.16)$$

To facilitate a comparison with the discrete equation resulting from the straightforward linear discretization given in Equation 4.12, we set three coefficients α_1 , α_2 , α_3 , such that the equation

$$\alpha_1 c_{j-1} + \alpha_2 c_j + \alpha_3 c_{j+1} = 1. \quad (4.17)$$

is valid for all nodes, all *Péclet* numbers and any length h . Inserting the nodal expressions from Equation 4.16 into Equation 4.17, we obtain the following conditions:

$$\begin{cases} \alpha_1 + \alpha_2 + \alpha_3 = 0 \\ -\alpha_1 + \alpha_3 = \frac{a}{h} \\ \alpha_1 e^{-2Pe} + \alpha_2 + \alpha_3 e^{2Pe} = 0 \end{cases} \quad (4.18)$$

Having solved α_1 , α_2 , α_3 and replaced the values in Equation 4.17, we derive Equation 4.19, which has a similar form to Equation 4.12

$$a \left(\frac{c_{j+1} - c_{j-1}}{2h} \right) - (\nu + \bar{\nu}) \left(\frac{c_{j+1} - 2c_j + c_{j-1}}{h^2} \right) = 1, \quad (4.19)$$

where $\bar{\nu}$ is an additional term that does not appear in Equation 4.12. This extra term can be interpreted either as the truncation error of the first order Bubnov-Galerkin method or as an additional diffusivity required to provide nodally exact results. This term is a function of the *Péclet* number and reads

$$\bar{\nu} = \left(\coth Pe - \frac{1}{Pe} \right) \nu Pe. \quad (4.20)$$

Its value increases with the *Péclet* number. In fact, Equation 4.20 forms the basic motivation behind using the Petrov-Galerkin method. In many stabilization approaches, efforts are made to control the artificial numerical oscillations in convection-dominated problems by compensating for the truncation error by adding extra diffusivity. As shown in the next section, however, the truncation error of the Bubnov-Galerkin method decreases as the polynomial order of the spatial discretization increases.

4.2 Truncation error of the Bubnov-Galerkin discretization in the p -FEM

In this section, we contemplate the same example as presented in Section 4.1, where we apply hierarchic shape functions of second order derived from the set of integrated Legendre polynomials and investigate the polynomial orders up to 5. The convection and stiffness matrices are then computed analogously to the low order finite element method, as follows

$$C^e = a \int_{\Omega^e} \begin{pmatrix} N_1 \frac{\partial N_1}{\partial x} & N_1 \frac{\partial N_2}{\partial x} & N_1 \frac{\partial N_3}{\partial x} \\ N_2 \frac{\partial N_1}{\partial x} & N_2 \frac{\partial N_2}{\partial x} & N_2 \frac{\partial N_3}{\partial x} \\ N_3 \frac{\partial N_1}{\partial x} & N_3 \frac{\partial N_2}{\partial x} & N_3 \frac{\partial N_3}{\partial x} \end{pmatrix} dx = \frac{a}{2} \begin{pmatrix} -1 & +1 & -\frac{\sqrt{6}}{3} \\ -1 & +1 & \frac{\sqrt{6}}{3} \\ \frac{\sqrt{6}}{3} & -\frac{\sqrt{6}}{3} & 0 \end{pmatrix} \quad (4.21)$$

$$K^e = \nu \int_{\Omega^e} \begin{pmatrix} \frac{\partial N_1}{\partial x} \frac{\partial N_1}{\partial x} & \frac{\partial N_1}{\partial x} \frac{\partial N_2}{\partial x} & \frac{\partial N_1}{\partial x} \frac{\partial N_3}{\partial x} \\ \frac{\partial N_2}{\partial x} \frac{\partial N_1}{\partial x} & \frac{\partial N_2}{\partial x} \frac{\partial N_2}{\partial x} & \frac{\partial N_2}{\partial x} \frac{\partial N_3}{\partial x} \\ \frac{\partial N_3}{\partial x} \frac{\partial N_1}{\partial x} & \frac{\partial N_3}{\partial x} \frac{\partial N_2}{\partial x} & \frac{\partial N_3}{\partial x} \frac{\partial N_3}{\partial x} \end{pmatrix} dx = \frac{\nu}{h} \begin{pmatrix} +1 & -1 & 0 \\ -1 & +1 & 0 \\ 0 & 0 & +2 \end{pmatrix} \quad (4.22)$$

$$f^e = \int_{\Omega^e} \begin{pmatrix} N_1 \\ N_2 \\ N_3 \end{pmatrix} dx = \frac{h}{2} \begin{pmatrix} +1 \\ +1 \\ -\frac{\sqrt{6}}{3} \end{pmatrix}. \quad (4.23)$$

The total number of degrees of freedom in two elements is five and consists of three nodal modes and two internal modes, see Figure 4.2.

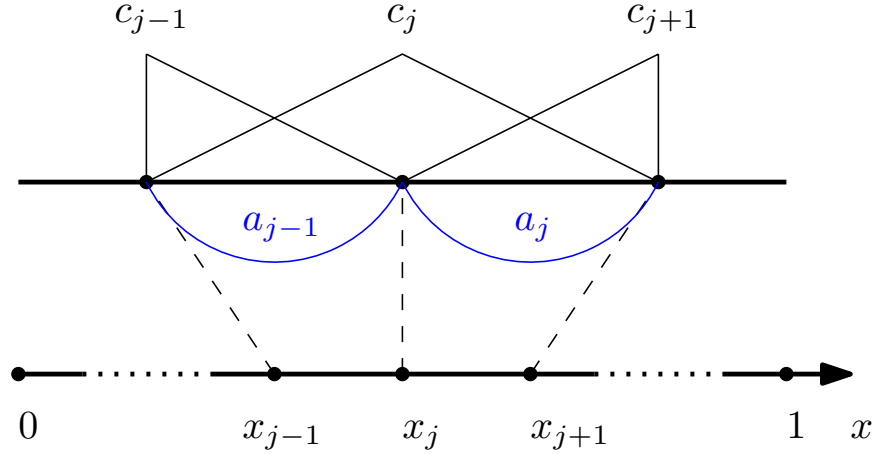


Figure 4.2: 1D example with $p=2$: five degrees of freedom in two elements

We wish to mention that the elements are only coupled by the linear modes. All higher order modes are purely local to the element and thus independent of other degrees of freedom. One block of the global matrix, which corresponds to five degrees of freedom depicted in Figure 4.2, is shown in Equation 4.24.

$$\begin{array}{c}
 c_{j-1} \\
 c_j \\
 c_{j+1} \\
 a_{j-1} \\
 a_j
 \end{array}
 \begin{pmatrix}
 c_{j-1} & c_j & c_{j+1} & a_{j-1} & a_j \\
 \frac{\nu}{h} - \frac{a}{2} + \dots & -\frac{\nu}{h} + \frac{a}{2} + \dots & & -\frac{\sqrt{6}}{6}a & \\
 -\frac{\nu}{h} - \frac{a}{2} & \frac{2\nu}{h} & -\frac{\nu}{h} + \frac{a}{2} & \frac{\sqrt{6}}{6}a & -\frac{\sqrt{6}}{6}a \\
 & -\frac{\nu}{h} - \frac{a}{2} + \dots & \frac{\nu}{h} + \frac{a}{2} + \dots & & \frac{\sqrt{6}}{6}a \\
 \frac{\sqrt{6}}{6}a & -\frac{\sqrt{6}}{6}a & & \frac{2\nu}{h} & \\
 & \frac{\sqrt{6}}{6}a & -\frac{\sqrt{6}}{6}a & & \frac{2\nu}{h}
 \end{pmatrix}
 \begin{pmatrix}
 c_{j-1} \\
 c_j \\
 c_{j+1} \\
 a_{j-1} \\
 a_j
 \end{pmatrix}
 =
 \begin{pmatrix}
 \frac{h}{2} + \dots \\
 h \\
 \frac{h}{2} + \dots \\
 -\frac{\sqrt{6}}{6}h \\
 -\frac{\sqrt{6}}{6}h
 \end{pmatrix}
 \quad (4.24)$$

The discrete functions referring to degrees of freedom c_j , a_{j-1} and a_j can be computed independently. There are consequently three equations to solve

$$\left\{ \begin{array}{l}
 \frac{\nu}{h} \cdot (-c_{j-1} + 2c_j - c_{j+1}) + \frac{a}{2} \cdot (-c_{j-1} + \frac{\sqrt{6}}{3}(a_{j-1} - a_j) + c_{j+1}) = h \\
 \frac{\nu}{h} \cdot 2a_{j-1} + \frac{\sqrt{6}}{6}a \cdot (c_{j-1} - c_j) = -\frac{\sqrt{6}}{6}h \\
 \frac{\nu}{h} \cdot 2a_j + \frac{\sqrt{6}}{6}a \cdot (c_j - c_{j+1}) = -\frac{\sqrt{6}}{6}h.
 \end{array} \right. \quad (4.25)$$

a_{j-1} and a_j , the variables related to the internal mode, can be eliminated from the last two equations. After substituting these variables in the first equation of Equation 4.25, we arrive

at the condensed Equation 4.26, which is solely related to nodal degrees of freedom

$$a \left(\frac{c_{j+1} - c_{j-1}}{2h} \right) - (\nu + \bar{\nu}_2) \left(\frac{c_{j+1} - 2c_j + c_{j-1}}{h^2} \right) = 1, \quad (4.26)$$

where

$$\bar{\nu}_2 = \frac{1}{3} Pe^2 \nu. \quad (4.27)$$

$\bar{\nu}_2$ represents the additional numerical diffusion generated naturally by the second order Bubnov-Galerkin method and can be regarded as an approximation of Equation 4.20. Generally speaking, it is possible to condense the system equation in Equation 4.28 in an analogous manner using polynomial degrees higher than 2, all higher modes being purely internal to the element. The form of the resulting equation at node x_j is similar to Equation 4.26

$$a \left(\frac{c_{j+1} - c_{j-1}}{2h} \right) - (\nu + \bar{\nu}_p) \left(\frac{c_{j+1} - 2c_j + c_{j-1}}{h^2} \right) = 1 \quad (4.28)$$

The additional numerical diffusion term $\bar{\nu}_p$ can be computed in the same way. For third, fourth and fifth orders, it reads

$$\begin{aligned} \bar{\nu}_3 &= \frac{5Pe^2\nu}{Pe^2 + 15} \\ \bar{\nu}_4 &= \frac{\nu(Pe^4 + 35Pe^2)}{10Pe^2 + 105} \\ \bar{\nu}_5 &= \frac{14\nu(4Pe^4 + 90Pe^2)}{4Pe^4 + 420Pe^2 + 3780}. \end{aligned} \quad (4.29)$$

In fact, the condensation approach from Equation 4.25 to Equation 4.26 can be interpreted as follows: the contribution of the internal degrees of freedom in p -FEM is transferred to the contribution of nodal degrees of freedom located at the vertices of the element only. The solutions of the condensed system in Equation 4.28, which consists solely of nodal degrees of freedom, are identical to the nodal solutions of the complete system, where the internal modes are also taken into account.

Compared to Equation 4.20, the relative truncation error of p -FEM is defined as

$$\Delta\nu_p = \bar{\nu} - \bar{\nu}_p \quad (4.30)$$

and depicted in dependence of Pe in Figure 4.3, where the ordinate displays $\Delta\nu_p$.

In general, the curves have different tendencies which correspond to the parity of the polynomial degree. Odd degrees generate curves that increase monotonically as Pe increases, while the even ones decrease. Although the sign of relative truncation error depends on the parity

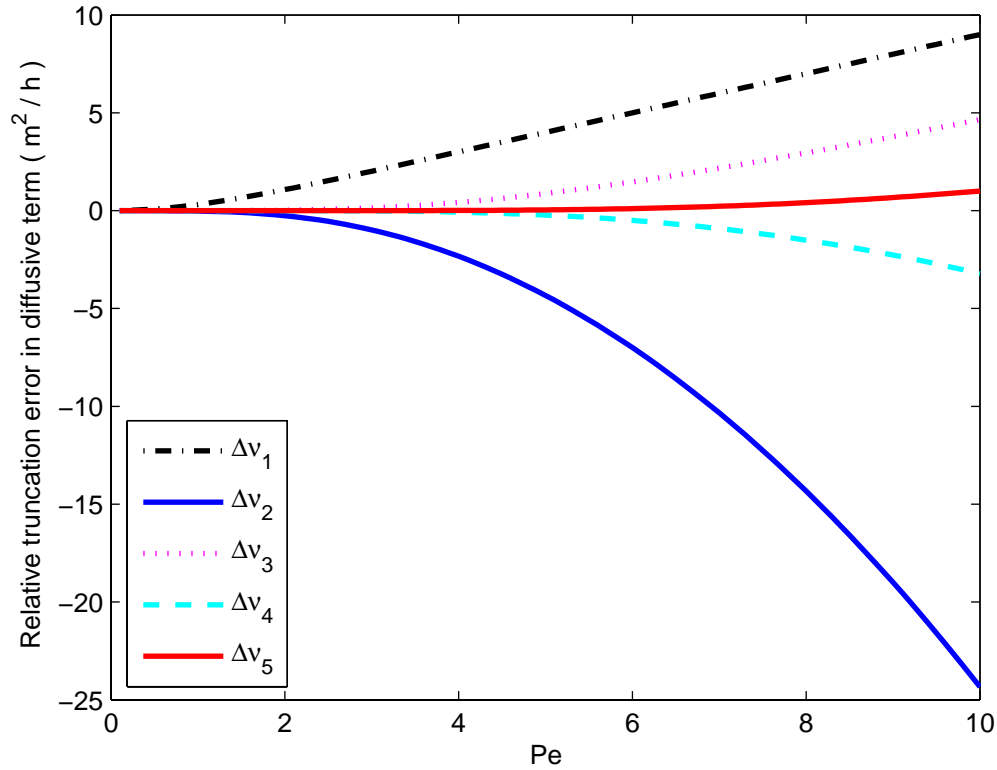


Figure 4.3: Relative truncation error with different polynomial degrees

of the order, the absolute value of relative truncation error decreases with each higher order of shape function. Accordingly, the numerical solution at the nodes comes close to the exact solution.

On the other hand, using odd polynomial degrees, the numerical diffusivity of the high order approach is less than $\bar{\nu}$. This lack of diffusivity explains the oscillatory behavior of the numerical solution with a high Pe . By contrast, the numerical diffusivity is always greater than $\bar{\nu}$ using even polynomial degrees. Consequently, nodal solutions exhibit an over-diffusive behavior and never show nodal oscillations. This result is analyzed from a more detailed, mathematical angle in the next section.

4.3 Connection of the stability and the structure of the system matrix

The stability of the system is determined by the discrete maximum principle which manifests itself in the sign pattern of the off-diagonal terms of the system matrix. This connection was proven for the transient heat equation by Rank [50], where the size of the time step δt must remain above a certain threshold for the discrete maximum principle to be fulfilled, as otherwise the system will become unstable. More recently, this connection was studied at

greater depth in [19], where the form of the system matrix resembles the tridiagonal Toeplitz matrix.

4.3.1 Spectral properties of tridiagonal Toeplitz matrix

By applying the Galerkin discretization to Equation 4.3, we obtain a discrete linear system of equations in the following form

$$\mathcal{A}\vec{c} = \mathbf{f}. \quad (4.31)$$

For example, the system matrix \mathcal{A} corresponds to the sum of a convection and a diffusion matrix in Equation 4.4. [19] proved that, if the system matrix \mathcal{A} is similar in form to Equation 4.32, the solution of the system is stable, i.e. the solution does not oscillate, if and only if α is not larger than 1.

$$\mathcal{A}(\alpha) = \text{tridiag}(-1 - \alpha, 2, -1 + \alpha) \quad (4.32)$$

Applying the linear Bubnov-Galerkin discretization to an evenly-spaced computational grid, it is possible to reformulate Equation 4.12 in such a way that the global stiffness matrix has an analogous tridiagonal structure

$$\mathcal{A} = \frac{\nu}{h^2} \cdot \text{tridiag}(-1 - Pe, 2, -1 + Pe). \quad (4.33)$$

Equation 4.33 is clearly valid in the case with linear elements, since the *Péclet* number corresponds directly to α . Eigenvalues $\{\lambda_j\}_{j=1}^N$ of Equation 4.34 can be computed using the theory of Toeplitz matrices.

$$\lambda_j = 2 \left(1 + \sqrt{|1 - Pe^2|} e^{\frac{i}{2}(\pi + \arg(Pe-1))\cos(j\pi h)} \right) \quad j = 1, 2, \dots, N \quad (4.34)$$

It means that eigenvalues $\{\lambda_j\}_{j=1}^N$ are complex when Pe exceeds 1, whereas for $Pe \leq 1$, they only lie on the real axis. Equation 4.34 can be re-written in the form of

$$\lambda_j = \begin{cases} 2 \left(1 - \sqrt{1 - Pe^2} \cos(j\pi h) \right) & 0 \leq Pe \leq 1 \\ 2 \left(1 + i\sqrt{Pe^2 - 1} \cos(j\pi h) \right) & Pe > 1 \end{cases} \quad j = 1, 2, \dots, N. \quad (4.35)$$

4.4 Stability analysis of nodal solutions in the p -FEM

Similarly, in convection-diffusion problems, the solution stability is also influenced by the sign pattern of the entries in the system matrix. In the p -FEM, additional degrees of freedom are introduced into the matrix when the polynomial degree p is larger than 1, which makes the matrix more complicated than the tridiagonal one. When hierarchic shape functions are

applied, however, the equations of internal degrees of freedom can be condensed out such that the system matrix contains only the equations of nodal degrees of freedom. Equation 4.28 can be reformulated as

$$\left(-\frac{a}{2h} - \frac{(\nu + \bar{\nu}_p)}{h^2}\right) \cdot c_{j-1} + \frac{2(\nu + \bar{\nu}_p)}{h^2} \cdot c_j + \left(\frac{a}{2h} - \frac{(\nu + \bar{\nu}_p)}{h^2}\right) \cdot c_{j+1} = 1. \quad (4.36)$$

We now evaluate the stability solely at the nodal degrees of freedom rather than the internal ones. For the sake of clarity, we abbreviate the common factor $\frac{(\nu + \bar{\nu}_p)}{h^2}$ in Equation 4.36. The condensed system now has the same structure as Equation 4.32, i.e. it is a Toeplitz matrix.

$$\mathcal{A}_p = \frac{(\nu + \bar{\nu}_p)}{h^2} \text{tridiag}(-1 - \alpha_p, 2, -1 + \alpha_p) \quad (4.37)$$

$$\alpha_p = \frac{ah}{2(\nu + \bar{\nu}_p)}$$

The stability of the nodal solutions is consequently determined by the value of α_p . The value of α_p , moreover, can be quantified for higher order polynomial degrees on the basis of Equations 4.27 and 4.29.

$$\begin{aligned} p = 2 & \quad \alpha_2 = \frac{3Pe}{Pe^2 + 3} \\ p = 3 & \quad \alpha_3 = \frac{Pe(Pe^2 + 15)}{2Pe^2 + 5} \\ p = 4 & \quad \alpha_4 = \frac{5Pe(2Pe^2 + 21)}{Pe^4 + 45Pe^2 + 105} \\ p = 5 & \quad \alpha_5 = \frac{Pe(Pe^4 + 105Pe^2 + 945)}{15(Pe^4 + 28Pe^2 + 63)} \\ p = 6 & \quad \alpha_6 = \frac{21Pe(Pe^4 + 60Pe^2 + 495)}{Pe^6 + 210Pe^4 + 4725Pe^2 + 10395} \\ p = 7 & \quad \alpha_7 = \frac{Pe(Pe^6 + 378Pe^4 + 17325Pe^2 + 135135)}{7(4Pe^6 + 450Pe^4 + 8910Pe^2 + 19035)}. \end{aligned} \quad (4.38)$$

The corresponding values are plotted in Figure 4.4. As we can see, α_p increases as Pe for odd polynomial degrees. For even polynomial degrees, α_p first increases and then decreases, while the value is always smaller than 1. This, in turn, means that, the numerical solution at nodal degrees of freedom never oscillates in the case of even polynomial degrees. This result also coincides with the conclusion from the relative truncation error analysis in the previous section. To clarify this point even further, we plot the solution of the 1D example with $Pe = 20$, as shown in Figure 4.5.

Figure 4.5 illustrates that, when the polynomial degree is even, numerical oscillations only stem from internal modes and the numerical solutions at each node do not oscillate. For odd polynomial degrees, numerical oscillations are reflected by both internal and nodal degrees of

freedom.

By setting $\alpha_p = 1$ in Equation 4.38, we can compute the maximum value of Pe allowed, thus guaranteeing nodally stable solutions for the given polynomial degree of the shape functions.

$$\begin{aligned}
 p = 3 & \quad Pe = 2.322185 \\
 p = 5 & \quad Pe = 3.646738 \\
 p = 7 & \quad Pe = 4.971786 \\
 p = 9 & \quad Pe = 6.297019 \\
 p = 11 & \quad Pe = 7.622340 \\
 & \quad \dots
 \end{aligned} \tag{4.39}$$

In other words, for a given *Péclet* number, the corresponding p stated in Equation 4.39 is the minimum polynomial degree required, and their relationship is depicted in Figure 4.6. It turns out to be almost linear for polynomial orders $p \leq 11$.

The value of the *Péclet* number includes the information of the element size h , so Equation 4.39 also indicates the relationship between mesh size h and the polynomial degree p for a given $\frac{a}{\nu}$. The maximum mesh size allowed with respect to the value of $\frac{a}{\nu}$ is plotted in Figure 4.7 for different orders.

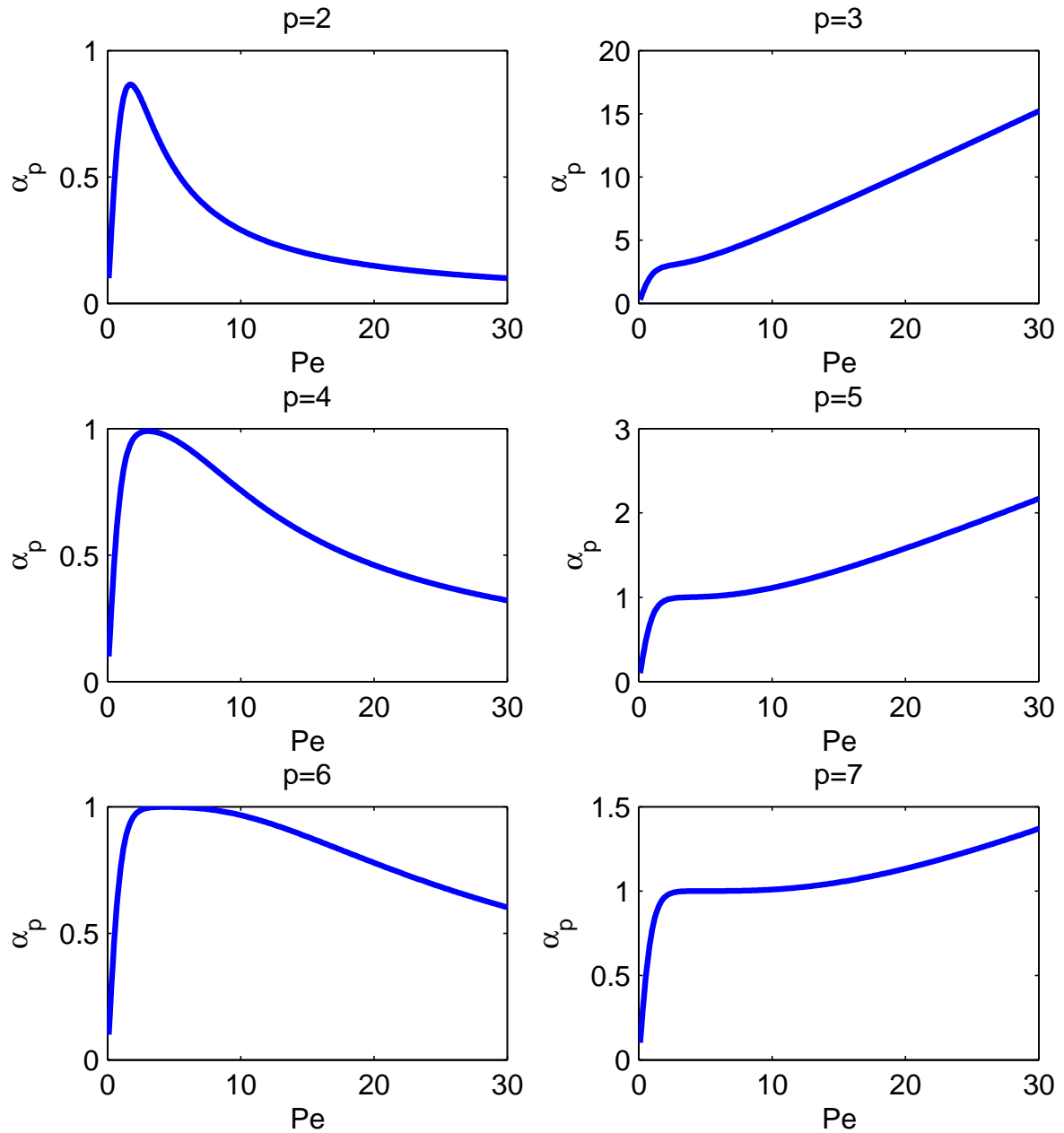


Figure 4.4: α_p behaves differently for odd and even polynomial degrees

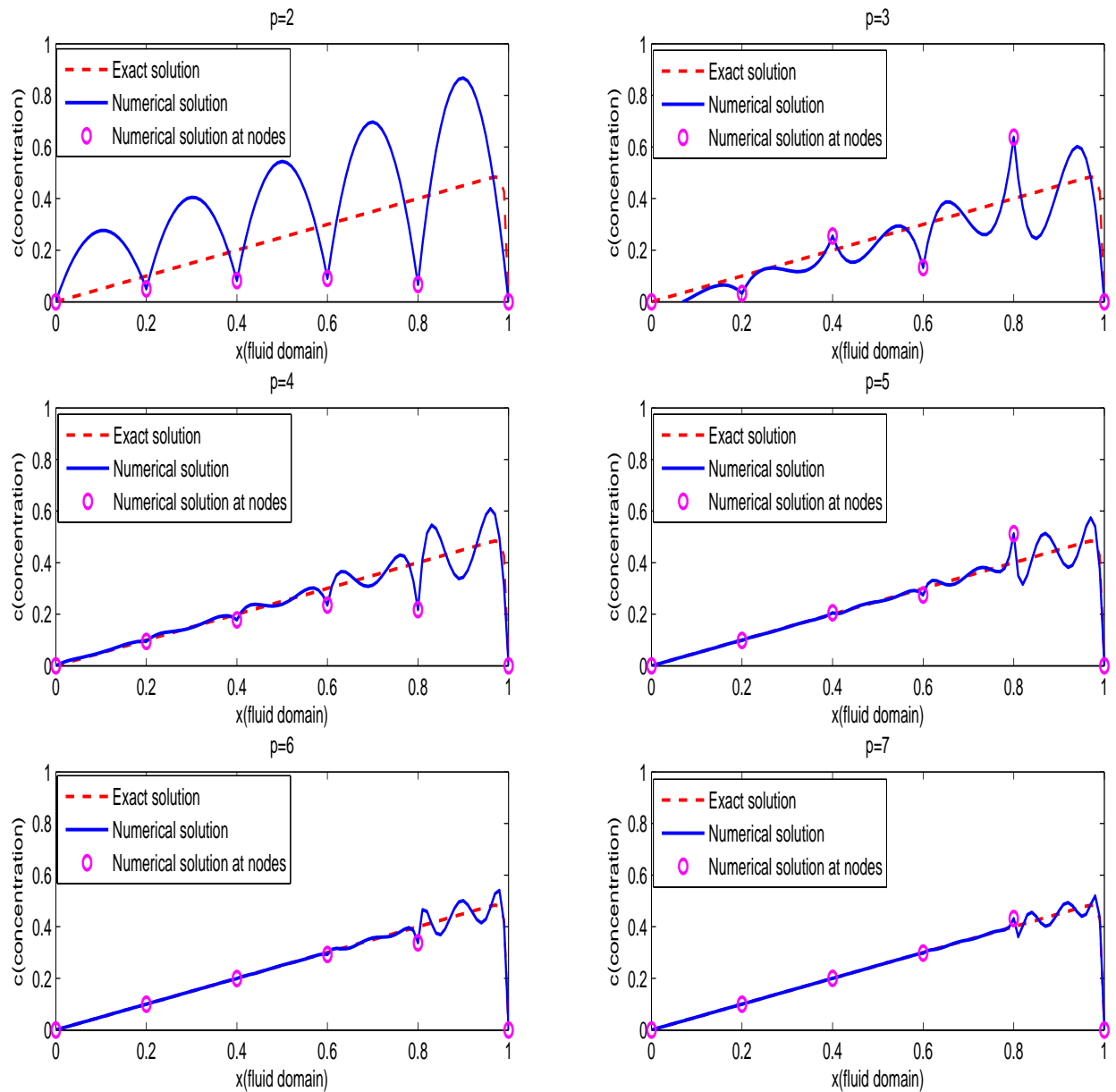


Figure 4.5: Numerical solutions with different Ansatz degree, $Pe=20$

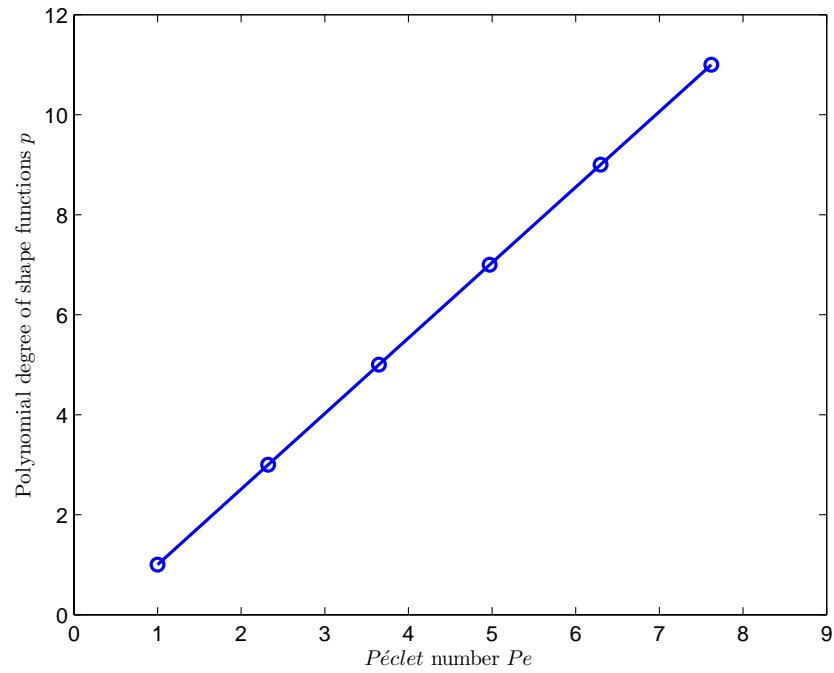


Figure 4.6: The relationship between a given *Péclet* number and the minimum polynomial degree required

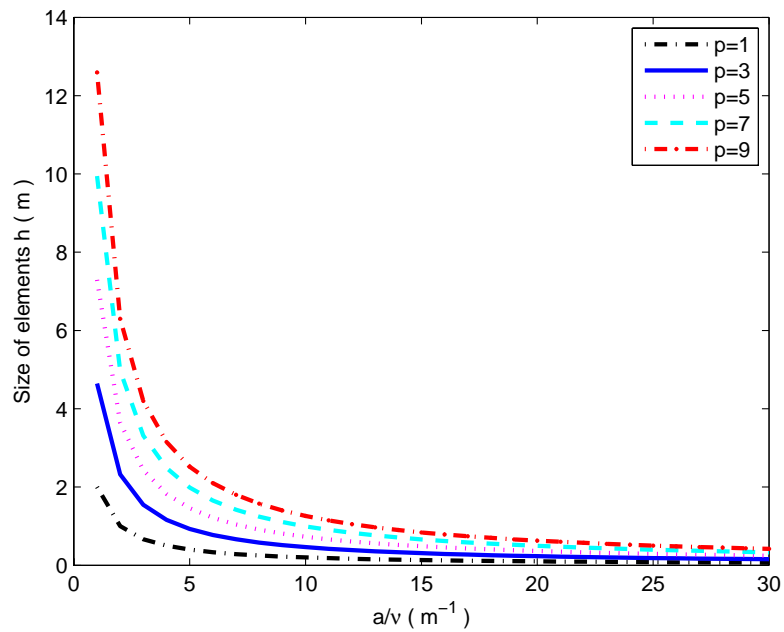


Figure 4.7: The maximum allowed mesh size with respect to a/ν for different polynomial degrees

4.5 Verification of truncation analysis in 1D convection-diffusion problem

In this example, the numerical result of the one-dimensional convection-diffusion transport problem is compared to the exact solution to verify the *Péclet* numbers stated in Equation 4.39. We again consider the 1D convection-diffusion equation

$$\begin{cases} a \frac{dc}{dx} - \nu \frac{d^2c}{dx^2} = 1 & \text{on } \Omega = \{x | 0 < x < 1\} \\ c = 0 & \text{at } x = 0 \\ c = 0 & \text{at } x = 1. \end{cases} \quad (4.40)$$

We choose the parameters $a = 1.2m/h$, $\nu = 0.02m^2/h$, and compute the corresponding numerical solutions with 10 elements of the same length $h = 0.1$. The analytical solution reads

$$y = a \left(x - \frac{e^{ax/\nu} - 1}{e^{a/\nu} - 1} \right). \quad (4.41)$$

Employing linear elements, the Bubnov-Galerkin method produces the expected oscillations, since *Péclet* number $Pe = \frac{ah}{2\nu} = 3$ is greater than 1. Figure 4.8 shows the comparison between the exact solution and the numerical solution for different polynomial degrees.

The oscillations tend to decrease as the polynomial degree increases. Although there is considerable improvement in the numerical oscillations using linear elements with $p = 3$, the nodal solution still oscillates. The solution at node $x = 0.8$ is smaller than the exact solution, whereas that at its neighboring node $x = 0.9$ is larger. In other words, the solution still oscillates around the exact solution. With $p = 5$, the numerical solutions at both nodes are greater than the exact solution, which is a clear indication that the nodal oscillation has now vanished completely. This observation is perfectly compatible with the result obtained mathematically in Equation 4.39.

Figure 4.9 shows the eigenvalues of the full system matrix computed by means of Lagrange shape functions. Since the Lagrange shape functions are nodal-based, the solution obtained by solving the system matrix has a physical interpretation – the solution at each internal or end-node. Therefore, the stability of the solution can also be reflected by analyzing eigenvalues of the full system matrix constructed using the Lagrange shape functions. With $p = 5$, all the eigenvalues lie on the real axis, whereas some eigenvalues are located on the complex axis using $p = 3$. This observation coincides well with the results given Equation 4.35.

With a stabilized solution, it is now possible to enjoy the benefits of the exponential convergence rate of the p -version of finite element method. The numerical error in the finite element

approximation can be quantified by the error in L_2 norm defined by

$$\|e\|_{L_2} = \int_{\Omega} e^2 d\Omega = \int_{\Omega} (c_{ex} - c_{fe})^2 d\Omega. \quad (4.42)$$

Figure 4.10 plots the result with a double logarithmic scale, showing the convergence rate of the error in the L_2 norm by a pure h - and p -extension, respectively. With different values of a/ν , the p -extension exhibits exponential convergence, whereas the h -extension only obtains an algebraic rate of the convergence. In addition, the effect of the a/ν can also be observed in Figure 4.10. If the value a , ν and h satisfy the condition that point $(a/\nu, h)$ is located below a certain curve in Figure 4.10, then the nodal solutions are non-oscillatory for the corresponding polynomial degree p .

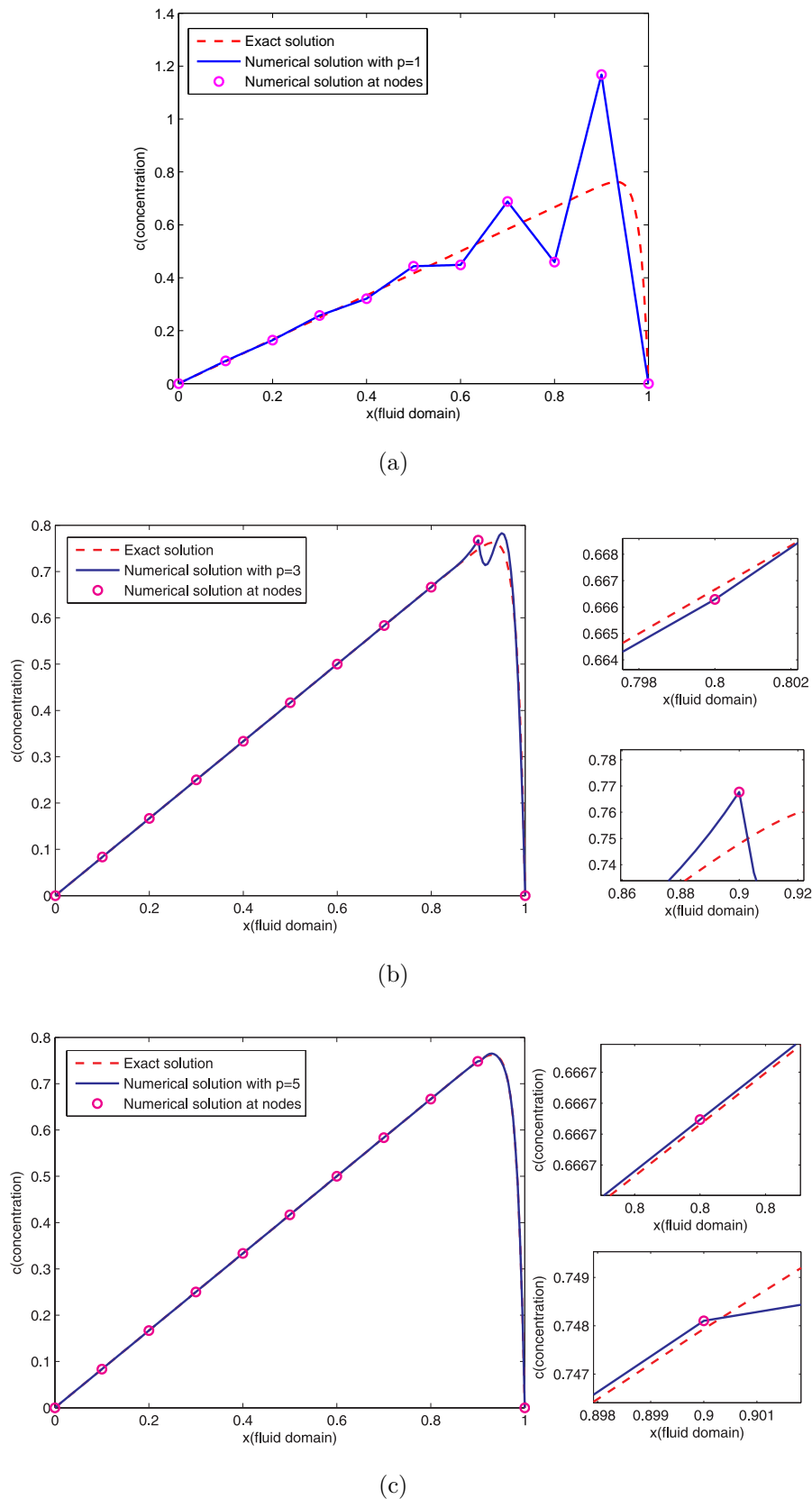
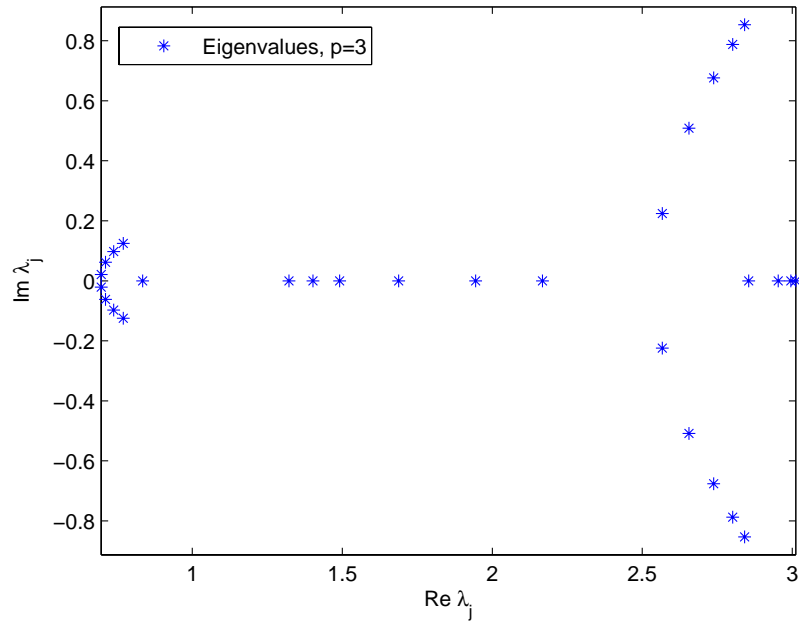
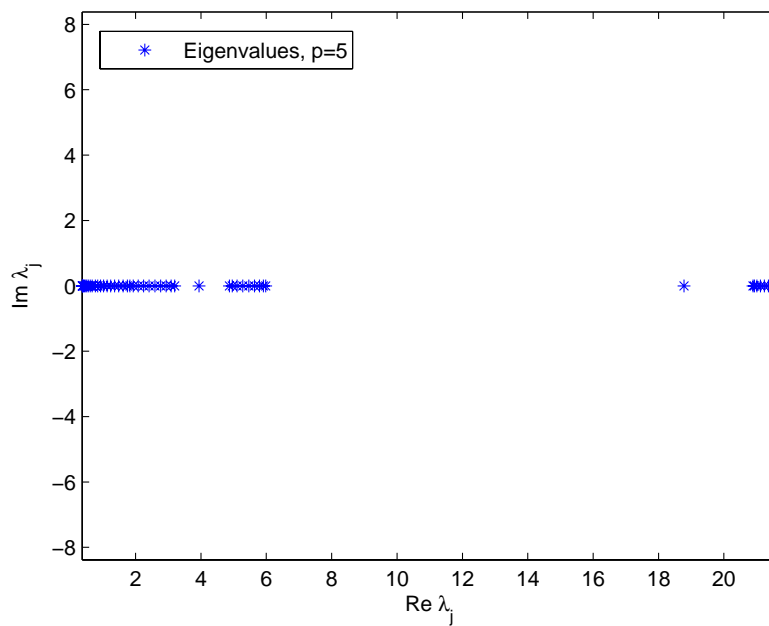


Figure 4.8: Comparison of the numerical and exact solutions using different polynomial degrees



(a)



(b)

Figure 4.9: Eigenvalues are computed for $p = 3$ and $p = 5$

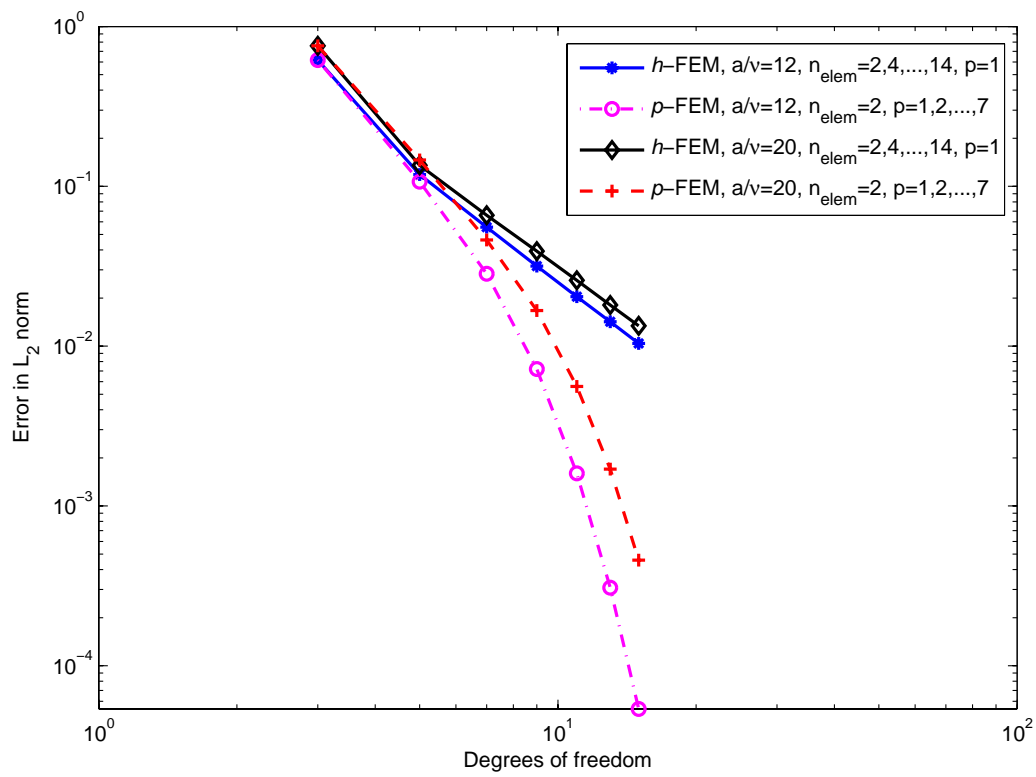


Figure 4.10: Error in L_2 norm in Equation 4.42 with different *Péclet* numbers

Chapter 5

Finite Cell Method in transport problems in porous media

5.1 Basic principles

We consider a linear convection-diffusion single-component transport problem in porous media. The basic partial differential equation describing the transport of a dissolved contaminant in a steady state reads

$$\begin{aligned} \nabla \cdot (\vec{q}c) - \nabla \cdot (\theta\nu\nabla c) &= f & \text{on } \Omega \\ c &= c_D & \text{at } \Gamma_D. \end{aligned} \quad (5.1)$$

Here, c is the unknown concentration, ν is the effective diffusion coefficient, \vec{q} is Darcy's velocity, θ is the volumetric water content, f is the source term and c_D denotes the prescribed concentration on the Dirichlet boundary Γ_D . The weak form of Equation 5.1 on a given domain Ω then reads

$$\mathcal{B}(c, w) = \mathcal{F}(w). \quad (5.2)$$

in which c is the concentration and w is a test function. When Neumann boundary conditions are absent, the operators \mathcal{B} and \mathcal{F} are defined as

$$\mathcal{B}(c, w) := \int_{\Omega} [\vec{q}c \cdot \nabla w + \theta\nu\nabla c \cdot \nabla w] d\Omega. \quad (5.3)$$

$$\mathcal{F}(w) := \int_{\Omega} w^T f d\Omega \quad (5.4)$$

The FCM now embeds the physical domain Ω in an extended domain Ω_e , see Figure 5.1. The physical domain is taken into account at the integration level of the weak formulation, simply setting appropriate material coefficients in and outside Ω .

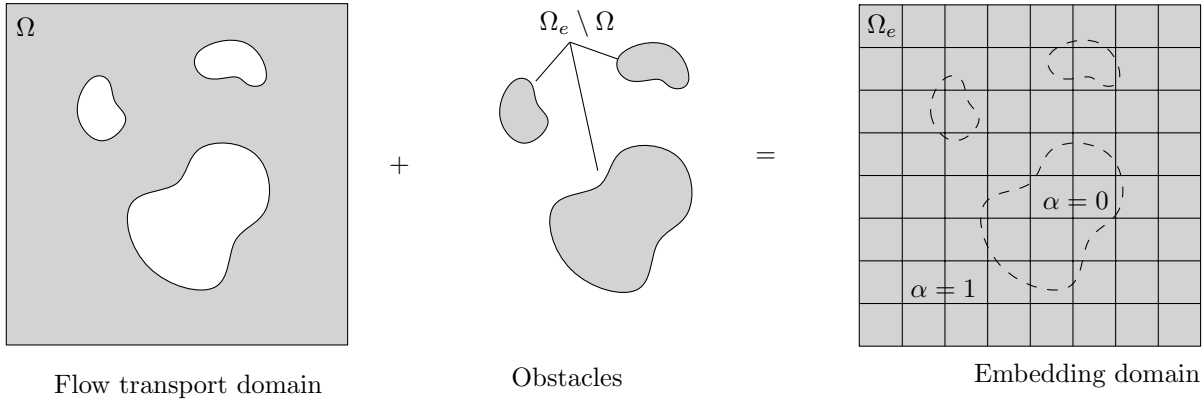


Figure 5.1: The physical, or flow transport domain Ω is embedded in the fictitious or embedding domain Ω_e

An extended bilinear form is introduced in the embedding domain Ω_e .

$$\mathcal{B}_e(c, w) := \int_{\Omega_e} [\vec{q}_e c \cdot \nabla w + (\theta\nu)_e \nabla c \cdot \nabla w] d\Omega \quad (5.5)$$

where \vec{q}_e is Darcy's velocity and $(\theta\nu)_e$ is the effective diffusion coefficient on the embedding domain with the values

$$\begin{cases} \vec{q}_e = \alpha \cdot \vec{q} \\ (\theta\nu)_e = \alpha \cdot \theta\nu. \end{cases} \quad (5.6)$$

The value of α in Equation 5.7 denotes the physical and fictitious part of the embedding domain.

$$\alpha = \begin{cases} 1 & \text{in } \Omega \\ 0 & \text{in } \Omega_e \setminus \Omega \end{cases} \quad (5.7)$$

Equation 5.5 can now be rewritten as

$$\begin{aligned} \mathcal{B}_e(c, w) &= \int_{\Omega_e} [\vec{q}_e c \cdot \nabla w + (\theta\nu)_e \nabla c \cdot \nabla w] d\Omega_e \\ &= \int_{\Omega_e} \alpha \cdot [\vec{q} c \cdot \nabla w + \theta\nu \nabla c \cdot \nabla w] d\Omega_e \\ &= \int_{\Omega} [\vec{q} c \cdot \nabla w + \theta\nu \nabla c \cdot \nabla w] d\Omega \\ &+ \int_{\Omega_e \setminus \Omega} 0 \cdot [\vec{q} c \cdot \nabla w + \theta\nu \nabla c \cdot \nabla w] d\Omega_e \setminus \Omega. \end{aligned} \quad (5.8)$$

It is evident that the bilinear form in Equation 5.8 is equivalent to the original formulation on the physical domain given in Equation 5.2. We would also like to point out that the second

part of the equation, which is defined on $\Omega_e \setminus \Omega$, does not contribute any energy to the solution.

The extended domain Ω_e is now meshed into 'cells' of a simple Cartesian grid (see right-hand section of Figure (5.1)) in which high order Ansatz functions are defined. These functions are used to compute a finite element approximation, taking into account the physical material properties in the original domain Ω and the fictitious material (i.e. zero-values) outside. At this point, it is important to emphasize that, in contrast to the classical low order finite element shape functions, high order Ansatz functions allow for jumps in the material coefficients (from 1 to 0) in an element, without necessarily suffering from deterioration of the approximation quality. It is, however, imperative to integrate element matrices accurately in cells that are cut by the boundary of the domain Ω . Various methods, ranging from (very) high order Gaussian integration [48] to an octree-based integration formula [18, 1], have been investigated.

In this thesis, we divide the cells into a uniform grid of sub-cells, where those that are intersected by the boundary are integrated using an adaptive Gaussian approach (see [18, 1]). Finally it should be noted that, for numerical reasons, α is not set to zero in the implementation of FCM, but to a small positive value. This serves to introduce a minor modeling error, which is usually much smaller than the discretization error and can thus be disregarded.

5.2 Different integration schemes

The integration error plays an important role in the FCM, since the geometry is described implicitly by the parameter α in Equation 5.7 at each Gaussian point. The Gaussian quadrature rule yields an accurate result for the integral of a function that can be approximated satisfactorily using polynomials. Due to the discontinuity of α within one element in the FCM, however, the standard Gaussian quadrature scheme is unable to produce the highest level of accuracy. Other adapted integration schemes are accordingly called for with the FCM.

5.2.1 Gaussian quadrature employing over-integration

The Gaussian quadrature rule is conceived in such a way that n Gaussian points can integrate a polynomial function of degree $2n - 1$ exactly [20]. In the standard FEM, if shape functions are polynomials of degree p , then the maximum polynomial degree of the system matrix is $2p + 1$. Then the minimum required number of Gaussian points n_{gp} is

$$n_{gp} = p + 1 \geq \frac{2p + 1}{2}. \quad (5.9)$$

Nevertheless, this amount of Gaussian points is still not sufficient for discontinuous functions, which is usually the case with the FCM. So, for some simple examples, such as the one in Section 5.3.1, more than $p + 1$ Gaussian points are employed to improve the integration accuracy.

There is no guarantee, however, that merely increasing the number of Gaussian points will solve the problem. For example, in Figure 5.2, the discontinuity occurs at $\xi = 0$ and more Gaussian points are required there. Due to the unequal distribution of the Gaussian points

shown in Figure 5.2, integration points tend to be allocated at two ends of an element rather than the middle part, where more integration points would be required. It means that the required number of Gaussian points depends on the position where the discontinuity occurs, which makes the integration scheme unpredictable and inefficient.

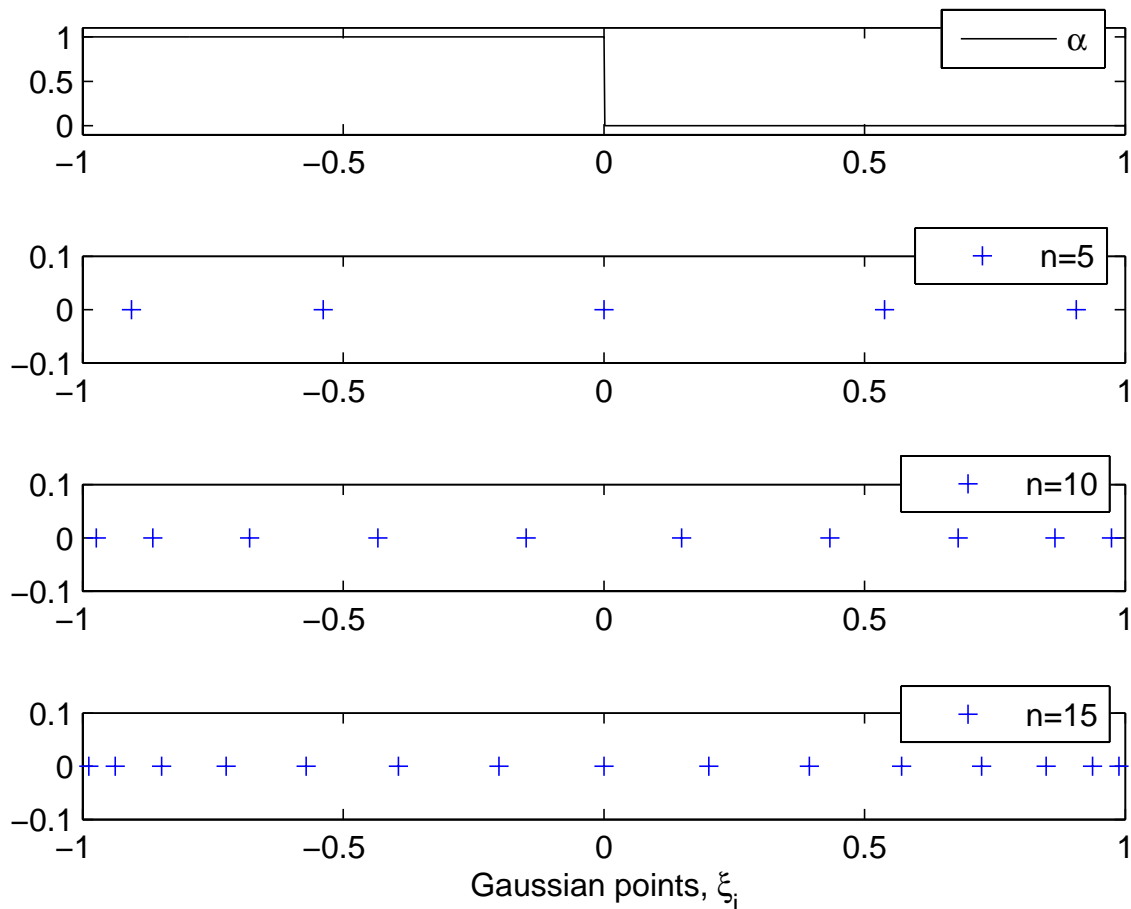


Figure 5.2: Distribution of Gaussian points for 1D problems

Compared to this scheme, subcell integration approaches introduced in the next sections make integration more efficient.

5.2.2 Subcell integration schemes

In order to decrease the integration error, cells are cut into smaller units, each unit being called a subcell. Subcells are introduced for integration purposes only, and the number of degrees of freedom does not change.

Let us take a one-dimensional convection-diffusion equation as an example to derive the mathematical expression for the subcell integration. For the sake of simplicity, the one-dimensional domain with the length l is divided into n elements of equal length. The element diffusion matrix described in Equation 4.5 can be rewritten as

$$\begin{aligned} K_{ij}^e(x) &= \int_0^l N_{i,x}(x) \nu N_{j,x}(x) dx \\ &= \int_0^l B_i(x) \nu B_j(x) dx, \end{aligned} \quad (5.10)$$

where $B_i(x)$ is the abbreviation of the first derivative of $N_i(x)$ with respect to x . Figure 5.3 shows the subcell division in a one-dimensional problem.

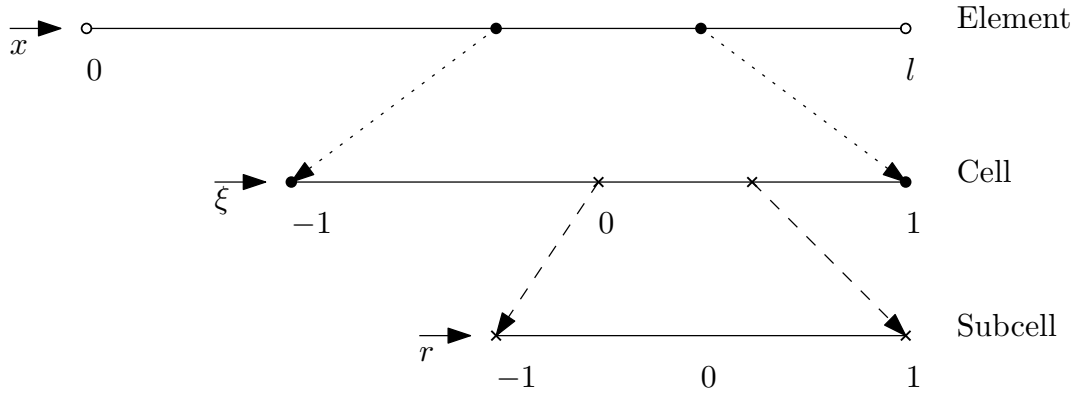


Figure 5.3: The projection of a one-dimensional element into the subcell coordinate

A cell can be subdivided into uniform or non-uniform subcells and Gaussian integration points are located on subcells. The first step is to compute the element diffusion matrices in the cell coordinate ξ

$$\begin{aligned} \int_0^l B_i(x) \nu B_j(x) dx &= \int_{-1}^1 \left[B_i(\xi) \frac{d\xi}{dx} \right] \nu \left[B_j(\xi) \frac{d\xi}{dx} \right] \frac{dx}{d\xi} d\xi \\ &= \sum_{k=0}^{n-1} \int_{-1+kl/n}^{-1+(k+1)l/n} \left[B_i(\xi) \frac{d\xi}{dx} \right] \nu \left[B_j(\xi) \frac{d\xi}{dx} \right] \frac{dx}{d\xi} d\xi. \end{aligned} \quad (5.11)$$

Each cell is then again projected into the subcell coordinate r and approximated by means of

n Gaussian Points

$$\begin{aligned}
& \int_{-1+il/n}^{-1+(i+1)l/n} \left[B_i(\xi) \frac{d\xi}{dx} \right] \nu \left[B_j(\xi) \frac{d\xi}{dx} \right] \frac{dx}{d\xi} d\xi \\
&= \int_{-1}^1 \left[B_i(\xi(r)) \frac{d\xi}{dx} \right] \nu \left[B_j(\xi(r)) \frac{d\xi}{dx} \right] \frac{dx}{d\xi} \left(\frac{d\xi}{dr} dr \right) \\
&\approx \sum_{p=1}^n \left[B_i(\xi(r_p)) \frac{d\xi}{dx} \right] \nu \left[B_j(\xi(r_p)) \frac{d\xi}{dx} \right] \frac{dx}{d\xi} \frac{d\xi}{dr} w_p.
\end{aligned} \tag{5.12}$$

The components of the subcell stiffness matrices are added to the cell stiffness matrices, which does not increase the degrees of freedom but only improves the integration accuracy. Finally, a global stiffness matrix is obtained by assembling all cell stiffness matrices together. Two different sorts of subcell integration schemes are introduced in the following sections.

5.2.2.1 Uniform subcell integration scheme

Based on the equations derived above, the uniform subcell integration scheme can be implemented for a three-dimensional example. As depicted in Figure 5.4, Gaussian integration points are located on each individual subcell.

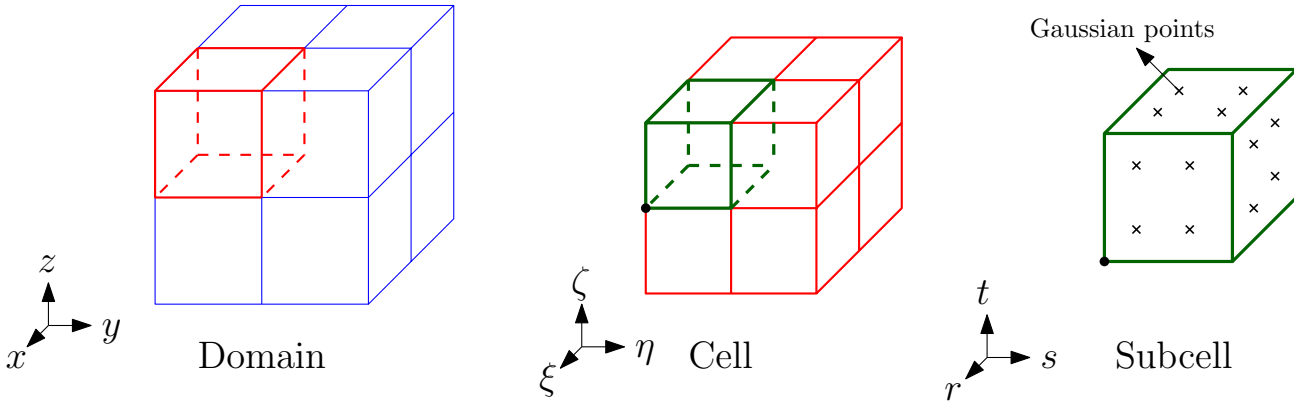


Figure 5.4: The projection of a three-dimensional element into the subcell coordinate

The optimal number of subcells required in the integration process can be determined by comparing the effective domain iteratively. An effective domain is the sum of the domain of subcells, where at least one Gaussian point is inside the physical domain. The coordinates of Gaussian integration points of the subcells are evaluated at each iteration to check whether they are in the physical or the fictitious domain. The corresponding weight function of a Gaussian point is then multiplied by the penalization factor α and its value is allocated to the effective domain. When the difference between the current effective domain and the previous one is smaller than the prescribed tolerance, the number of subcells in the current iteration is deemed to be sufficient.

The optimal number of subcells is calculated using the flowchart in Figure 5.5, which is implemented in AdhoC. Ω_{old} and Ω_{new} denote the effective domain before and after the computation at each step, whereas Ω_{cell} is the whole domain of the corresponding cell.

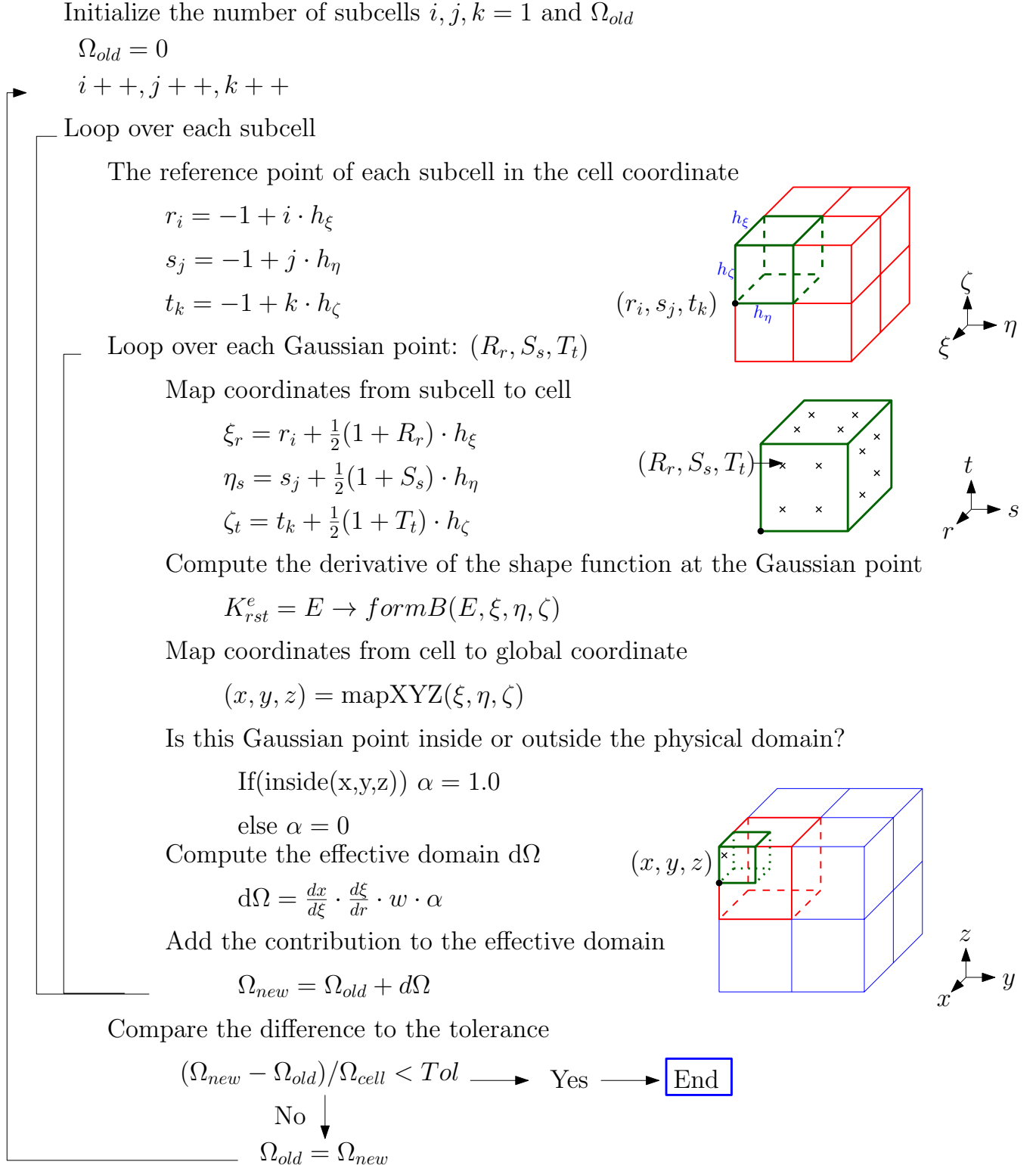


Figure 5.5: The uniform subcell integration implemented in AdhoC

5.2.2.2 Adaptive integration scheme

As opposed to the uniform subcell integration scheme, the adaptive integration scheme employs subcells of varying sizes created by a hierarchic decomposition. In the uniform subcell approach, when the integration error is larger than the predefined tolerance, each individual cell will be cut into the same number of subcells, no matter where the cell is located. However, cutting the cell located completely inside or outside of the physical domain does not help to improve the integration accuracy but only makes the computation inefficient. For this reason, we employ the adaptive integration scheme to overcome the shortcoming [18].

The first step of this approach is to define a certain number of checkpoints in each cell (or subcell) and check whether the cell (or subcell) is cut by the boundary. If all the checkpoints are located inside (or outside) the physical domain, there is no need to divide the cell (or subcell) any further, thus making the computation more efficient. At each refinement level, $\alpha = 0$ or $\alpha = 1$ is assigned for each Gaussian point according to the physical coordinate. Then the effective area in the physical domain can be computed by adding up the weighting functions of each Gaussian point multiplied by α . The cell (or subcell) will be further refined until the effective area computed at the last refinement step is very close to the one computed at the current step. The flowchart of the adaptive integration scheme is illustrated in Figure 5.6. A_{old} and A_{new} denote the effective area before and after computation at each step, whereas A_{cell} is the whole area of the corresponding cell.

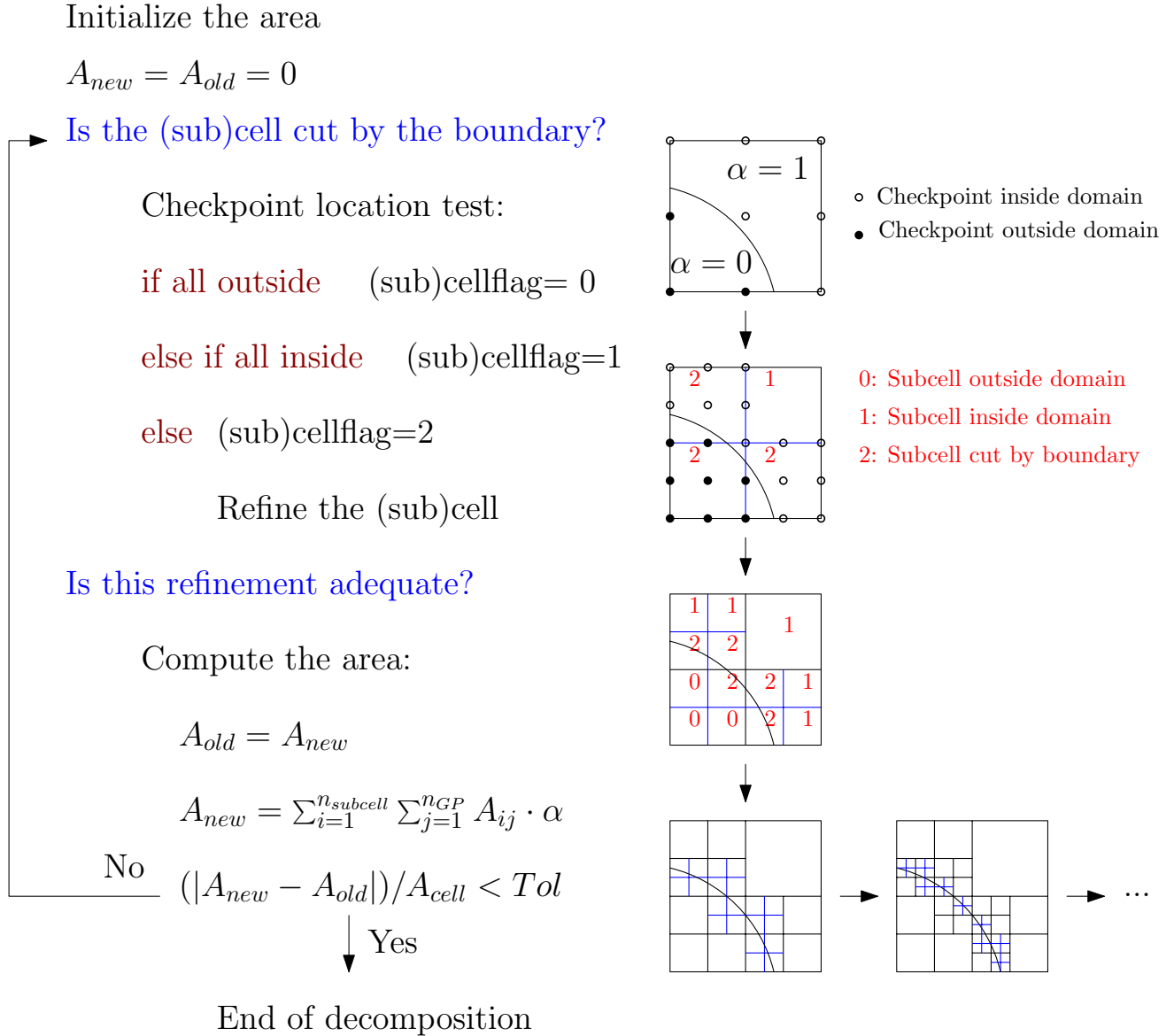


Figure 5.6: The adaptive subcell integration implemented in AdhoC

5.3 FCM in single-component reactive transport problems in porous media

5.3.1 The performance of the FCM in 1D transport problems

In this section we investigate the performance of the FCM for a one-dimensional single-component transport problem, which may seem trivial but nevertheless sheds some light on the performance of the method. As formulated, the example displays a material-void problem whose schematic interpretation is depicted in Figure 5.7.

Since convective flux is physically uninterpretable in the 1D material-void domain, transportation is carried out by means of a pure diffusion process. The associated differential equation

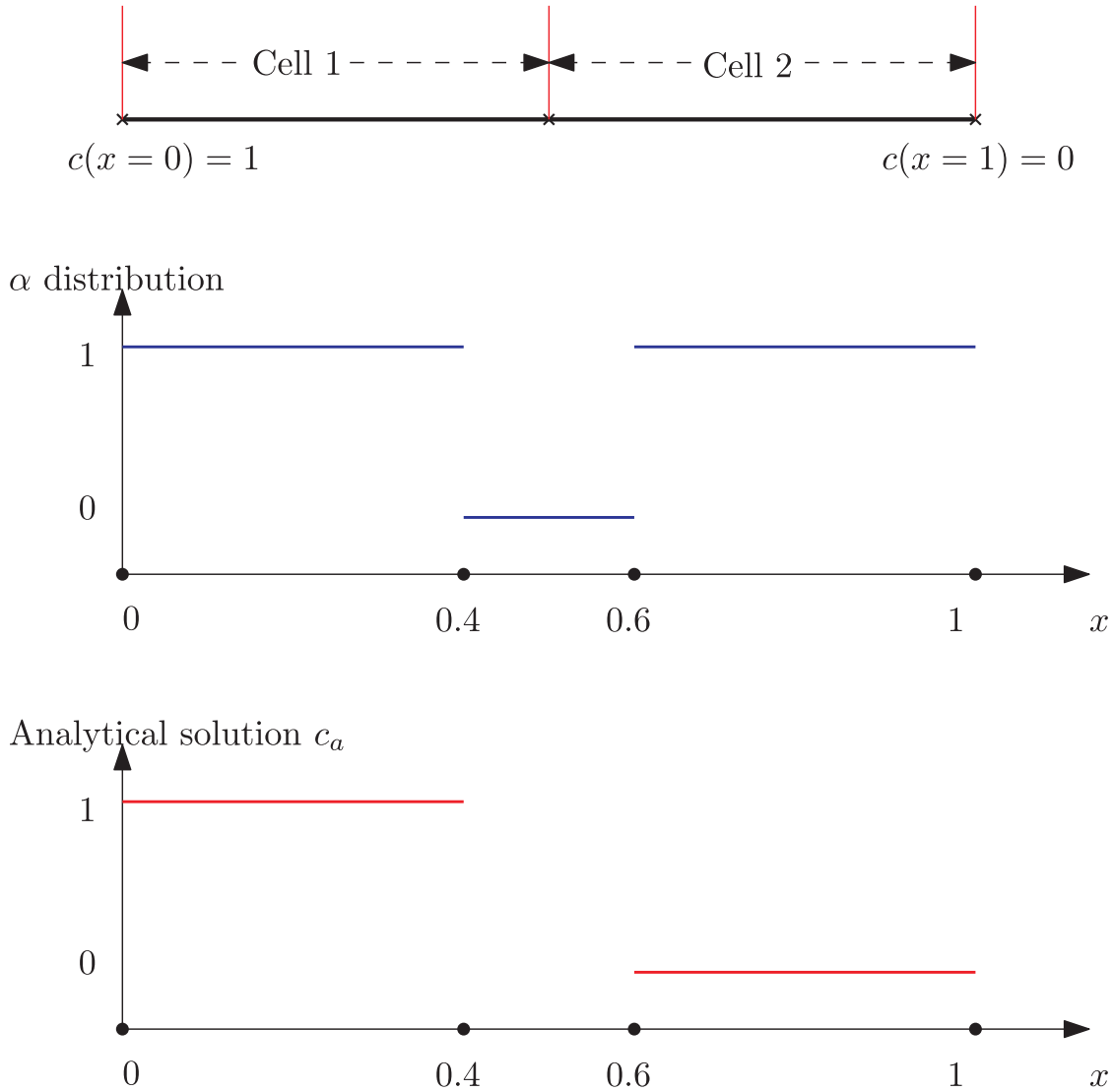


Figure 5.7: One-dimensional diffusion transport example

in domain $\Omega = (0, 1)$ is

$$\begin{aligned} \frac{d}{dx}(\theta\nu \frac{dc}{dx}) &= 0 \\ c &= 0 \quad \text{at } x = 0 \\ c &= 1 \quad \text{at } x = 1. \end{aligned} \tag{5.13}$$

With the standard finite element method, the boundaries at $x = 0.4$ and at $x = 0.6$ would have to be respected by the mesh on which the shape functions are defined. This is not necessary using the FCM, however. We define the extended domain as $\Omega_e = \{x | 0 \leq x \leq 1\}$ and divide it into two cells only, whose common boundary does not coincide with the discontinuity in the effective diffusion coefficient.

In addition, a homogeneous Neumann boundary should be imposed at the material-void

boundary $x = 0.4$ and $x = 0.6$, since there is no flux in the void domain. However, it is not feasible to express the homogeneous Neumann boundary condition explicitly in the FCM, since material-void boundary is not a part of $\partial\Omega$. The void part is accordingly treated as a different 'material' set in the computational domain. A homogeneous Neumann boundary condition can also be applied by setting material properties to zero in the void domain. This effect can be achieved by multiplying parameter α in Equation 5.7, which indicates on the other hand that the void part is regarded as a fictitious domain in the FCM.

Since the element boundary is not usually in line with the physical-fictitious boundary in the FCM, there are several different materials within one cell, which are expressed by the stiffness matrix at each Gaussian point. To minimize the integration error resulting from insufficient Gaussian points for discontinuous functions, the numerical integration of the stiffness matrix in this problem is then carried out by over-integrating the cells with 40 Gaussian points each¹. The p -extension of the Ansatz is then employed, inherited from the classical high order finite element method.

With α distribution shown in Figure 5.7, Equation 5.13 has a piecewise constant analytical solution in the physical domain

$$c(x) = \begin{cases} 1 & \text{in } x \in [0, 0.4] \\ 0 & \text{in } x \in [0.6, 1]. \end{cases} \quad (5.14)$$

The computational results are depicted in Figure 5.8. For linear and even cubic Ansatz spaces, the numerical solution is only a very rough approximation of the piecewise constant analytic solution. Nevertheless, $p = 5$ already provides an acceptable result and $p = 7$ yields an accurate result. The solution in the void part of the domain (i.e. the part in between $0.4 \leq x \leq 0.6$ where $\alpha=0$) is shown here on purpose, although it does not have any physical meaning. As the shape functions forming the solution are piecewise polynomials, the approximation simply extends smoothly into this void part. Provided the shape functions represent a good transition between the physical domain parts, they do not harm the quality of the approximate solution there.

The numerical error quantified in L_2 -norm is defined by Equation 4.42. Figure 5.9 shows the exponential convergence in L_2 -norm of the p -extension.

Note that value α is chosen to be 0 in this example. It will not cause any singularity problem for the stiffness matrix since there are only two elements in this case. When there are more elements, however, so that one of these elements only contains a void part, $\alpha = 0$ will introduce a singular stiffness matrix. In practice, we therefore choose a very small value for α instead of 0. It is important to make a compromise and choose a value for α that is somewhere between the condition number of the stiffness matrix and the accuracy. Figure 5.10 shows the influence of α on error in the L_2 -norm and condition number of the stiffness matrix in this 1D example,

¹Alternatively, a composed integration scheme that respects the boundaries at $x = 0.4$ and at $x = 0.6$ could be used to reduce the integration error. However, simple over-integration already provides accurate results in this example

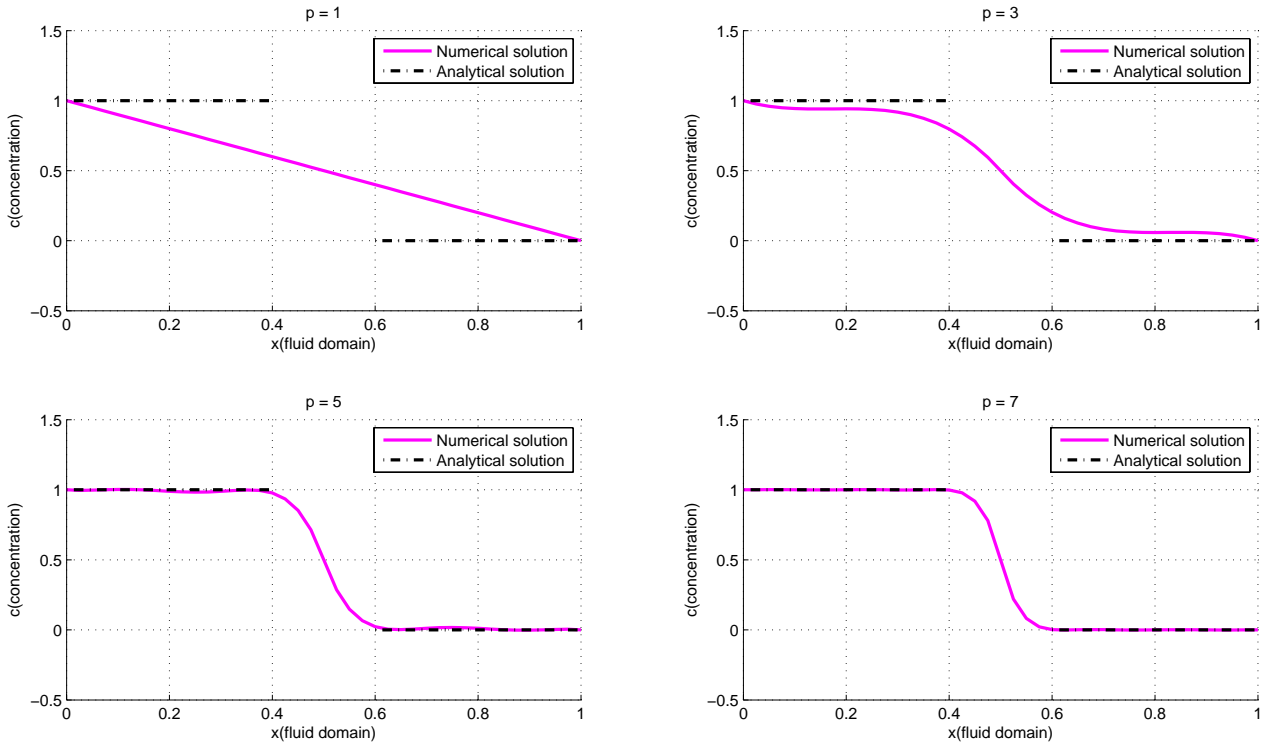


Figure 5.8: 1D diffusion problem solved by FCM with different Ansatz degrees

where the polynomial degree is chosen to be 7. The value of α can be chosen according to the required error or condition number level.

5.3.2 The performance of the FCM in 2D transport problems

This section investigates the performance of the FCM for two-dimensional problems and the influence of convection dominance on the convergence behavior, which will then be compared to the standard finite element method. In the first example, the physical domain is a square measuring $4m \times 4m$, containing a circular, impermeable obstacle with a radius of $1m$ located at its center. Dirichlet boundary conditions are imposed as follows: $c(x = -2, y) = 1$, $c(x = 2, y) = 0$ on the left and right-hand boundaries of the embedding domain: $\Omega = [-2, 2] \times [-2, 2]$ and the homogeneous Neumann boundary condition is applied to the upper and lower boundaries of the domain Ω . We set the effective diffusion coefficient to $\nu = 1m^2/h$ and investigate the flow for different *Péclet* numbers.

The reference solution is computed by means of a classical p -FEM discretization with a boundary-conforming mesh. With the p -FEM approach, the boundary conditions are the same as the ones imposed in the FCM model. In addition, the homogeneous Neumann boundary condition is also applied explicitly at the boundary of the circular domain, indicating that the flux cannot flow into the circular domain. The quarter circle in the elements is represented

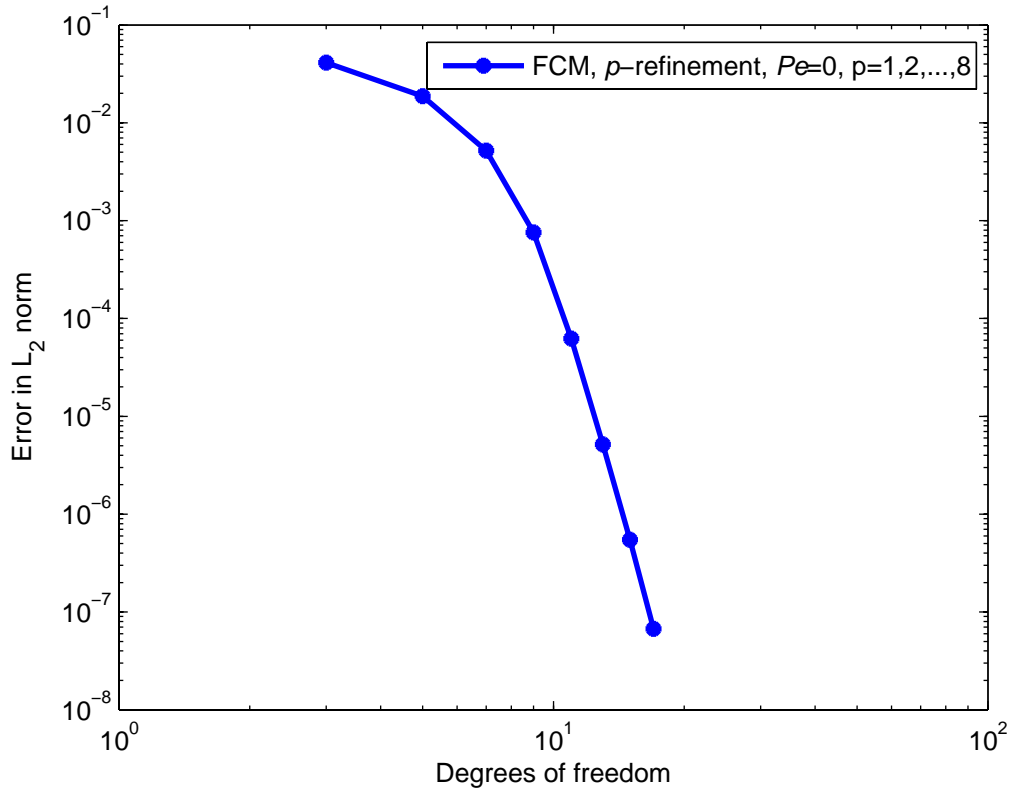


Figure 5.9: Convergence rate of 1D example with respect to p -refinement

with absolute geometric precision in the spatial discretization by employing the blending function method [24]. The mesh is depicted in Figure 5.11.

By contrast, the FCM uses 4 cells which are not conform with the boundary. They are obtained by means of simple Cartesian subdivision resulting in 2×2 cells. The integration of the stiffness matrix is performed numerically in a composed manner on 6×6 subcells. A schematic sketch is depicted in Figure 5.12. Please see Section 5.2.2.1 for details of the integration scheme.

To begin with, let us consider the case of a pure diffusion problem with *Péclet* number 0. The reference solution, as computed by the boundary-conforming p -version of the FEM, and the solution computed by the FCM are shown in Figure 5.13.

These two results are compared once again in Figure 5.15 by investigating the solution along the diagonal cut-lines depicted in Figure 5.14 (left).

It is apparent that the FCM solution coincides very well with the reference solution obtained by the boundary-conforming p -version of the finite element method. This is, of course, only true in the physical domain. The solution in the void domain is arbitrary and can be disregarded. Again, it is only included here for illustrative reasons.

The relative error computed in the energy norm is depicted in Figure 5.16. In order to illus-

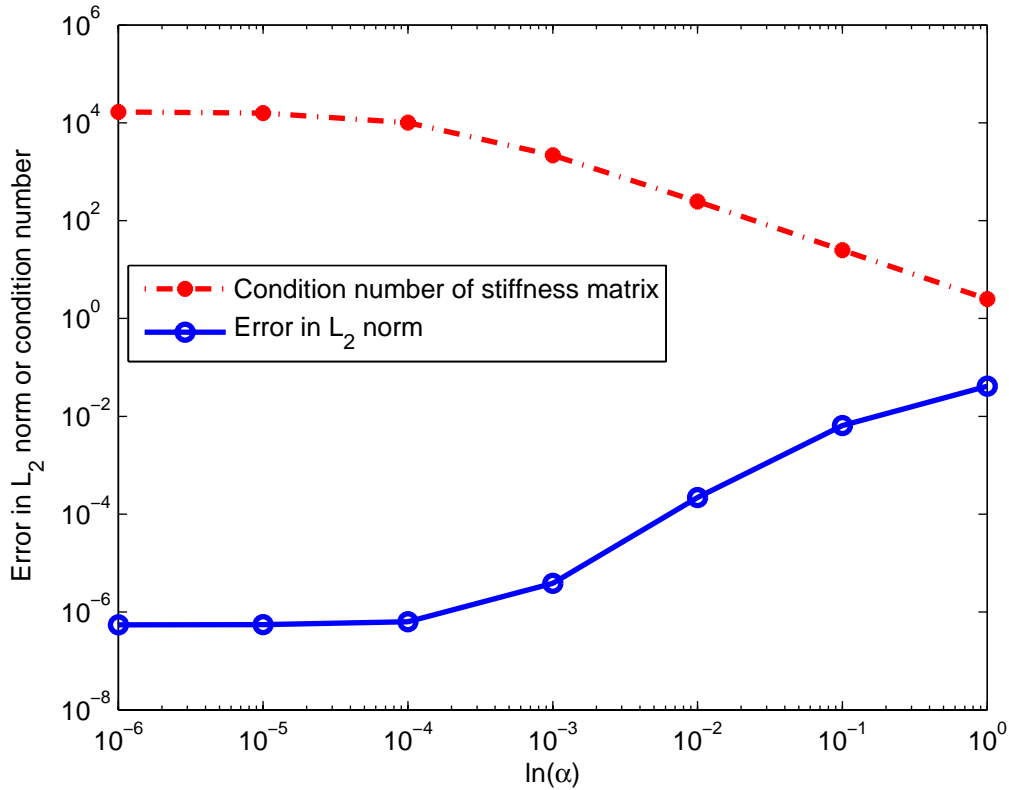


Figure 5.10: The influence of α on the error and condition number of the stiffness matrix

trate the convergence of the method, we compare the FCM to both a boundary-conforming p -extension and a classic h -extension. The h -extension was computed using meshes with elements possessing parabolic edges to approximate the shape of the circle. Both the p -extension and the FCM converge exponentially while the conventional h -version only exhibits algebraic convergence. As a result, the FCM needs up to two orders of magnitude less degrees of freedom to achieve the same accuracy as a classical h -version. In addition, only four cells are needed in the FCM in order to accurately approximate the results.

We will now proceed to take a closer look at a diffusion and a convection-dominated case. The mesh *Péclet* number is defined in Equation 2.11 and indicates which flux is dominant. In the convection-diffusion study, we establish the diffusion coefficient $\nu = 1m^2/h$ as a constant value. The diffusion and the convection-dominated cases are then obtained by setting Darcy's velocity to $0.5m/h$, $1m/h$ and $2m/h$, which results in a *Péclet* number of $Pe = 0.5$, $Pe = 1.0$ and $Pe = 2.0$, respectively. The results obtained by the FCM with different *Péclet* number are depicted in Figure 5.17.

The influence of the *Péclet* number on the convergence rate is evaluated by the error in the energy norm in Figure 5.18 and the L_2 -norm in Figure 5.19.

In both cases, as the degrees of freedom increase, the convergence behavior of the convection-dominated flow solved using the FCM is slightly inferior to the diffusion dominated case. Al-

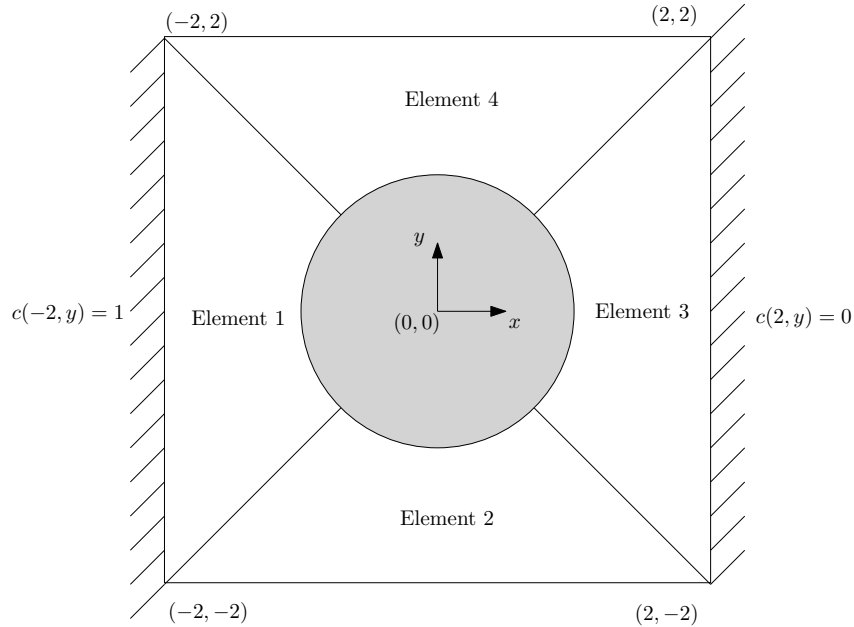


Figure 5.11: Boundary-conforming mesh of the p -version finite element method

though it has, in general, a lower convergence rate than the standard p -FEM, the convergence is still exponential. At this point, it should be noted that standard low order Bubnov-Galerkin approaches always exhibit instabilities for convection-dominated flows and stabilization is necessary in any case. By contrast, the approach presented here, which is based on high order Ansatz functions, remains stable without any artificially added stability measures for moderate *Péclet* numbers.

Another two-dimensional example was chosen to illustrate the further potential of the FCM for the simulation of flow in complex geometries. Obstacles of different sizes are embedded in the flow domain $\Omega = [-10, 10] \times [-10, 10]$, significantly increasing the effort for the generation of boundary-conforming meshes in the finite element method. The adaptive subcell integration scheme is applied in this example, as illustrated in Figure 5.20.

We apply the same boundary conditions as in the example above. The simulation results of the p -version of the FEM and the FCM are given in Figure 5.21 with $Pe = 1$ and Figure 5.22 with $Pe = 2$ respectively. The polynomial degree $p = 8$ is applied in both cases.

In analogy to the previous example, the cut-line for the $Pe = 1$ case is drawn along the diagonal of the domain in Figure 5.14 (right) and the simulation results are displayed in Figure 5.23. The conformity of the two solutions along the cut-line shows how accurately the FCM is able to approximate the solution even for those areas where the physical domain is very narrow compared to the size of the cells. These areas are usually difficult to mesh as they define the mesh size in their vicinity and accordingly increase the number of elements. This is particularly the case in 3D models, where it is a real challenge to obtain boundary-conforming meshes for domains where obstacles are almost touching each other.

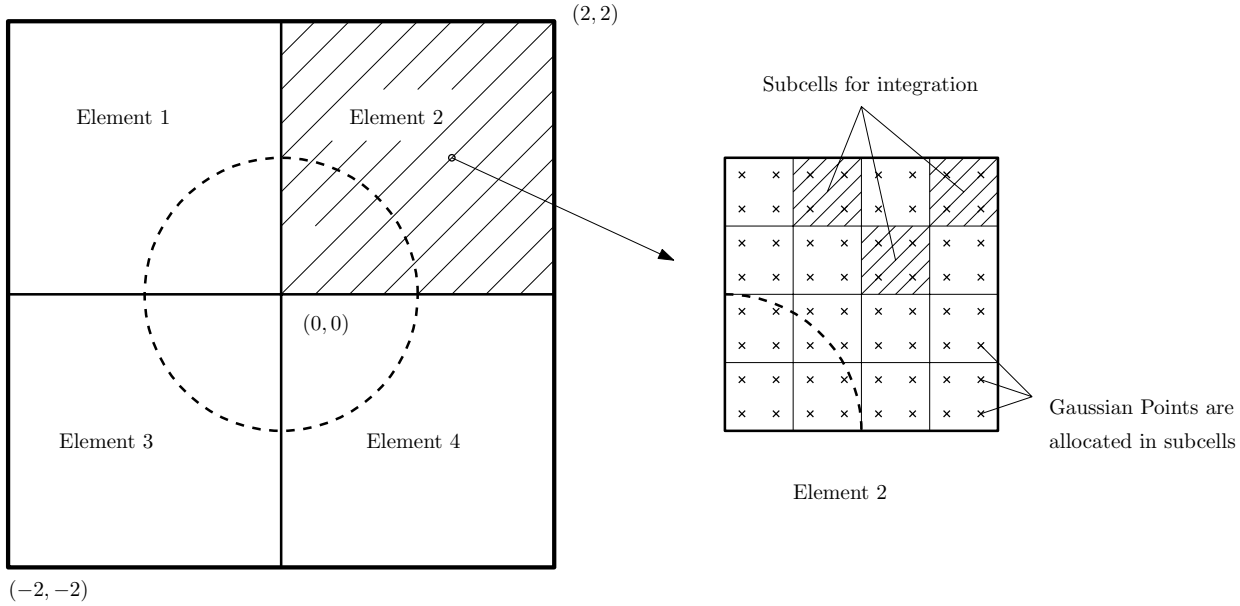


Figure 5.12: A simple structured mesh in the Finite Cell Method

5.3.3 The performance of the FCM in 3D transport problems

In reality, obstacles in flow regimes are often distributed randomly on a microscopic scale. To obtain effective macroscopic material properties it is, therefore, necessary to perform a large number of individual simulations, each with a different distribution of obstacles. Using classical simulation methods, it is nevertheless extremely time-consuming to generate a tailored computational mesh for each individual case. The FCM completely dispenses with this necessity and can accordingly compute efficiently and accurately on a large number of randomly generated granular media.

For the sake of illustration, a computational domain was generated with 100 randomly distributed spheres with random radii, see Figure 5.24.

The complex 3-dimensional, physical domain is now embedded in a cube and subdivided into $10 \times 10 \times 10$ structured cells. The integration is performed with $(p+1)^3$ Gaussian points in all cells that do not contain an inclusion, where p is the polynomial degree of the shape functions. A composed integration is only employed for cells which are cut by, or contain an inclusion. The polynomial degree of the Ansatz was chosen to be $p = 4$ in each cell for the given example, where the trunk space [60] was utilized. The real computation time is 26.7 hours on a single threaded process on Intel(R) Core(TM)2 Quad CPU Q6600@2.40GHz. The distribution of the concentration in the physical domain, as computed using the FCM, is depicted on a cutting plane lying parallel to the $x-y$ and the $x-z$ plane in Figures 5.25 and 5.26 respectively.

Due to some very narrow flow bridges between the obstacles, it is difficult to generate a boundary-conforming mesh in the p -FEM. However, the application of the FCM is not limited by the complexity of the geometry, and we can still obtain physically reasonable results with a simple structured mesh.

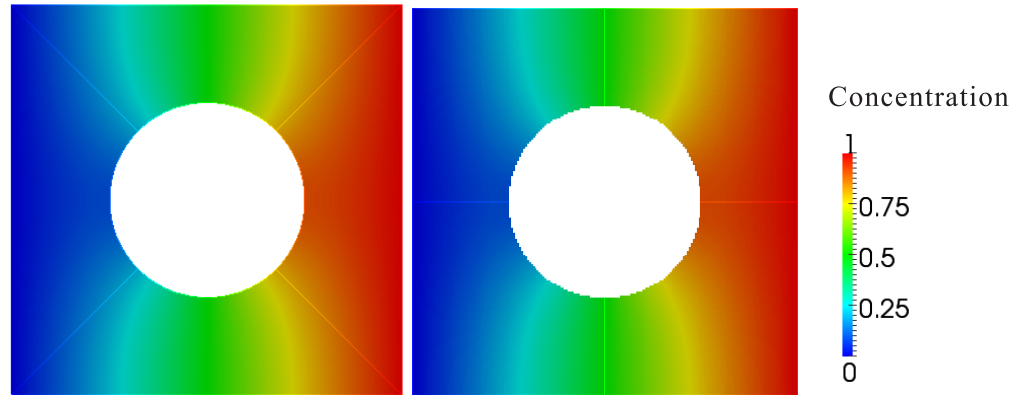


Figure 5.13: A pure diffusion problem solved by p -FEM (left) using boundary-conforming mesh and the FCM (right)

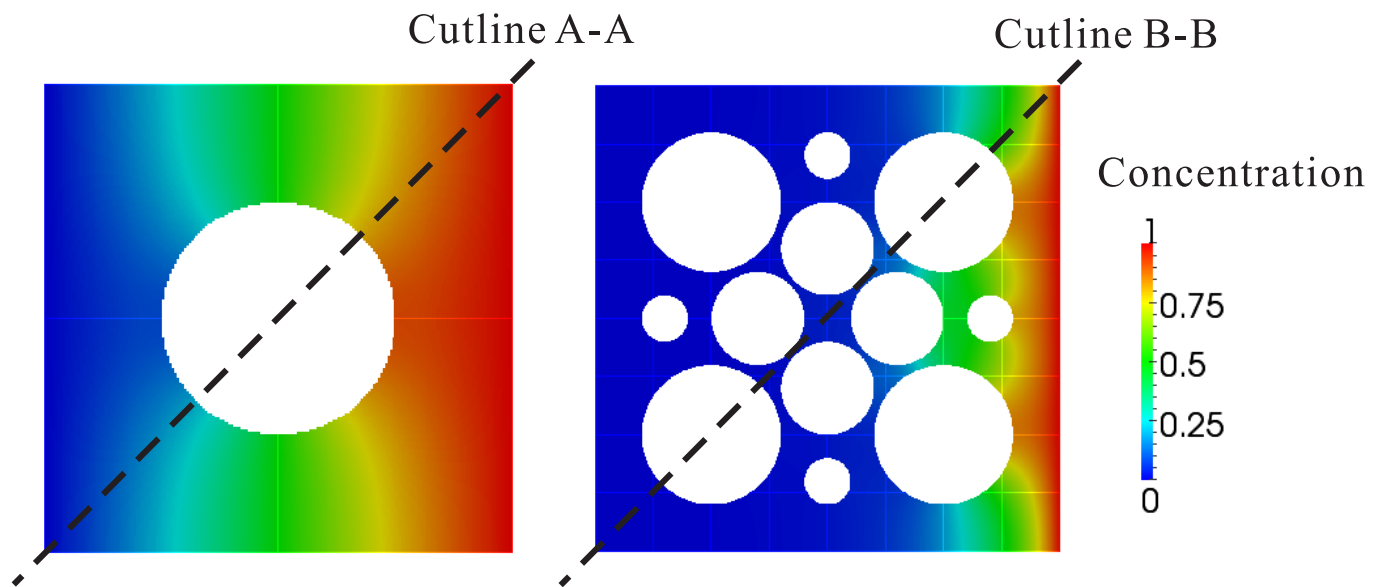


Figure 5.14: Illustration of cut-lines along the diagonal in two-dimensional problems

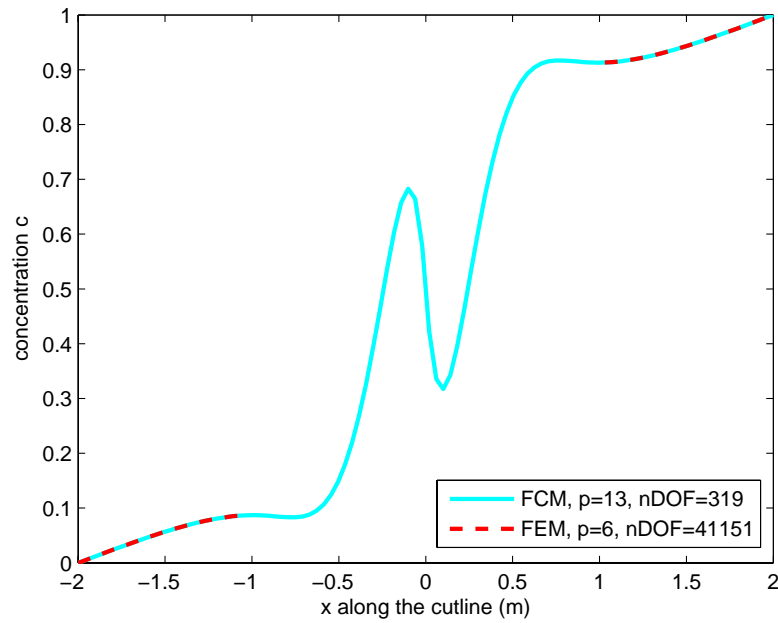


Figure 5.15: Comparison of solutions along the cut-line in the first two-dimensional problem

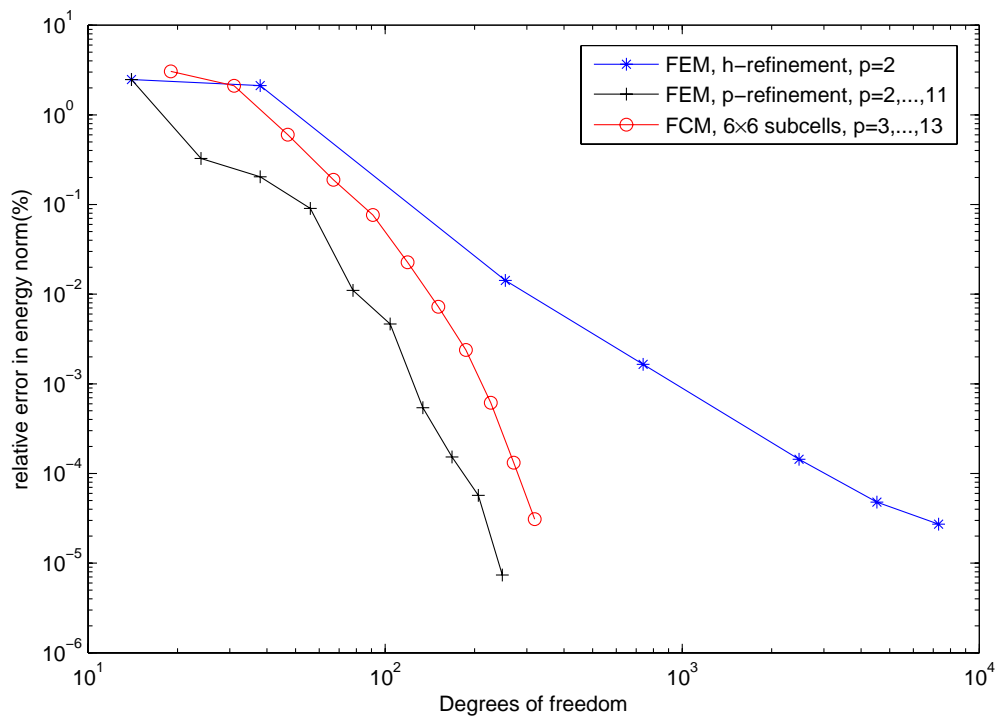


Figure 5.16: Convergence behavior of 2D example with respect to p -refinement

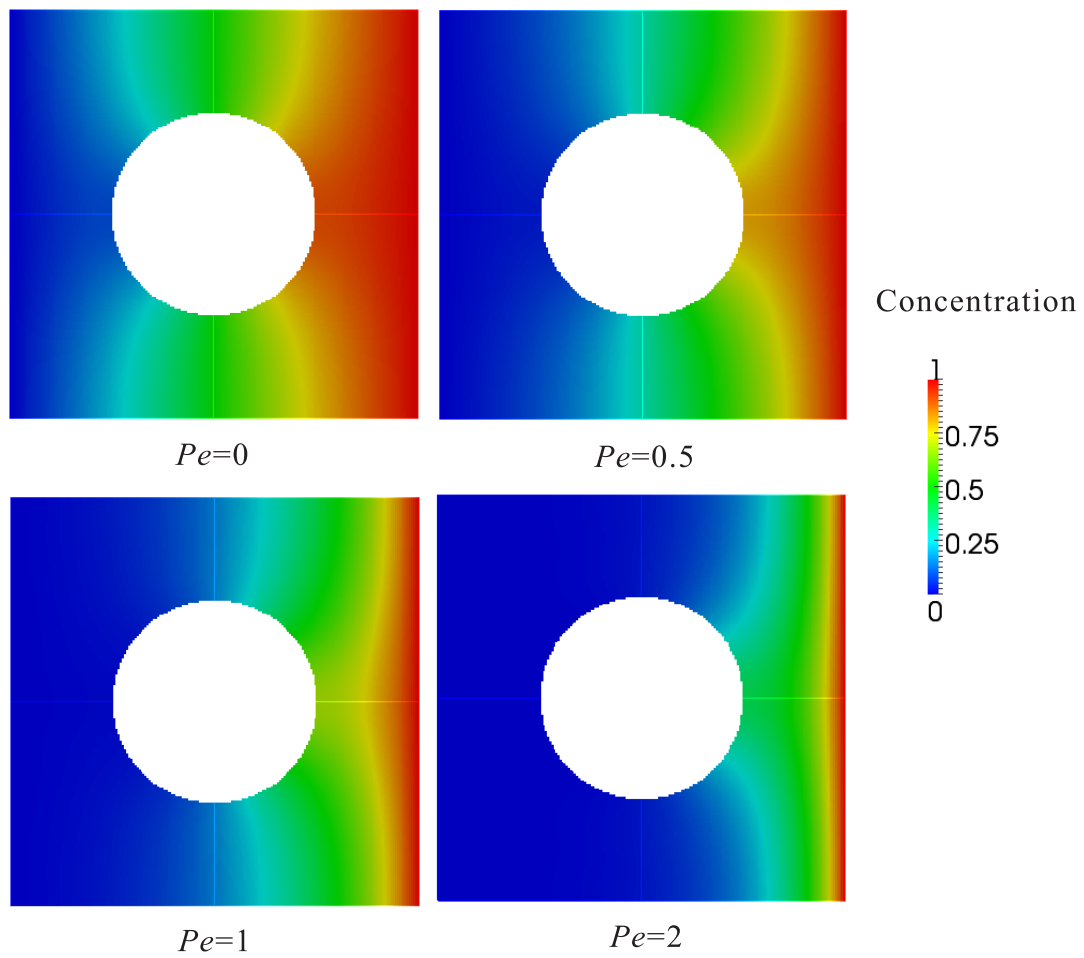


Figure 5.17: 2D benchmark problem solved by the Finite Cell Method, $p=8$

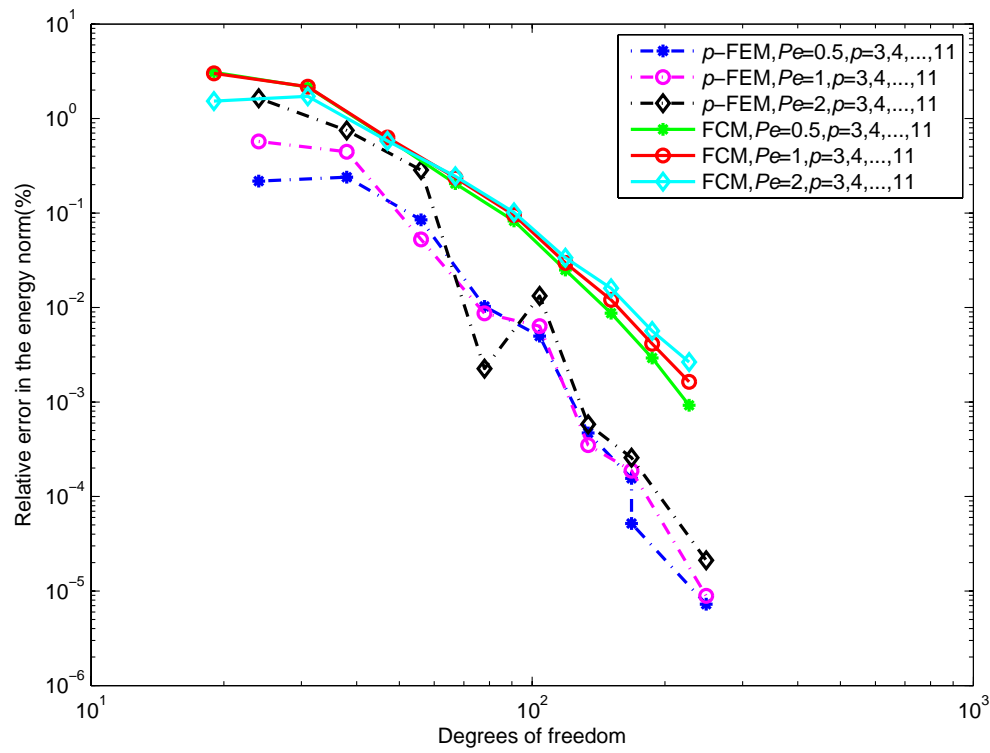


Figure 5.18: The influence of the Péclet number on the convergence behavior in the energy norm

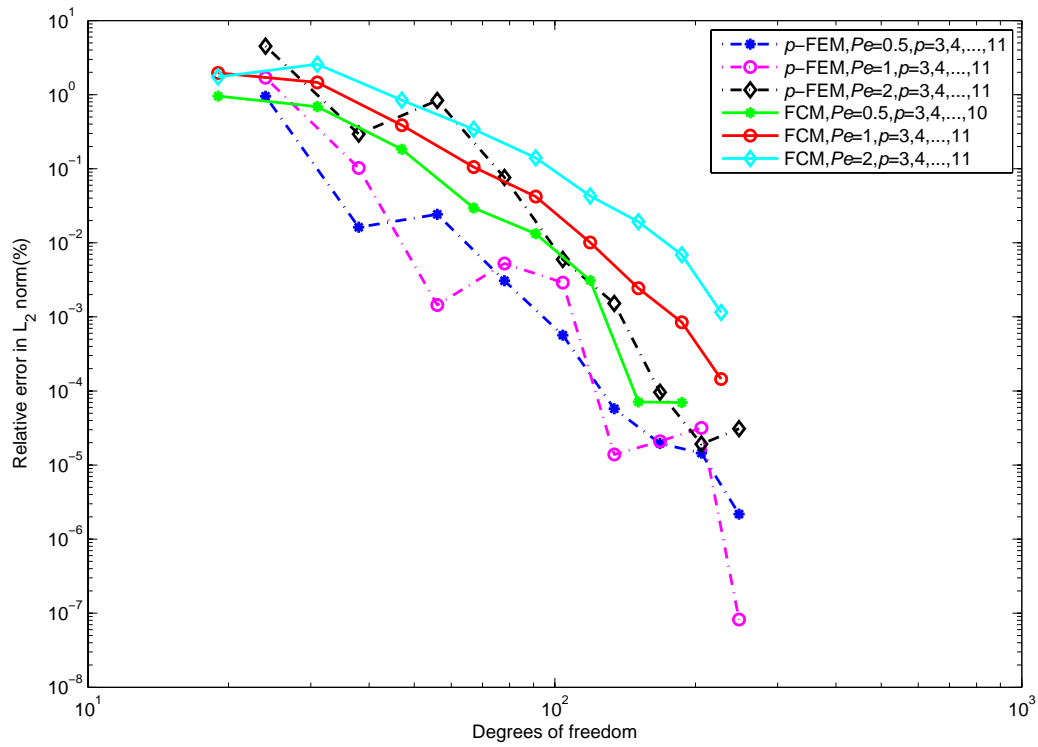


Figure 5.19: The influence of the *Péclet* number on the convergence behavior in the L_2 -norm

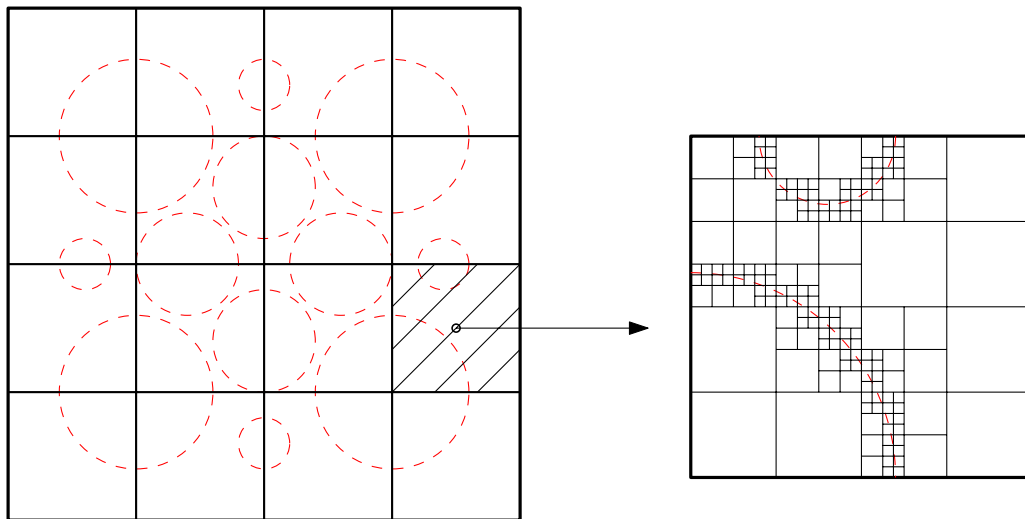


Figure 5.20: Adaptive subcell integration scheme for the second two-dimensional example

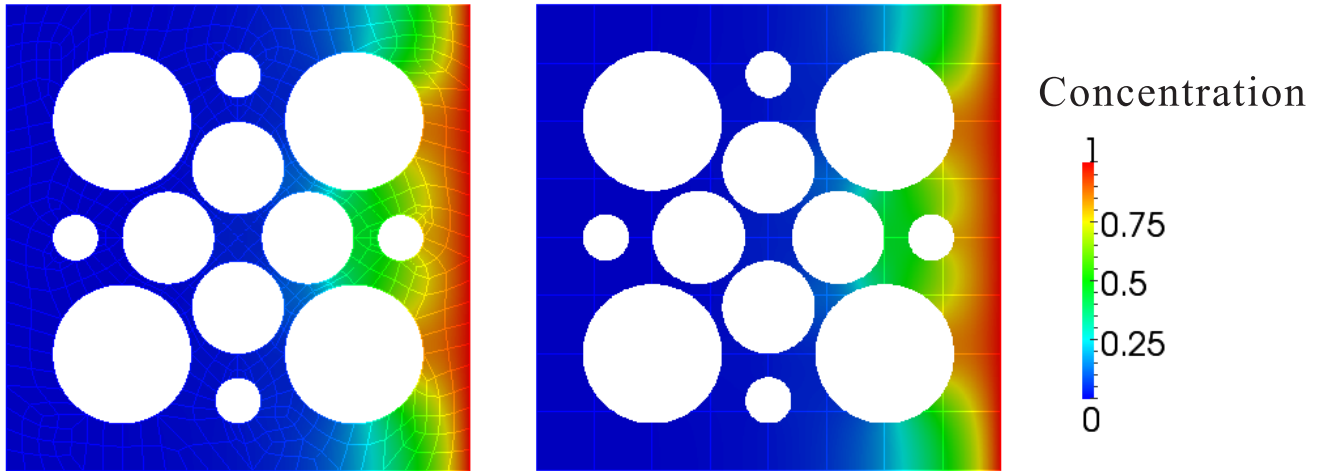


Figure 5.21: Numerical solution computed using p -FEM (left) and FCM (right) with $Pe = 1$

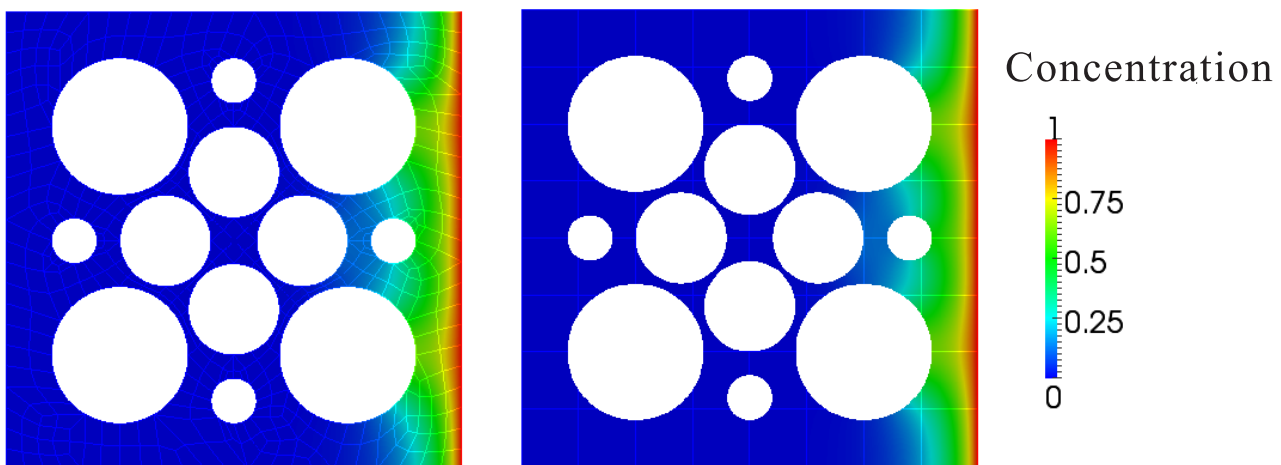


Figure 5.22: Numerical solution computed using p -FEM (left) and FCM (right) with $Pe = 2$

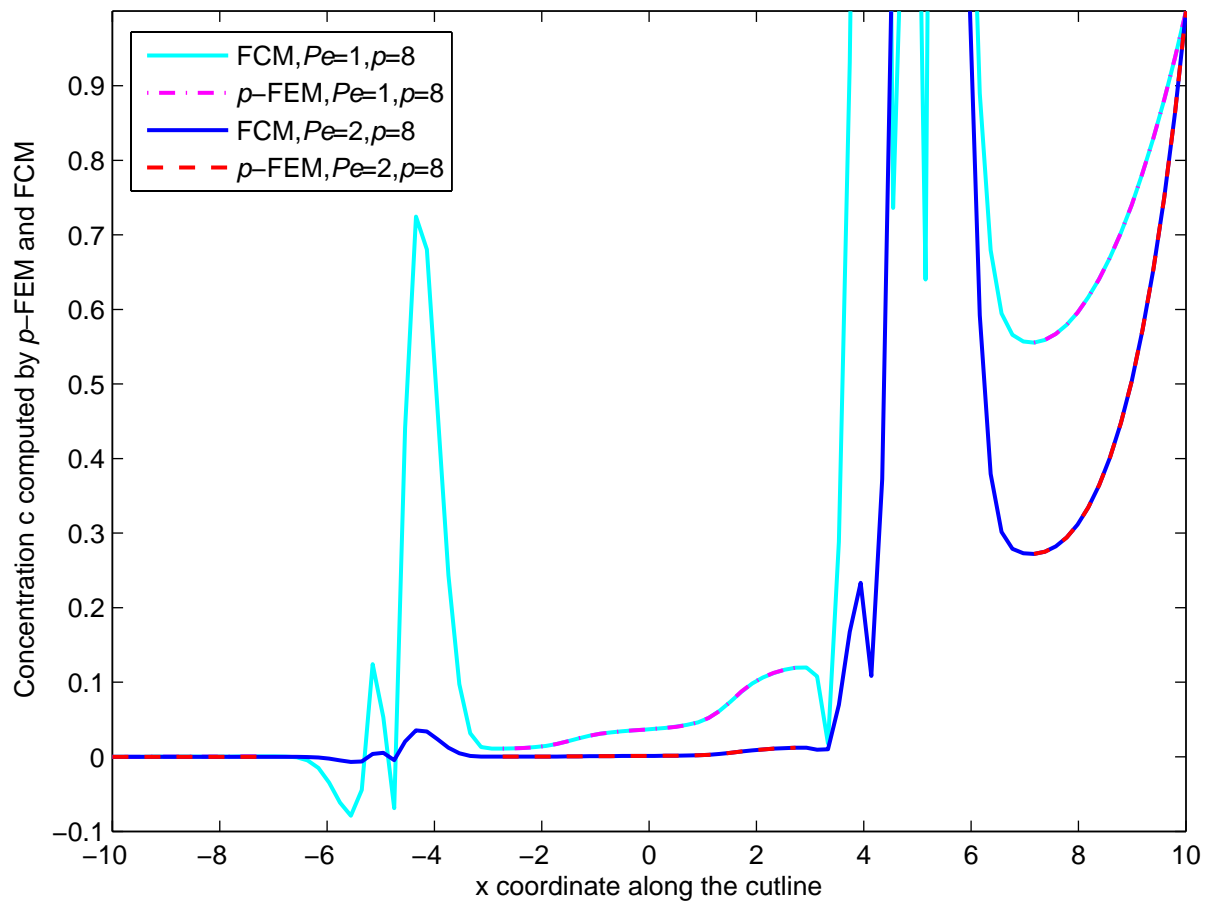


Figure 5.23: Comparison of solutions along the cut-line for $Pe = 1$ and $Pe = 2$

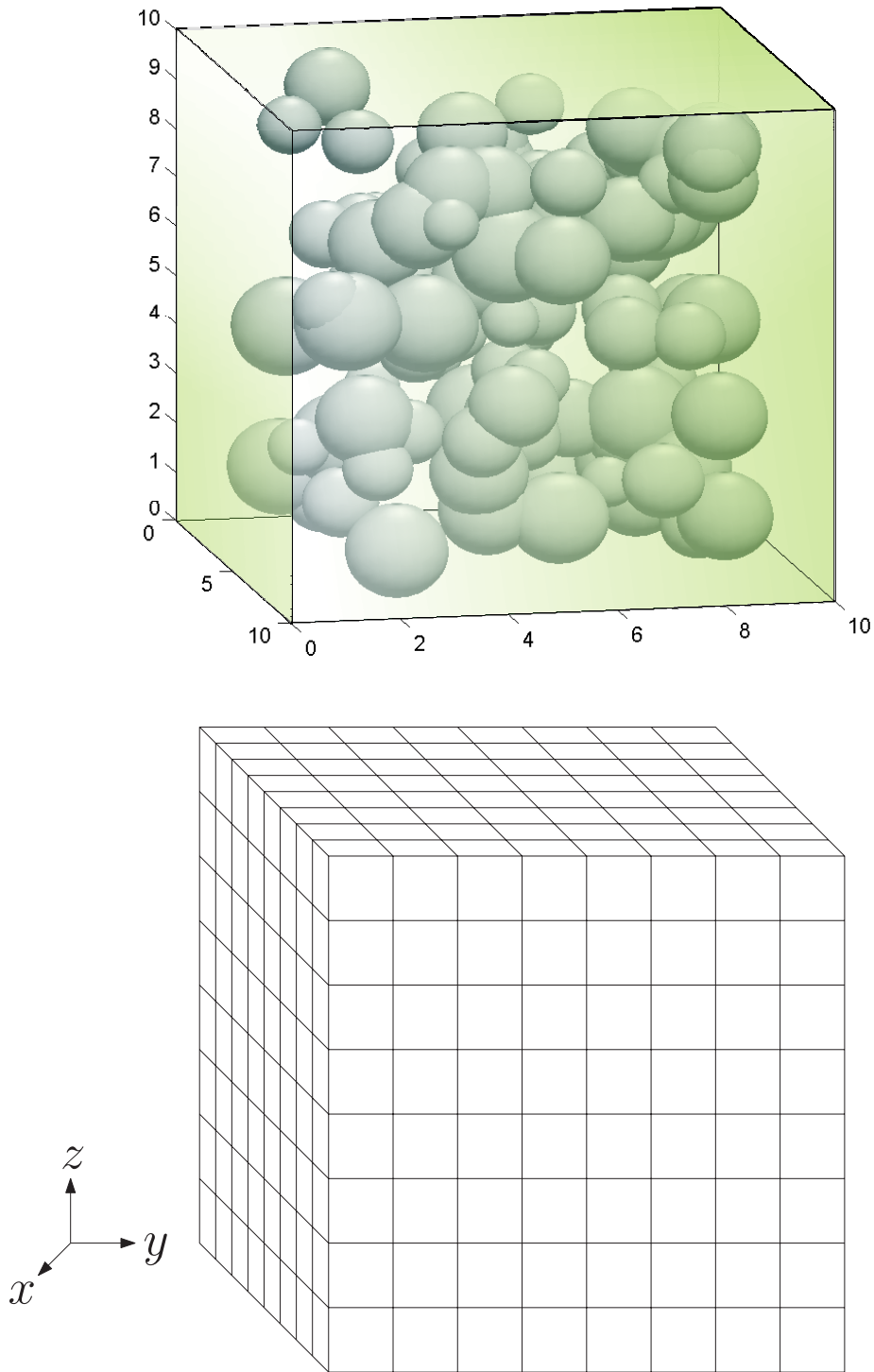


Figure 5.24: Granular media with randomly distributed spheres in 3D

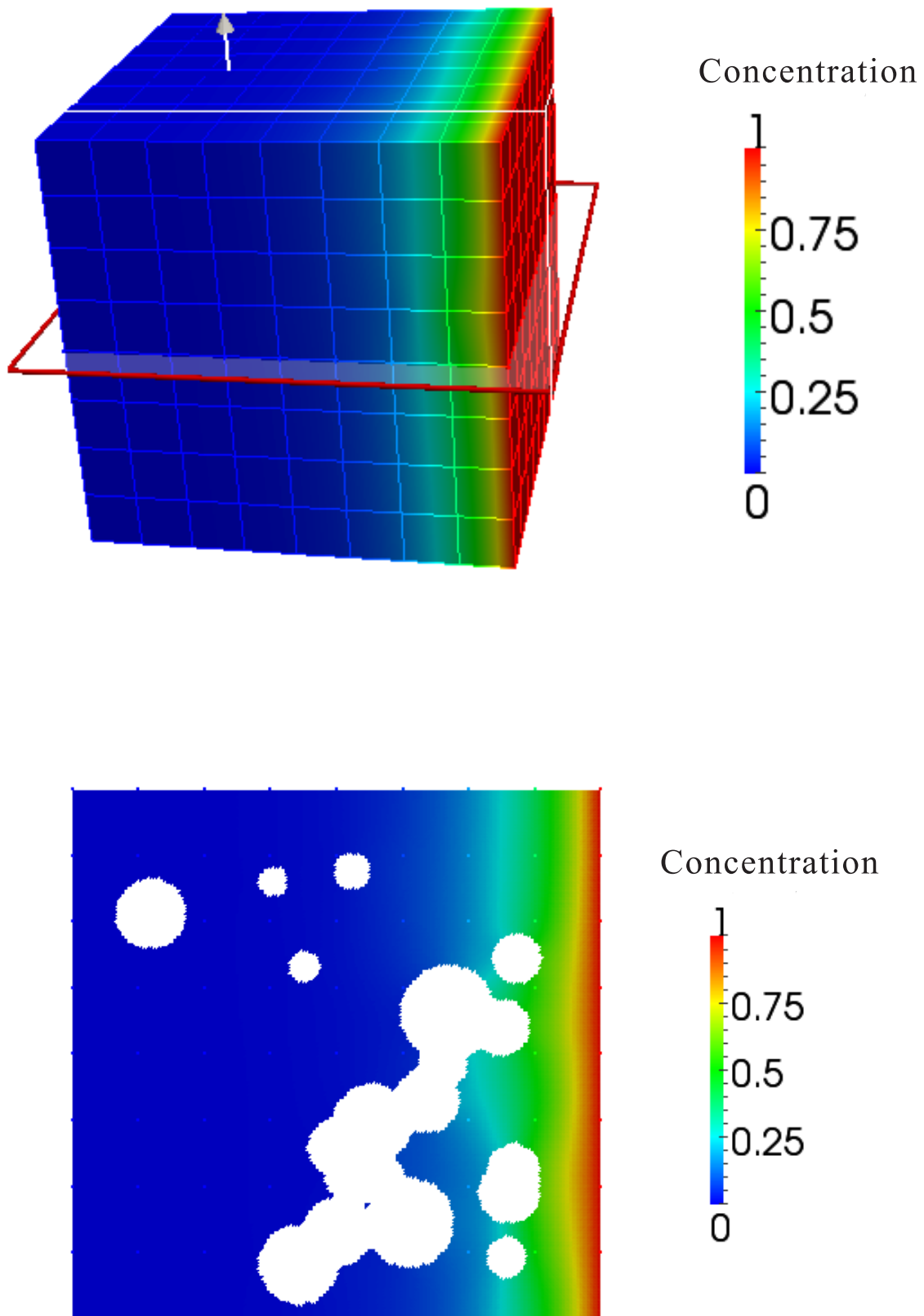


Figure 5.25: Distribution of the concentration: x-y plane

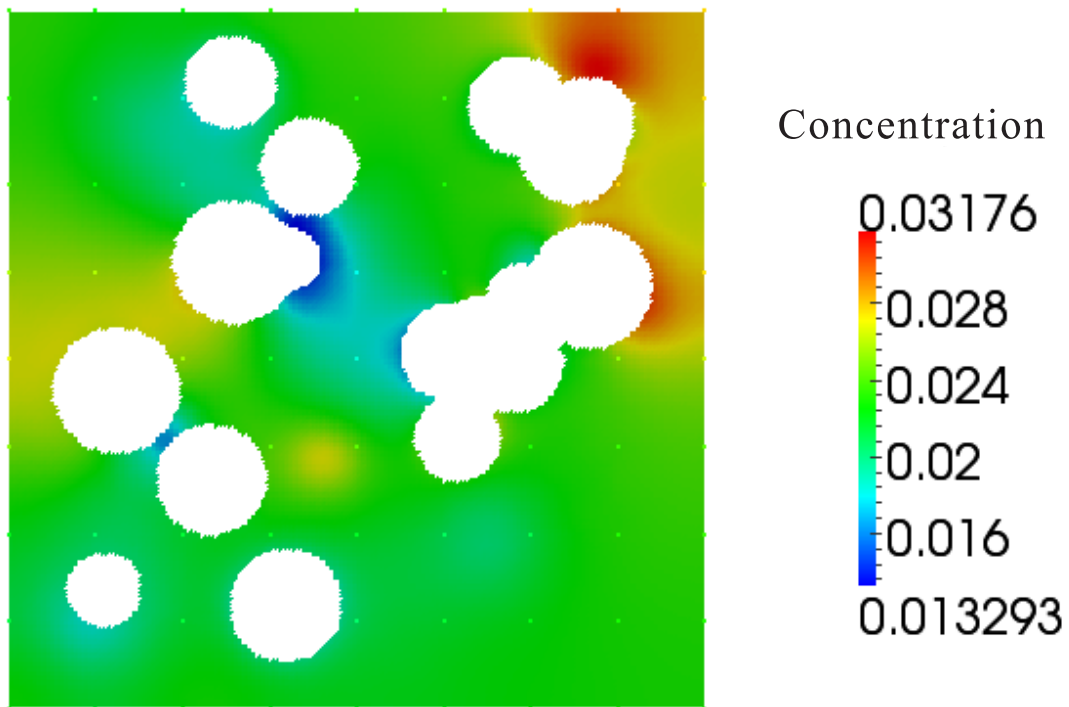
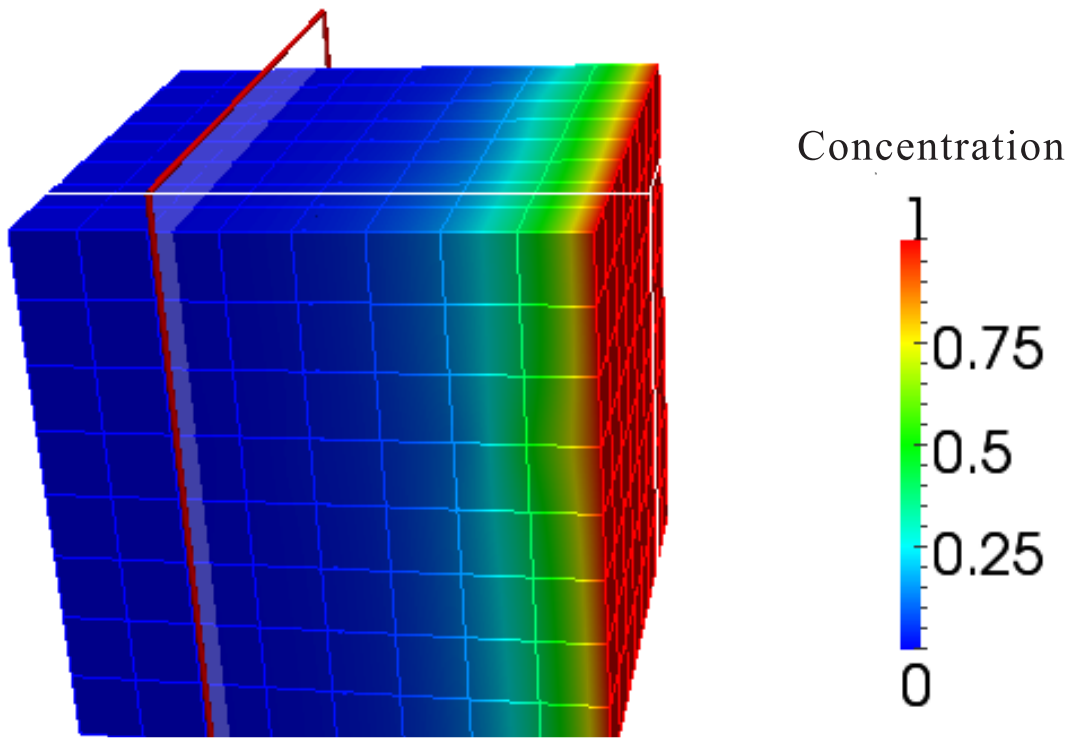


Figure 5.26: Distribution of the concentration: x-z plane

5.4 FCM in multi-component reactive transport problems in porous media

In this section, we investigate the multi-component reactive transport in two-dimensional porous media, the governing equations being given in Equation 5.15.

$$\theta \frac{\partial c_j}{\partial t} + \nabla \cdot (\vec{a}c_j - \theta \nu \nabla c_j) = \sum_{i=1}^N R_{ij} \quad \text{in } \Omega \quad (5.15)$$

The geometry of the domain and its dimensions are illustrated in Figure 5.27 and we apply the parameters listed in Table 5.1.

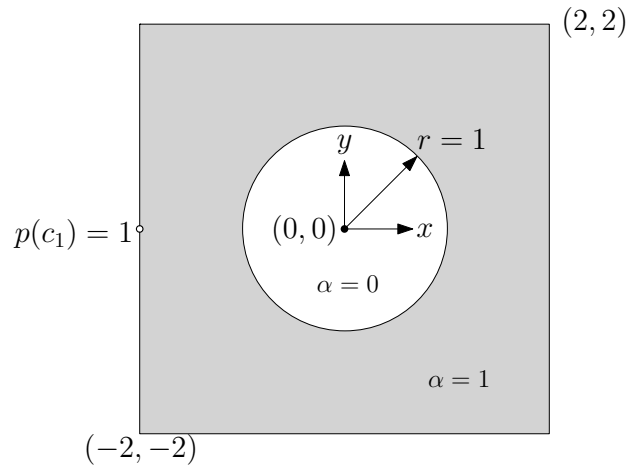


Figure 5.27: The geometry of 2D domain and its dimensions

Diffusion coefficient	ν_x	1	L^2T^{-1}
Diffusion coefficient	ν_y	0.3	L^2T^{-1}
Velocity	q_x	0.5	LT^{-1}
Reaction coefficient 1	k_1	0.05	T^{-1}
Reaction coefficient 2	k_2	0.03	T^{-1}
Reaction coefficient 3	k_3	0.02	T^{-1}

Table 5.1: Parameter values in 2d three-components reactive transport problem in porous media

In this example, the space domain is discretized using a boundary-conforming mesh and the p -FEM approach is employed, whereas 4×4 structured grids are employed in the FCM. The time domain is discretized by the backward finite difference method and the fixed-point iteration is applied to solve the unknowns in coupled reactive terms iteratively. The reference solution is obtained using p -FEM with polynomial degree $p = 6$ and the shape functions with $p = 8$ is applied in the FCM. To improve the integration accuracy, we use the uniform subcell integration approach with 36 subcells in each cell. The numerical solutions of three

components obtained by means of the p -FEM and the FCM at time $t = 50T$ are shown in Figures 5.28, 5.29 and 5.30, respectively.

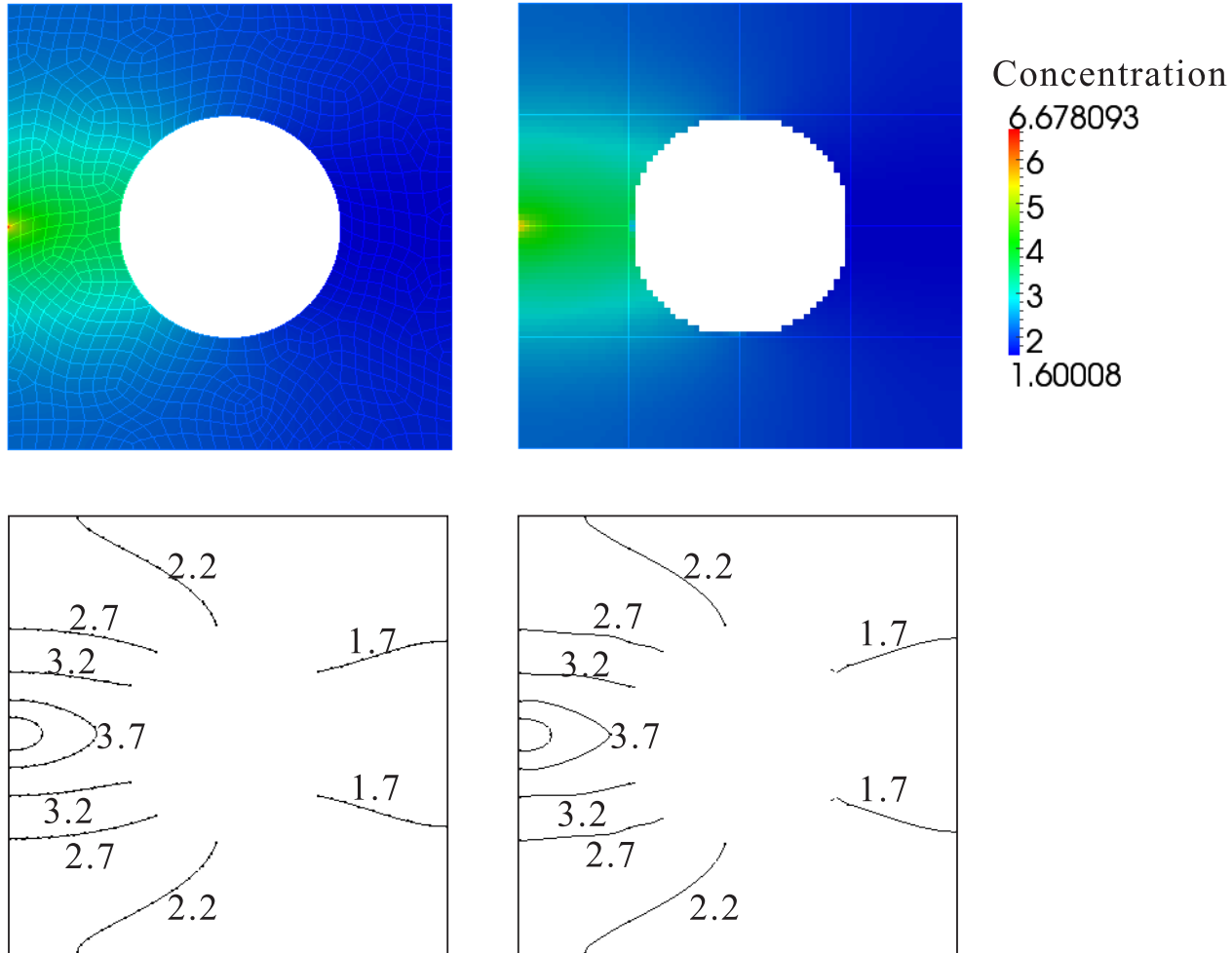


Figure 5.28: Comparison of c_1 between computed using p -FEM with $p=6$ (left) and FCM with $p=8$ (right), at time $t=50T$

The upper sections of Figures 5.28, 5.29 and 5.30 describe the concentration distributions of c_1 , c_2 and c_3 , while the lower sections illustrate the contour of the distribution for a better comparison of the results. We see from the results that, the numerical solution obtained using the FCM corresponds well, generally speaking, with those obtained by means of the p -FEM. The accuracy of the numerical solutions can be improved upon using following approaches: 1) Reducing the integration error by using the adaptive integration scheme. 2) Discretizing the time space with a more accurate method, such as the central finite difference method.

As introduced in Chapter 1, irregular distributions of impermeable materials in groundwater flow give rise to a complex shape of the fluid domain. To solve the concentration distribution during transportation accurately, boundary-conforming meshes are necessary to describe the complex fluid domain, which involves a lot of computational effort. Thanks to the fictitious

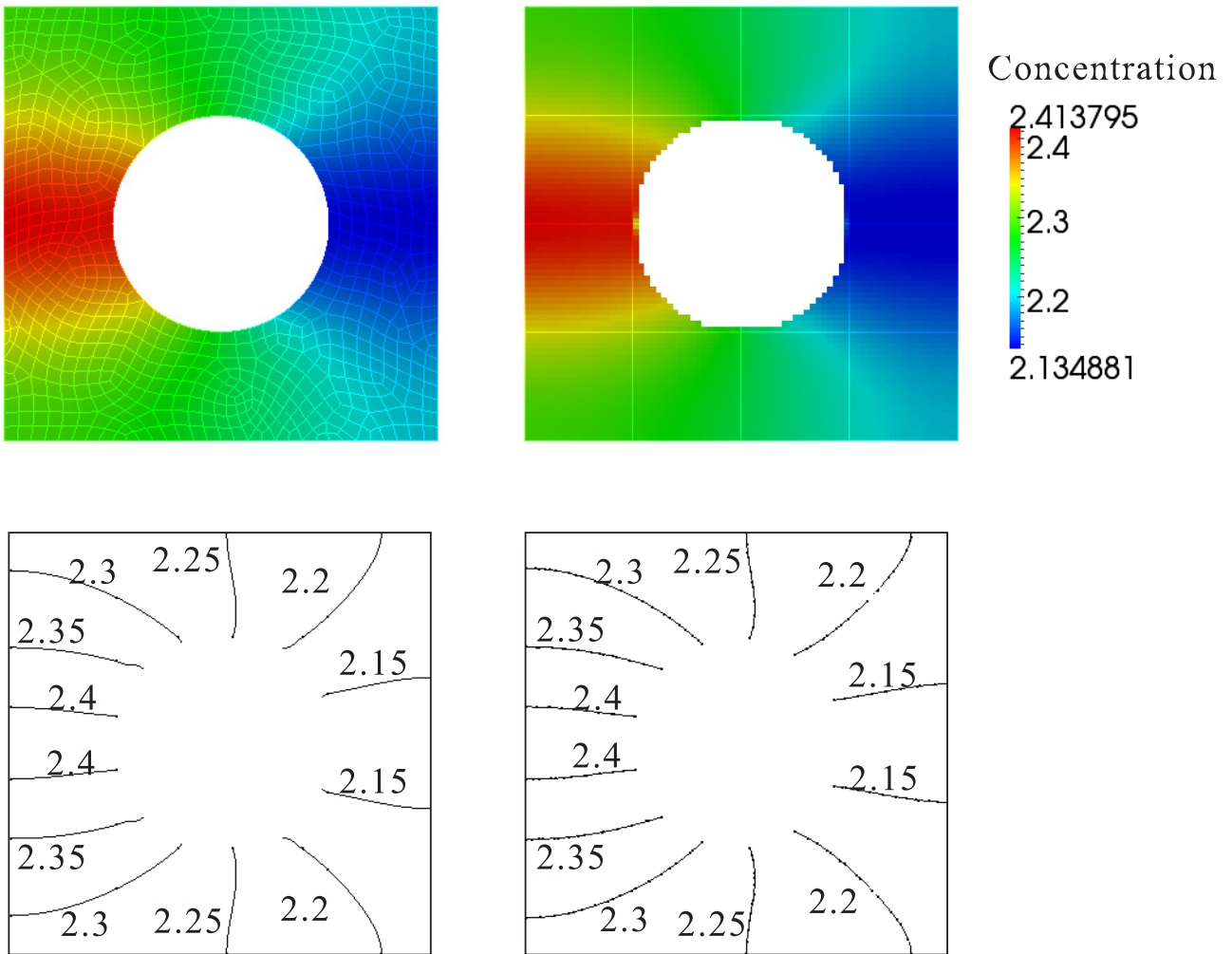


Figure 5.29: Comparison of c_2 computed using p -FEM with $p=6$ (left) and FCM (right), at time $t=50T$

domain concept, the FCM does not require boundary-conforming meshes and is accordingly very well suited for solving transport problems in groundwater flow. In Section 5.3 and Section 5.4, many numerical examples have already proved that either single- or multi-component problems can be solved satisfactorily using the FCM with a level of accuracy comparable with that obtained using the p -FEM.

For the sake of simplicity, the constant velocity and diffusivity are applied over the whole domain. To model more realistic transport problems in groundwater flow, microscopic analysis is required to obtain local velocity and diffusivity at different points of the domain, which can be offered by other project partners in MAC B5 [2]. This information can be written in a file and read by the FCM codes to initialize the velocity field and diffusivity of the domain.

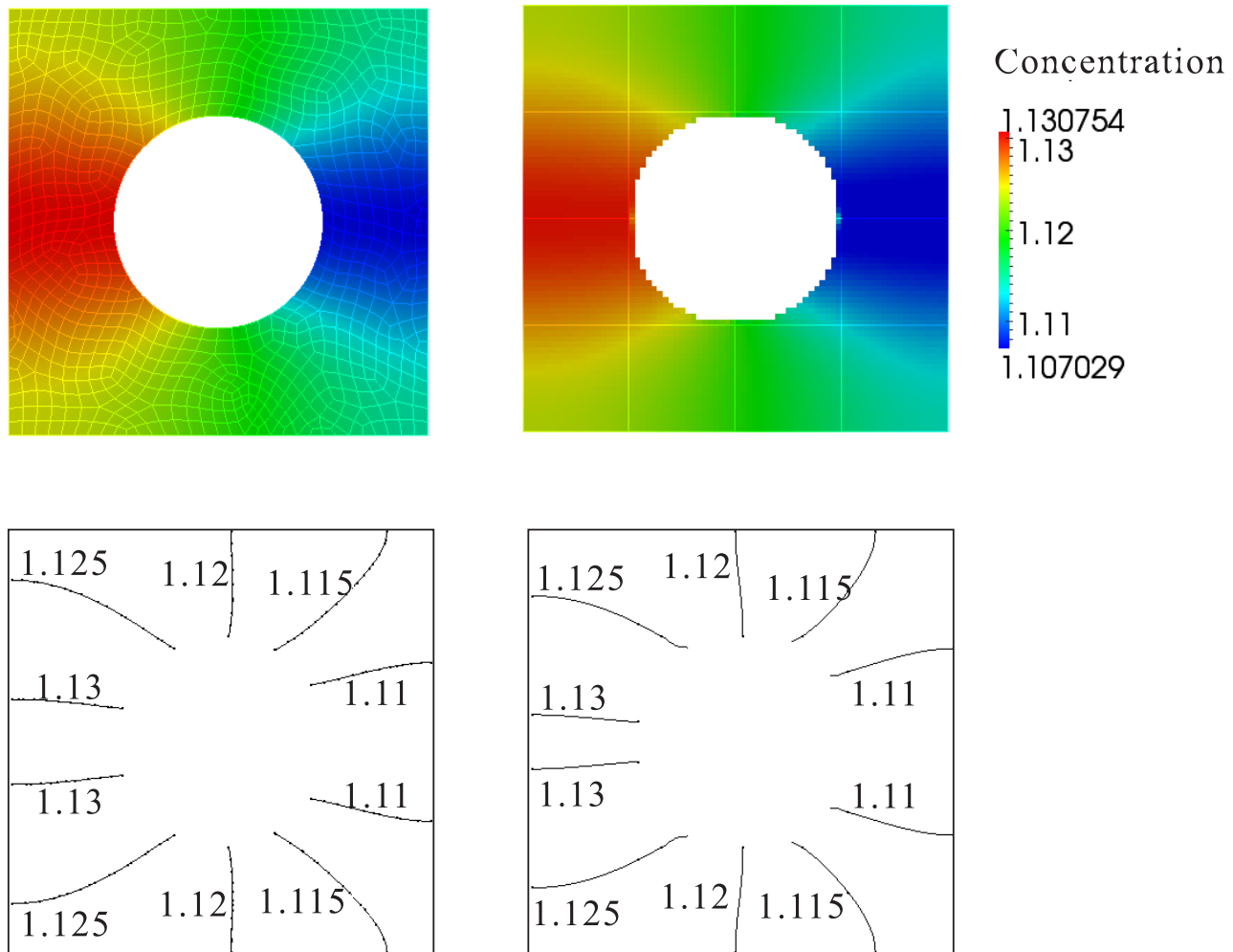


Figure 5.30: Comparison of c_3 computed using p -FEM (left) and FCM (right), at time $t=50T$

Chapter 6

Conclusion

This dissertation has investigated an extension of the FCM for the computation of convection-diffusion problems in porous media. As a combination of the p -FEM and the fictitious domain method, the FCM has effectively controlled the artificial oscillations in convection-dominated problems by an increasing polynomial degree and the solution converges exponentially to the exact solution. By introducing the fictitious domain principle, an originally complex geometry is embedded in a geometrically simpler domain and discretized with structured Cartesian grids.

The distribution of a substance that is fully dissolved in the groundwater flow is described in the context of a convection- diffusion transport problem in porous media. We present that diffusion-dominated flow problems are accurately solved by the standard Bubnov-Galerkin finite element method, whereas it exhibits non-physical oscillations for convection-dominated problems. It is also a common perception that the high order finite element methods increase artificial oscillations for convection dominated problems, rather than decreasing them. The numerical examples in this dissertation clearly show the contrary, however.

The underlying reason for the non-physical oscillation of low order Bubnov-Galerkin methods is that the inclusion of the convective term in the stiffness matrix gives rise to complex eigenvalues of the stiffness matrix, which adds an oscillation component to the solution from a mathematical point of view. The eigenvalue analysis of stiffness matrices in the p -FEM shows that, this oscillation at nodal solutions can be fully eliminated merely by increasing the polynomial degree of the shape functions to a certain value. Compared to other stabilization approaches, the p -FEM succeeded in stabilizing the oscillatory nodal solutions while simultaneously retaining the simplicity of forming weighting functions, benefiting from the standard Bubnov-Galerkin method.

A boundary-conforming mesh for a complex domain is no longer required with the FCM. Three different integration schemes are discussed here: Gaussian quadrature employing over-integration, uniform subcell integration and the adaptive subcell integration scheme. The Gaussian quadrature over-integration approach is easy to implement, whereas subcell integration provides more accurate results.

In order to demonstrate the principle behavior of the FCM, we present one-dimensional examples for flows transported by diffusive flux. Two-dimensional examples are introduced to

show the effect of different *Péclet* numbers and to highlight the advantage of the FCM in the mesh-generation process. In the case of both convection- and diffusion-dominated problems, a p -extension of the FCM yields an exponential rate of convergence in both the L_2 -norm and the energy norm. The three-dimensional problem with randomly distributed obstacles in porous media simulates the real situation in groundwater flow, which is solved admirably using the FCM. Moreover, the FCM also shows a high level of accuracy in the three-component reactive-transport problem including chemical reactions, where each component is coupled with all the others by means of first order reactions.

Bibliography

- [1] A. Abedian, J. Parvizian, A. Düster, H. Khademyzadeh, and E. Rank. Performance of different integration schemes facing discontinuities in the finite cell method. *International Journal of Computational Methods*, 10(3):1–24, 2013.
- [2] Project B5 at Munich Centre of Advanced Computing. Transport and Reaction Processes in Porous Media. *Technischen Universität München*, 2008.
- [3] Frank Baaijens. A fictitious domain/mortar element method for fluid-structure interaction. *International Journal for Numerical Methods in Fluids*, 35:743–761, 2001.
- [4] J. Bear. *Dynamics of Fluids in Porous Media*. Dover, 1972.
- [5] T. Belytschko, T. Black, Y.Y. Lu, and L. Gu. Element-free galerkin methods. *International Journal for Numerical Methods in Engineering*, 37:229–256, 1994.
- [6] M. Braack and E. Burman. Local projection stabilization for the oseen problem and its interpretation as a variational multiscale method. *SIAM Journal on Numerical Analysis*, 43:2544–2566, 2006.
- [7] A. Brooks and T.J.R. Hughes. Streamline upwind Petrov-Galerkin formulations for convection dominated flows with particular emphasis on the incompressible Navier-Stokes equations. *Computer Methods in Applied Mechanics and Engineering*, 32:199–259, 1982.
- [8] R.L. Burden and J.D. Faires. *Numerical Analysis, 9th Edition*. Brooks Cole Pub., 2011.
- [9] D.M. Causon and C.G. Mingham. *Introductory Finite Difference Methods for PDEs*. Ventus Publishing ApS, 2010.
- [10] Y. Chen, J. Lee, and A. Eskandarian. *Meshless methods in solid mechanics*. Springer, Heidelberg, 2006.
- [11] J. Chessa and T. Belytschko. An extended finite element method for two-phase fluids. *ASME J. Appl. Mech.*, 70:10–17, 2003.
- [12] R. Codina and J. Blasco. Analysis of a stabilized finite element approximation of the transient convection-diffusion-reaction equation using orthogonal subscales. *Computing and Visualization in Science*, 4:167–174, 2002.
- [13] S. Del Pino and O. Pironneau. A fictitious domain based general pde solver. In Y. Kuznetsov, P. Neittanmaki, and O. Pironneau, editors, *Numerical methods for scientific computing variational problems and applications*, CIMNE, Barcelona, Spain, 2003.

-
- [14] D.A. Di Pietro and A. Ern. *Mathematical Aspects of Discontinuous Galerkin Methods, Mathematiques et Applications*, volume 69. Springer-Verlag, 2011.
- [15] J. Donea and A. Huerta. *Finite Element Methods for Flow Problems*. John Wiley & Sons, 2003.
- [16] A. Düster. *High Order FEM – Lecture Notes*. Numerische Strukturanalyse mit Anwendungen in der Schiffstechnik (M-10), Studienbereich Maschinenbau, Technische Universität Hamburg-Harburg, 2010.
- [17] A. Düster, H. Bröker, H. Heidkamp, U. Heißeberer, S. Kollmannsberger, Z. Wassouf, R. Krause, A. Muthler, A. Niggel, V. Nübel, M. Rücker, and D. Scholz. *AdhoC⁴ – User’s Guide*. Lehrstuhl für Bauinformatik, Technische Universität München, 2004.
- [18] A. Düster, J. Parvizian, Z. Yang, and E. Rank. The finite cell method for three-dimensional problems of solid mechanics. *Computer Methods in Applied Mechanics and Engineering*, 197:3768–3782, 2008.
- [19] O.G. Ernst. Residual-Minimizing Krylov Subspace Methods for Stabilized Discretization of Convection-Diffusion Equations. *SIAM J. Matrix Anal. Appl.*, 21(4):1079–1101, 2000.
- [20] J. Fish and T. Belytschko. *A first course in Finite Elements*. John Wiley & Sons, 2007.
- [21] T.-P. Fries and T. Belytschko. The intrinsic xfem: A method for arbitrary discontinuities without additional unknowns. *International Journal for Numerical Methods in Engineering*, 68:1358–1385, 2006.
- [22] R. Glowinski and Y. Kuznetsov. Distributed Lagrange multipliers based on fictitious domain method for second order elliptic problems. *Computer Methods in Applied Mechanics and Engineering*, 196:1498–1506, 2007.
- [23] R. Glowinski, T.-W. Pan, T.I. Hesla, and D.D. Joseph. A distributed lagrange multiplier/fictitious domain method for particulate flows. *International Journal of Multiphase Flow*, 25:755–794, 1999.
- [24] W.J. Gordon and Ch.A. Hall. Transfinite element methods: Blending function interpolation over arbitrary curved element domains. *Numerische Mathematik*, 21:109–129, 1973.
- [25] I. Harari and T. J. R. Hughes. Stabilized finite element methods for steady advection–diffusion with production. *Computer Methods in Applied Mechanics and Engineering*, 115:165–191, 1994.
- [26] J. S. Hesthaven and T. Warburton. *Nodal Discontinuous Galerkin Methods*. Springer-Verlag, 2008.
- [27] C. Hirsch. *Numerical Computation of Internal & External Flows*. Butterworth-Heinemann, Great Britan, 2007.
- [28] J.P. Holman. *Heat Transfer*. McGraw-Hill, 2002.

- [29] T. J. R. Hughes. Multiscale phenomena: Green's functions, the Dirichlet-to-Neumann formulation, subgrid scale models, bubbles and the origins of stabilized methods. *Computer Methods in Applied Mechanics and Engineering*, 127:387–401, 1995.
- [30] T. J. R. Hughes. *The Finite Element Method: Linear Static and Dynamic Finite Element Analysis*. Dover Publications, 2000.
- [31] T. J. R. Hughes and G. M. Hulbert. Large eddy simulation and the variational multiscale method. *Computing and Visualization in Science*, 3:47–59, 2000.
- [32] T. J. R. Hughes and G. Sangalli. Variational multiscale analysis: the final-scale Green's functions, projection, optimization, localization and stabilized methods. *SIAM Journal on Numerical Analysis*, 45:539–557, 2007.
- [33] T.J.R. Hughes, L.P. Franca, and M. Mallet. A new finite element formulation for computational fluid dynamics: I. Symmetric forms of the compressible Euler and Navier-Stokes equations and the second law of thermodynamics. *Computer Methods in Applied Mechanics and Engineering*, 54(2):223 – 234, 1986.
- [34] M. Huysmans and A. Dassargues. Review of the use of pecelet numbers to determine the relative importance of advection and diffusion in low permeability environments. *Hydrogeology Journal*, 13:895–904, 2005.
- [35] M. A. Hyman. Non-iterative numerical solution of boundary value problems. *Appl. Sci. Res. Sec. B2*, pages 325–351, 1952.
- [36] S. Ingebritsen, W. Stanford, and C. Neuzil. *Groundwater in Geologic Processes*. Cambridge University Press, 2006.
- [37] P. Knobloch and L. Tobiska. On the stability of finite-element discretizations of convection-diffusion-reaction equations. *IMA Journal of Numerical Analysis*, 31:147–164, 2011.
- [38] P. Kumar, G.R. Dodagoudar, and B.N. Rao. Contaminant transport modelling using egfm. *Springer Proc. in Physics, Theoretical and Numerical Unsaturated Soils Mechanics, Weimar, Germany*, pages 225–231, 2007.
- [39] P. Kumar, G.R. Dodagoudar, and B.N. Rao. Two-dimensional modelling of contaminant transport through saturated porous media using the radial point interpolation method (rpm). *Hydrogeology*, 16:1497–1505, 2008.
- [40] G. Liu, G. Zhang, Y. Gu, and Y. Wang. A meshfree radial point interpolation method (rpm) for three-dimensional solids. *Computational Mechanics*, 36:421–430, 2005.
- [41] G. Lube and G. Rapin. Residual-based stabilized higher-order FEM for advection-dominated problems. *Computer Methods in Applied Mechanics and Engineering*, 195:4124–4138, 2006.
- [42] L.B. Lucy. A numerical approach to the testing of the fission hypothesis. *Astron. J.*, 8(12):1013–1024, 1977.

- [43] M. Lunn, R.J. Lunn, and R. Mackay. Determining analytic solutions of multiple species contaminant transport, with sorption and decay. *Journal of Hydrology*, 180:195–210, 1996.
- [44] G. Matthies, P. Skrzypacz, and L. Tobiska. Stabilization of local projection type applied to convection–diffusion problems with mixed boundary conditions. *Electronic Transactions on Numerical Analysis*, 32:90–105, 2006.
- [45] B. Maury. A fat boundary method for the poisson problem in a domain with holes. *Journal of Scientific Computing*, 16:319–339, 2001.
- [46] N. Moës, J. Dolbow, and T. Belytschko. A finite element method for crack growth without remeshing. *International Journal for Numerical Methods in Engineering*, 64:131–150, 1999.
- [47] P. Neittaanmäki and D. Tiba. An embedding of domains approach in free boundary problems and optimal design. *SIAM Journal on Control and Optimization*, 33(5):1587–1602, 1995.
- [48] J. Parvizian, A. Düster, and E. Rank. Finite cell method – h- and p-extension for embedded domain problems in solid mechanics. *Computational Mechanics*, 41:121–133, 2007.
- [49] I. Ramière, P. Angot, and M. Belliard. Fictitious domain methods to solve convection-diffusion problems with general boundary conditions. In *17th Computational Fluid Dynamics conference-AIAA. Toronto, Canada*. Journal of the American Institute of Aeronautics and Astronautics, 2005.
- [50] E. Rank, C. Katz, and H. Werner. On the importance of the discrete maximum principle in transient analysis using finite element methods. *International Journal for Numerical Methods in Engineering*, 19:1771 – 1782, 1983.
- [51] E. Rank, S. Kollmannsberger, Ch. Sorger, and A. Düster. Shell finite cell method: A high order fictitious domain approach for thin-walled structures. *Accepted for publication in Computer Methods in Applied Mechanics and Engineering*, 2011.
- [52] H.-G. Roos, M. Stynes, and L. Tobiska. *Robust Numerical Methods for Singularly Perturbed Differential Equations*, volume 24. Springer Series in Computational Mathematics, 2008.
- [53] A. Russo. Bubble stabilization of the finite element methods for the linearized incompressible Navier-Stokes equation. *Computer Methods in Applied Mechanics and Engineering*, 132:335–343, 1996.
- [54] H. Sauerland and T.-P. Fries. The extended finite element method for two-phase and free-surface flows: A systematic study. *Journal of Computational Physics*, In Press, Accepted Manuscript, 2011.
- [55] V. K. Saul’ev. On solution of some boundary value problems on high performance computers by fictitious domain method. *Siberian Mathematical Journal*, 4:912–925, 1963.

- [56] D. Schillinger, S. Kollmannsberger, R. Mundani, and E. Rank. The Finite Cell Method for Geometrically Nonlinear Problems of Solid Mechanics. In *The World Congress on Computational Mechanics*. Sydney, Australia, 2010.
- [57] D. Schillinger, S. Kollmannsberger, R. Mundani, and E. Rank. The Hierarchical B-Spline Version of the Finite Cell Method for Geometrically Nonlinear Problems of Solid Mechanics. In *The European Conference on Computational Mechanics*. Paris, France, http://www.eccm2010.org/complet/fullpaper_1204.pdf, 2010.
- [58] J.H. Spurk and N. Aksel. *Fluid Mechanics*. Springer, 2. edition, 2008.
- [59] B.A. Szabó and I. Babuška. *Finite element analysis*. John Wiley & Sons, 1991.
- [60] B.A. Szabó, A. Düster, and E. Rank. The p-version of the Finite Element Method. In E. Stein, R. de Borst, and T. J. R. Hughes, editors, *Encyclopedia of Computational Mechanics*, volume 1, chapter 5, pages 119–139. John Wiley & Sons, 2004.
- [61] A. Thom and C.J. Apelt. *Field Computations in Engineering and Physics*. London: D. Van Nostrand, 1961.
- [62] L. Tobiska. Analysis of a new stabilized higher order finite element method for advection-diffusion equations. *Computer Methods in Applied Mechanics and Engineering*, 196:538–550, 2006.
- [63] U. van Rienen. *Numerical Methods in Computational Electrodynamics - Linear Systems in Practical Applications*. Springer, 2001.
- [64] P.E.J. Vos, R. Loon, and S.J. Sherwin. A comparison of fictitious domain methods appropriate for spectral/hp element discretizations. *Computer Methods in Applied Mechanics and Engineering*, 197:2275–2289, 2008.
- [65] W. Wall, P. Gammnitzer, and A. Gerstenberger. Fluid-structure interaction approaches on fixed grids based on two different domain decomposition ideas. *International Journal of Computational Fluid Dynamics*, 22:411–427, 2008.
- [66] Wikipedia. [http://en.wikipedia.org/wiki/Permeability_\(earth_sciences\)](http://en.wikipedia.org/wiki/Permeability_(earth_sciences)).
- [67] Wikipedia. http://en.wikipedia.org/wiki/Groundwater_flow_equation.
- [68] Z. Yang, C. Dick, S. Kollmannsberger, A. Düster, M. Ruess, R. Burgkart, R. Westermann, and E. Rank. Computational Steering for Orthopaedics. *Submitted to Biomechanics and Modeling in Mechanobiology*, 2010.
- [69] Z. Yang, A. Düster, M. Ruess, and E. Rank. The Finite Cell Method for Interactive Orthopaedic Simulation. 10 (1/2):66, 2009.